Non-scanning Fluorescence Confocal Microscopy using Laser Speckle Illumination

by

Shihong Jiang, BEng.

School of Electrical and Electronic Engineering

Thesis submitted to The University of Nottingham
for the Degree of Doctor of Philosophy

October 2005

Abstract

Confocal scanning microscopy (CSM) is a much used and advantageous form of microscopy. Although CSM is superior to conventional microscopy in many respects, a major disadvantage is the complexity of the scanning process and the sometimes long time to perform the scan. In this thesis a novel non-scanning fluorescence confocal microscopy is investigated. The method uses a random time-varying speckle pattern to illuminate the specimen, recording a large number of independent full-field frames without the need for a scanning system. The recorded frames are then processed in a suitable way to give a confocal image. The goal of this research project is to confirm the effectiveness and practicality of speckle-illumination microscopy and to develop this proposal into a functioning microscope system. The issues to be addressed include modelling of the system performance, setting up experiments, computer control and image processing. This work makes the following contributions to knowledge:

- The development of criteria for system performance evaluation
- The development of methods for speckle processing, whereby the number of frames required for an image of acceptable quality can be reduced
- The implementation of non-scanning fluorescence confocal microscopy based upon separate recording of the speckle patterns and the fluorescence frames, demonstrating the practicality and effectiveness of this method
- The realisation of real-time image processing by optically addressed spatial light modulator, showing how this new form of optical arrangement may be used in practice

The thesis is organised into three main segments. Chapters 1-2 review related work and introduce the concepts of fluorescence confocal microscopy. Chapters 3-5 discuss system modelling and present results of performance evaluation. Chapters 6-8 present experimental results based upon the separate recording scheme and the spatial light modulation scheme, draw conclusions and offer some speculative suggestions for future research.

Acknowledgements

The author would like to thank Dr John Walker for his original and creative work in the field of fluorescence confocal microscopy which provides a well-defined research project for a PhD student, especially for his effort in providing the author with the opportunity to carry out this work under his direct supervision. Without John Walker's expert knowledge of confocal microscopy and of relevant disciplines, the completion of this work would have been an extremely difficult undertaking. The author would also like to thank Professor Mike Somekh, Dr Barrie Hayes-Gill, Dr C. W. See and other staff within the Applied Optics Group for their kind support and helpful advice throughout his PhD studies. Special thanks are due to the International Office of the University of Nottingham for providing funding to make the three-year research possible. Thanks also go to the many members of staff and postgraduate students who assisted the author with technical data, thoughtful comments as well as equipment and lab tools for building the experimental systems.

Other people to whom the author is indebted for being very valuable to him with his life and work are his wife Hong Ye, his son Weifeng and his mother Airu Sun.

Table of Contents

1. Introduction

"Real knowledge is to know the content of one's ignorance."

— Confucius, 551 BC - 479

Confocal scanning microscopy (CSM), invented by Minsky in 1955 [1], is a widely used technique in many fields of science particularly in the life and biosciences [2-4]. Unlike conventional microscopy, CSM illuminates and images only one small spot at a time, in the focal plane of the objective. The sequences of points of light from the specimen are detected through a pinhole and the output from the detector is built into an image and displayed by a computer. CSM has many advantages over conventional microscopy, including a valuable depth discrimination property that permits three-dimensional image reconstruction, the improved lateral resolution and a reduced effect of flare or scattered light contributing to the image. As CSM is a powerful and irreplaceable tool for studying biological cells *in vivo* or *in vitro*, its capabilities have been extended to include fluorescence detection and lifetime imaging [5-8], and to improve its spatial resolution [9-12]. Progress in multiphoton excitation processes, interest in the burgeoning field of single-molecule biophysics have recently pushed CSM to its ultimate level of sensitivity [13-15].

Because a confocal image is built up pixel by pixel by scanning the illuminated spot over the specimen, it is intrinsically time-consuming if a large area needs to be searched. The noise level of confocal images can be easily higher than wide-field images [16], particularly at high scan speeds, due to the limited number of photons of fluorescence that can be collected from a diffraction-limited area in pixel dwell times lasting fractions of a microsecond [17, 18]. Moreover, the light gathering ability of CSM is low due to the use of a pinhole. During the last few decades, various efforts have been undertaken to circumvent these limitations but retain the advantages of confocal microscopy. Major advances include direct view, or tandem scanning confocal microscopy, structured-light illumination such as standing wave illumination, grid pattern illumination and laser speckle illumination. In this chapter a general description and review of several state-of-the-art confocal microscopic techniques is given.

1.1 Laser confocal scanning microscopy

Lasers are the most common light source for confocal scanning microscopes as they provide ideal types of excitation light for fluorescence microscopy applications. In Laser Scanning Confocal Microscope (LSCM) shown in Fig. 1.1 a laser beam is focused by an objective onto a fluorescent specimen through an X-Y deflection mechanism. The mixture of reflected light and emitted fluorescent light is captured by the same objective and (after conversion into a static beam by the X-Y scanner device) is focused onto a photomultiplier via a dichroic beamsplitter. Commonly, a raster scan is generated by reflection from two moving mirrors, aligned at 90° with the motion of each mirror being driven by a linear saw-tooth control signal. This scanning unit is elaborately designed so that the laser location is changing linearly without image distortion. Current LSCMs collect images with a scan speed of up to 5 frames/second with 512×512 pixels, such as the ZEISS LSM 510 META in which the scanner consists of two independent galvanometric scanning mirrors. By varying the distance between the objective and the specimen, users can generate a Z-series that dissect through the specimen with a Z-scan interval down to 50 –100 nm. Object features in the order of 0.2 μm can be resolved, and height differences of less than 0.1 μm are made visible [19].

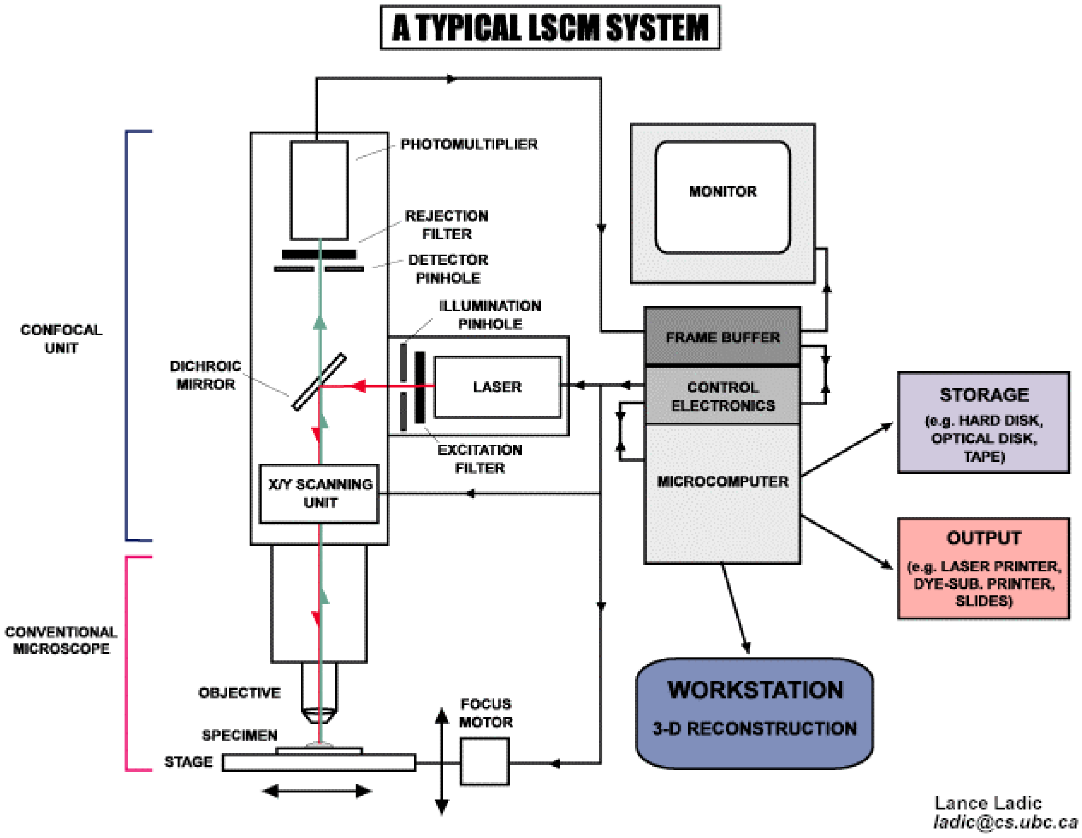

Fig. 1.1. A typical LSCM system

(From http://yakko.bme.virginia.edu/phy506/system.gif)

1.2 Tandem scanning confocal microscopy

Mojmir Petran [20] pioneered the use of Nipkow disks in CSM, where the specimen is illuminated with a large number of scanning beams in tandem to improve scanning speed. A Nipkow disk is an opaque circular disk perforated with small holes arranged at equal angular separations arranged in an Archimedean spiral. The holes trace a raster scanning pattern when the disk is spun around its centre. In the tandem scanning confocal microscope, the Nipkow disk can be spun rapidly enough to provide video-rate (30 frames/second) imaging and was used in early experiments on television and later in Petran's confocal microscope. A typical Nipkow-disk confocal microscope arrangement is shown in Fig. 1.2. The downside of the Nipkow-disk type system is that the efficiency of light transmission is low, usually less than 5%, often resulting in fluorescence that is too dim to take advantage of the high imaging speed of the system [21].

Fortunately, the development of a newer generation of disk scanning confocal microscopes has increased excitation light throughput and thus enabled real-time confocal microscopy [22]. The VisiTech's QLC100 is a good example [23].

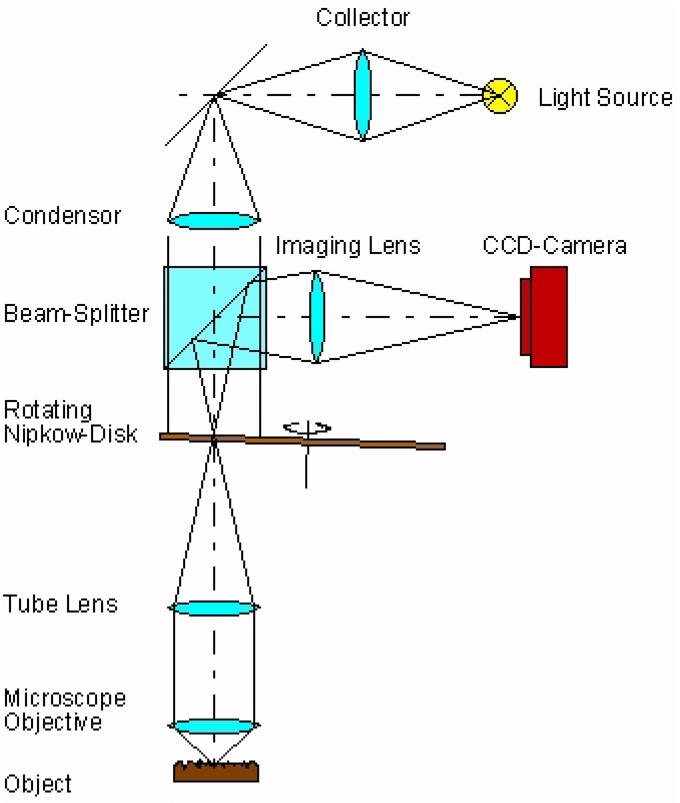

Fig. 1.2. Confocal microscope using a rotating Nipkow-disk

As illustrated in Fig. 1.3, the QLC100 utilizes two disks; one with about 20,000 microlenses, the other with pinholes arranged in the same pattern. Light incident on the upper disk is focused on the corresponding pinholes by the microlenses that increase light transmission to about 40% of the light from the source. The disks are rotated together at 1800 rpm so that the light beams raster-scan the specimen. The light passing through the pinhole is focused by an objective lens on a spot in the specimen. Fluorescent light from the specimen returns along the same path back through the objective lens, through the pinhole, to a beamsplitter and then through a relay lens which images the point on the camera detector or eyepiece image plane. Both the laser beam and the emitted fluorescent light pass through a pinhole, thus allowing the QLC100 to produce two-dimensional confocal images at high speed. The pinhole pattern is designed to capture 12 frames per rotation or 360 frames per second of confocal images, allowing capture and analysis of cellular and physiological processes in real time.

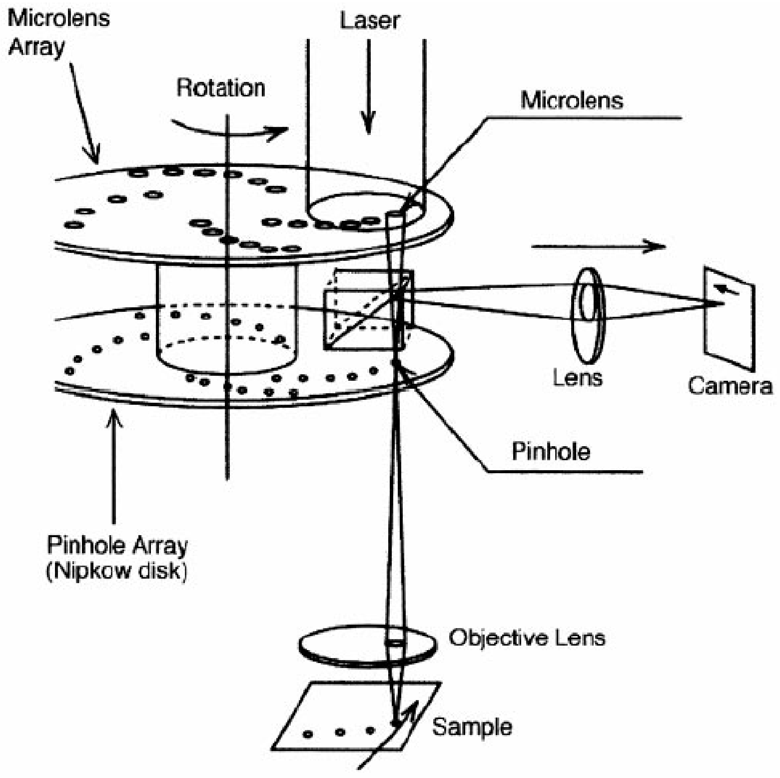

Fig. 1.3. QLC100 dual disk scanning confocal system (From Ref. 21)

1.3 Structured-light illumination

The aforementioned instruments work on a scanning basis with the complexity of the scanning apparatus being the main disadvantage of confocal systems compared with conventional microscopy. Wide-field imaging does not have the inherent depth resolution of the scanning techniques. However, there are a number of remarkable techniques to obtain 3D images in whole-field microscopes using structured-light illumination. Here two important structured illumination techniques will be discussed. Other methods include image interference microscopy (I^nM) invented by Mats GL Gustafsson [24, 25] and harmonic excitation light microscopy (HELM) by Jan T. Frohn et al [26-28]. These methods are focused on obtaining optical superresolution, so they are beyond the scope of this thesis and will not be discussed here.

1.3.1 Axially structured illumination

Standing-wave fluorescence microscopy (SWFM) was invented by Brent Bailey et al. in 1993 [29-32]. Its principle is shown in Fig. 1.4 where two collimated beams from a laser are directed at the specimen from opposite sides. The coherent, equal-amplitude beams (arrows) cross symmetrically relative to the microscope axis, and are s-polarised. The interference of the beams then produces planar nodes and antinodes (alternating dashed and solid lines) oriented perpendicular to the microscope axis. Fluorescence is therefore excited in the specimen in a series of equally spaced laminar zones, and nulled at the nodes. By optically shifting the standing-wave field planes up or down within the specimen, it is possible to excite or null structures selectively at different levels within the depth-of-field of the microscope.

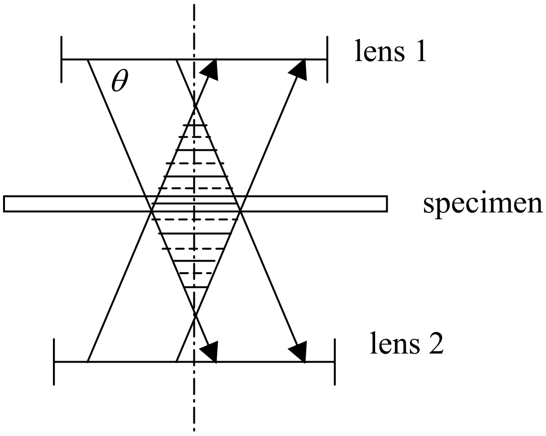

Fig. 1.4. Schematic of axial standing wave illumination (From Ref. 30)

The intensity of the standing-wave field is constant over any plane parallel to the x,y-plane, and varies sinusoidally with the axial (z) coordinate as:

$$I_{ex} = 1 + \cos[(4\pi n / \lambda_0)(\cos\theta)z + \phi] = 1 + \cos(Kz + \phi) \tag{1.1}$$

where n is the specimen refractive index, λ is the laser wavelength, and ϕ is the relative phase of the two beams which can be adjusted with very high precision by moving a mirror with a piezo-electric drive. The image equation with the camera held fixed in the image focal plane and the object stepped through focus, is:

$$I(x', y', \Delta z) = \iiint O(x, y, z - \Delta z)[1 + \cos(Kz + \phi)]S(x', y'; x, y, z)\mathrm{d}x\mathrm{d}y\mathrm{d}z \tag{1.2}$$

where S is the microscope's intensity point spread function and Δz is the focus position of the object. Since the value of ϕ is unknown, at least three images, corresponding to a phase shift of ϕ between them, need to be acquired at each focal plane to determine the optically sectioned image I. The axial resolution can be better than a quarter of the node spacing, or 0.045 μm, under typical conditions.

Because the axial response to a point object in the SWFM has a ringing effect, the sample thickness is limited by the period of the standing wave field unless there is *a priori* knowledge. A further development of this method, called excitation field synthesis, improves the sectioning capability by utilizing a superposition of different interference patterns giving one sharp interference maximum.

1.3.2 Laterally structured illumination

A simple method of using grid pattern illumination was proposed in 1997 by which optically sectioned fluorescence images may be obtained with conventional microscopes [33-35].

As illustrated in Fig.1.5, a one-dimensional grid pattern is projected onto the specimen. A CCD camera captures three images, I_1, I_2 and I_3, corresponding to a relative spatial phase shift of the grid of 120° between them. These images are then processed by

$$I_p = \frac{\sqrt{2}}{3}\{(I_1 - I_2)^2 + (I_1 - I_3)^2 + (I_2 - I_3)^2\}^{1/2} \tag{1.3}$$

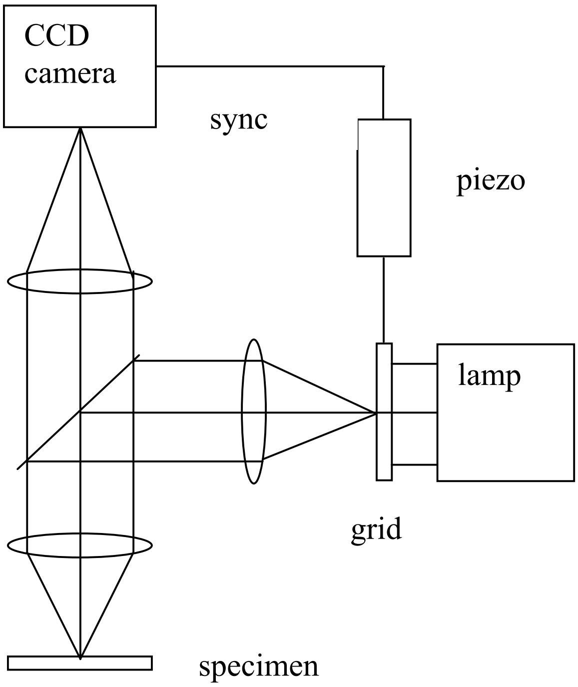

Fig. 1.5. Schematic of the optical arrangement using grid pattern illumination (From Ref. 33)

The processed image I_p exhibits optical sectioning in the same fashion as a confocal microscope, provided a suitable spatial frequency of the grid is chosen. This is because in a conventional microscope only the zero spatial frequency within the transfer function does not attenuate with defocus, one will thus obtain an optically sectioned image of the object with the grid pattern superimposed. The rate of attenuation with defocus will depend on the particular spatial frequency of the grid that is projected onto the object. The fundamental issue to be addressed is how to remove the unwanted grid pattern from the optically sectioned image. If v denotes the spatial frequency of the grating, β denotes the magnification between the grid plane and the specimen plane, the normalized axial intensity response is given by

$$I_p(z) = \left| \frac{2J_1[uv_n(1 - v_n/2)]}{uv_n(1 - v_n/2)} \right|^2 \tag{1.4}$$

where z is the axial position,

$$v_n = \beta\lambda v / NA$$

$$u = \frac{8\pi}{\lambda} zn \sin^2\left(\sin^{-1} \frac{NA}{n} / 2 \right)$$

The theoretical and measured optical sectioning strength are reportedly up to 0.856 μm and 2.78 μm respectively for a fluorescence lifetime imaging (FLIM) microscope where the grating pitch is 8 lines per millimeter, the excitation wavelength λ=415 nm, numerical aperture NA=1.25 and refractive index of the immersion medium n=1.55 [36].

1.4 Laser speckle illumination

The idea of using speckle illumination in a phase confocal microscope was first proposed by Professor Mike Somekh [37]. In 2001 a novel non-scanning fluorescence confocal microscopy using laser speckle illumination was proposed by John Walker [38]. It uses a random time varying speckle pattern to illuminate the specimen, recording a sequence of wide-field fluorescence images I_{im} and a sequence of corresponding speckle illumination patterns S. These recorded images are then processed by the averaging formula,

$$I_p(x,y,z) = \langle I_{im}(x,y,z) S(x,y,z) \rangle - \langle I_{im}(x,y,z) \rangle \langle S(x,y,z) \rangle \tag{1.5}$$

It was shown in [38] that the processed image I_p would be equivalent to a confocal image with enhanced lateral resolution and depth discrimination if an *infinite* ensemble of frames were used. The theory of this method will be given in section 2.4. Here the physical significance of Eq. (1.5) is provided as the following:

The dynamic speckles falling on the specimen can be thought of as acting like the illumination spots in a tandem scanning confocal microscope. The multiplication of each fluorescent frame I_{im} by the same illumination speckle pattern S mimics the returning fluorescent light from the specimen passed through the individual pinholes in a Nipkow disk. The difference is that the speckles are random in both position and in intensity, hence an average over a large number of speckle patterns must be obtained. Depth discrimination occurs because parts of the sample away from the focal plane are illuminated by the speckles formed in that plane. Since these speckles are different, due to the fact that the speckle pattern associated with the sample is three-dimensional in space, I_{im} is no longer correlated with S, and the ensemble of their product (the first term) tends to the multiplication of their ensembles (the second term), leaving a null image I_p.

This method avoids the scanning system and pinhole required in a conventional CSM but retains the advantages of confocal microscopy. Experiments to confirm the practicality and effectiveness of this method were made recently [39, 40]. Detailed discussions of this method will be given in the following chapters.

1.5 Remarks

An important feature of laser confocal scanning microscopes is the capability of depth discrimination. This depth response derives from the use of a point detector and is especially useful in the tomographic observation of thick fluorescent specimens. In many applications, however it is not possible to use as small a detector as we would like because of signal to noise problems. This is particularly true in fluorescent imaging because the signal level is weak. The optical sectioning becomes progressively worse as the pinhole size becomes larger (see Page 114 of Ref. 46). On the other hand, the signal to noise ratio of the image increases as the pinhole size increases, reaches a maximum value for an optimum pinhole size, and then decreases as the pinhole is made larger.

Tandem scanning is an elegant solution to the scan-time problem. The first version of this design suffered from the poor transmission of illumination through the disc. However, this problem has been alleviated by a recent design that uses microlenses to focus 40% of the illuminating light through the pinholes. This system, has found wide utility among cell biologists. Because the size of pinholes is fixed, resolution is necessarily worse when using lower power objectives compared with the LSCM system where the pinhole size is adjustable [41].

Structured-light and laser speckle illumination techniques require no scanning and have the potential to rapidly acquire data with a high signal-to-noise ratio. Standing wave fluorescence microscopy (SWFM) is a wide-field technique which provides high axial resolution in thin, fluorescently labelled specimens. However, this method does not extend the lateral resolution. A weakness of SWFM is that its optical transfer function contains large gaps between the central band and the sidebands, the so-called “information gap” [42].

Grid pattern illumination does permit optically sectioned images to be obtained but no information on the improved lateral resolution has been reported. Furthermore, practical applications of structured illumination microscopy often suffer from artefacts that can be observed as residual stripe patterns due to the inaccurate grating shifts, non-sinusoidal grating patterns or fluctuation of excitation light during acquisition [43].

Speckle illumination system makes it possible to perform wide-field fluorescence confocal imaging with minimal modification to a conventional microscope without the signal-to-noise problem associated with the pinhole size in a scanning system. An advantage of wide-field microscopy is that the CCD camera has a quantum efficiency (QE) between 20% and 80% depending on the wavelength. However the QE of the photomultiplier used in CSMs is only 10% or less, although it has very low detector noise levels. So to obtain the same signal level, typically 400 photons per pixel as for the CCD camera, the photomultiplier would require 4000 photons in a single scan. This is usually not possible for a fluorescence CSM.

Laser speckle illumination seems superior to other illumination techniques in the sense that it provides a fully confocal imaging response. However this is at the price of recording a huge number of frames, so that the recording time could be very long. The attractiveness with this method would rely on the frame rate of the recording device (CCD). Since current CCD technology allows a frame rate of 291 frames/s at the resolution of 480×640 pixels to be reached (C7770, Hamamatsu Photonics), imaging with speckle illumination on the second scale should be possible if the image obtained by averaging over 500 frames has an acceptable visual quality. With the advent of spatial light modulator technology, it is possible to multiply two frames optically in real time and average frames by taking a single CCD readout. An advantage of the CCD camera is that “it can integrate the signal in analogue form on the chip during a prolonged exposure, which avoids problems with digitisation errors and readout noise encountered when accumulating an image by averaging successive noisy individual frames in digital memory [44]”, thus increasing the attractiveness of this method.

2. Image formation

"Everything should be made as simple as possible, but not simpler."

— Albert Einstein, 1879 - 1955

There is an extensive literature [45-47] on the theory of image formation in confocal microscopes, based on either the scalar or the vector far-field diffraction imaging theory depending on whether a low-aperture or a high-aperture system is considered. In this chapter calculations are made for both the cases by using the existing theory to obtain the *point spread function* (response to a point source) in a fluorescence confocal system. It should be noted that the size of the pinhole in a scanning system is assumed to be ideally small, although this will cause signal-to-noise problems in fluorescence imaging, and the optical systems involved are assumed aberration-free.

2.1 Scanning fluorescence confocal microscopy

As illustrated in Fig. 2.1, if we denote by O the spatial distribution of the fluorescence generation, we can write the intensity just behind the object as proportional to $|h_1|^2 O$, where h_1 is the amplitude point response of the first lens imaging at a wavelength of λ_1. This intensity is then imaged at the fluorescence wavelength, λ_2, by the second lens. For circular pupils the confocal image intensity is given by

$$I = \left| h_1(u,v) h_2(u/\beta, v/\beta) \right|^2 \otimes O \tag{2.1}$$

where h_2 is the amplitude point response of the second lens, $\beta = \lambda_2 / \lambda_1$ ($\lambda_2 > \lambda_1$ due to the Stokes shift) is the ratio of the wavelengths. The *optical units*

$$u = \frac{2\pi}{\lambda_1} z \sin^2 \alpha \qquad v = \frac{2\pi}{\lambda_1} r \sin \alpha \tag{2.2}$$

where z is the defocus distance of the object, r the radial coordinate, α the semi-angle of aperture.

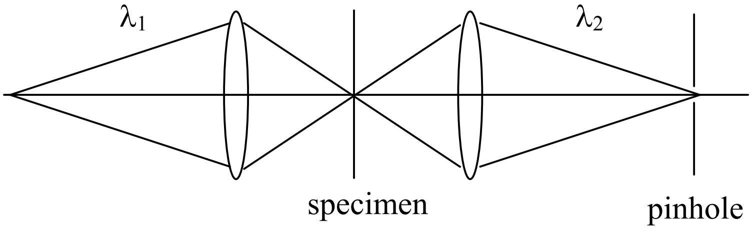

Fig. 2.1. Schematic of scanning fluorescence confocal microscopy

2.1.1 Low-aperture case

Assuming both lens have an identical small angular aperture, the scalar theory is then applicable. Based on Fraunhofer's approximation, the amplitude point response can be written as

$$h(u,v) = 2\int_0^1 P(\rho)\exp(-\frac{1}{2} ju\rho^2) J_0(v\rho)\rho \mathrm{d}\rho \tag{2.3}$$

where P is the pupil function defined as

$$P(\rho) = \begin{cases} 1, & 0 \le \rho \le 1 \\ 0, & \rho > 1 \end{cases} \tag{2.4}$$

J_0 is the Bessel function of the zeroth order. If the object consists of a point source, then the image is given by

$$I(u,v) = | h(u,v) h(u/\beta, v/\beta) |^2 \tag{2.5}$$

Fig. 2.2 shows such an image in a system with $\lambda_1 = 0.5\,\mu\mathrm{m}$, $\lambda_2 = 0.6\,\mu\mathrm{m}$ and the numerical aperture taking different values. Note that Fig. 2.2(b) is just for comparison with the vector solution to be discussed later. Compared with conventional fluorescence microscopy, the central peak of the confocal response is sharpened by a factor of 1.4 (measured at half-peak intensity).

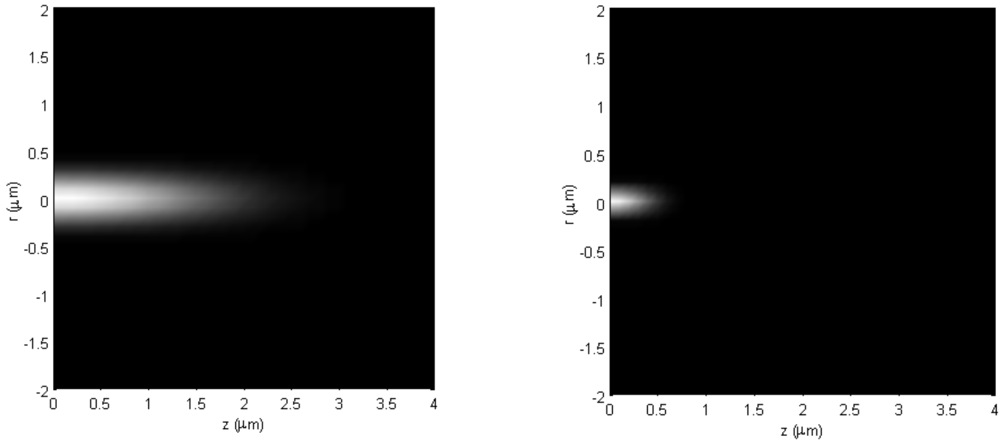

(a) $NA = 0.5$ (b) $NA = 1$

Fig. 2.2. Image of a single point source in a fluorescence confocal microscope with scalar solution

2.1.2 *High-aperture case*

For high-aperture incoherent systems, the vector solution should be used [48, 49]. Consider an optical system of revolution, which images a point source at infinity on the optical axis. The source is assumed to give rise to a linearly polarised monochromatic wave, with the electric vector E in the x-direction. The vector can be divided into a linear combination of a component within the meridional plane, $E_{||}$, plus a component perpendicular to it, $E_{\perp}$, as illustrated in Fig. 2.3(a). After undergoing refraction, the parallel part $E_{||}$ is bent by θ, while the perpendicular part $E_{\perp}$ suffers no change. The bent vector E_{θ}' at the exit pupil now exhibits also a part in the direction of the z-axis, E_z, as shown in Fig. 2.3(b) [50]. The components of the field vectors at a point P in the image region are given by

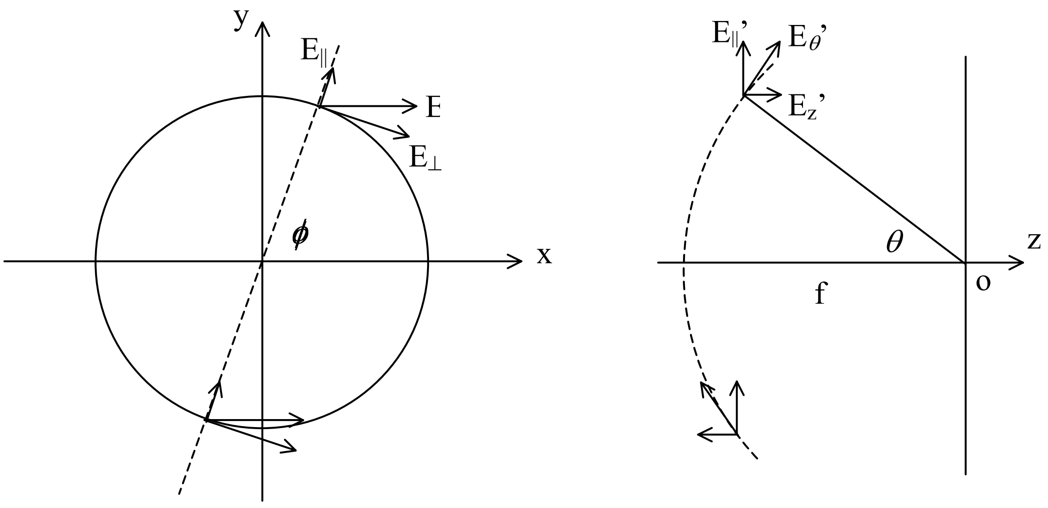

(a) The lateral plane (b) The meridional plane

Fig. 2.3 A schematic diagram for vector solution

$$E_x = -iA(I_0 + I_2 \cos 2\phi) \tag{2.6.1}$$

$$E_y = -iA(I_2 \sin 2\phi) \tag{2.6.2}$$

$$E_z = -2A(I_1 \cos\phi) \tag{2.6.3}$$

where A is a constant, ϕ is the azimuth and

$$I_0(u,v) = \int_0^{\alpha} \sqrt{\cos\theta}\, \sin\theta (1+\cos\theta) J_0\left(\frac{\sin\theta}{\sin\alpha} v\right) \exp\left(j \frac{\cos\theta}{\sin^2\alpha} u\right) \mathrm{d}\theta \tag{2.7.1}$$

$$I_1(u,v) = \int_0^{\alpha} \sqrt{\cos\theta}\, \sin^2\theta J_1\left(\frac{\sin\theta}{\sin\alpha} v\right) \exp\left(j \frac{\cos\theta}{\sin^2\alpha} u\right) \mathrm{d}\theta \tag{2.7.2}$$

$$I_2(u,v) = \int_0^{\alpha} \sqrt{\cos\theta}\, \sin\theta (1-\cos\theta) J_2\left(\frac{\sin\theta}{\sin\alpha} v\right) \exp\left(j \frac{\cos\theta}{\sin^2\alpha} u\right) \mathrm{d}\theta \tag{2.7.3}$$

where J_0, J_1 and J_2 are the Bessel functions of the first kind. For small semi-angle α, $J_n(x) \approx x^n$, I_1 and I_2 are of lower order than I_0, so that they may be neglected in comparison with I_0. Invoking

$$\sin\theta \approx \theta$$

$$\cos\theta \approx \begin{cases} 1-\theta^2/2 & \text{in the phase of equation 2.7} \\ 1 & \text{elsewhere} \end{cases}$$

$$\rho = \theta / \sin\alpha$$

equation (2.7.1) is then reduced to equation (2.3), the usual scalar solution, resulting in the electric field in the image region being linearly polarised in the same direction of the incoming wave. For large semi-angle, I_1 and I_2 cannot be neglected, the effect of field components E_y and E_z becomes significant, thus causing the point spread function to be asymmetric about the axis of the system.

The situation is quite different for fluorescence imaging. The fluorescent radiation is completely incoherent and randomly polarised. The time-averaged intensity distribution may be obtained by averaging the polarised fields over all possible states of polarisation. After carrying out this averaging and by assuming that the excitation light is circularly polarised [51], the intensity point response of the first and second lens can be expressed as

$$w_1(u,v) = w_2(u,v) = w(u,v) = |I_0(u,v)|^2 + 2|I_1(u,v)|^2 + |I_2(u,v)|^2 \tag{2.8}$$

Note that the above expression is independent of ϕ, meaning that the point spread function is circularly symmetric. The image of a point source in a high-aperture fluorescence confocal microscope is then given by

$$I(u,v) = w(u,v)w(u/\beta, v/\beta) \tag{2.9}$$

Calculations are made for a system with $\lambda_1 = 0.5\ \mu\text{m}$, $\lambda_2 = 0.6\ \mu\text{m}$ and the numerical aperture taking different values. The results are shown in Fig. 2.4. It may be seen that for the case of NA=0.5 the scalar solution is consistent with the vector one, but for the case of NA=1 the scalar theory underestimates the correct diffraction limit. It is natural to ask at what NA the scalar theory is no longer applicable. The consensus (see, for example, Ref. [52]) is that the scalar approximation is good up to a NA value of 0.5.

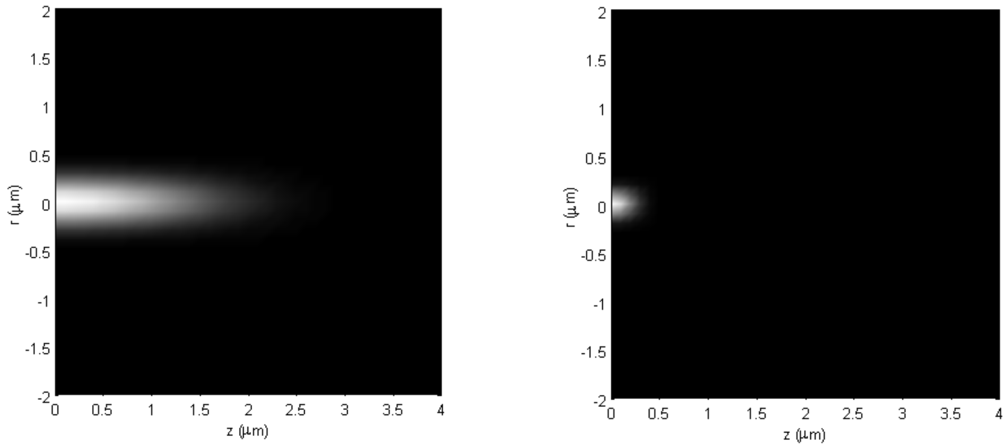

(a) $NA = 0.5$ (b) $NA = 1$

Fig. 2.4. Image of a single point source in a fluorescence confocal microscope with vector solution

2.2 Depth discrimination property

If we scan a uniform fluorescent planar object through focus, i.e., we set $O = \delta(u - u')$, where δ is a delta function, *u*' is a specified focal position, then the power, or the integrated intensity, in the image, is given by

$$I_{\text{int}}(u) = \int_0^\infty \left| h(u,v) h(u/\beta, v/\beta) \right|^2 v \mathrm{d}v \tag{2.10}$$

for the low-aperture case or by

$$I_{\text{int}}(u) = \int_0^\infty w(u,v) w(u/\beta, v/\beta) v \mathrm{d}v \tag{2.11}$$

for the high-aperture case. Note that the prime of *u* has been dropped. The depth discrimination property can be evaluated in terms of the ratio of the out-of-focus integrated intensity to the in-focus integrated intensity:

$$I_{\text{int}}(u) / I_{\text{int}}(0) \tag{2.12}$$

The full-width at half-maximum (FWHM) for the curve thus obtained versus z-direction is defined to be the *axial resolution*. Calculations are made using (2.10), (2.11) and (2.12) for both the low-aperture and high-aperture systems. The results are shown in Figs. 2.5 and 2.6 respectively. It may be observed that high-aperture systems give better axial resolution.

2.3 Lateral resolution

By setting $u = 0$ in (2.3), we get the image intensity distribution of a single point source at the focal plane in a low-aperture system:

$$I(v) = \left[4 \frac{J_1(v)}{v} \cdot \frac{J_1(v/\beta)}{v/\beta} \right]^2 \tag{2.13}$$

The optimal resolution is achieved if $\beta = 1$. Fig. 2.7 and Fig. 2.8 show the image intensity distribution of an in-focus single point source, obtained via scalar and vector approaches respectively. As for the axial resolution, the FWHM for the distribution versus radial direction is defined to be the lateral resolution.

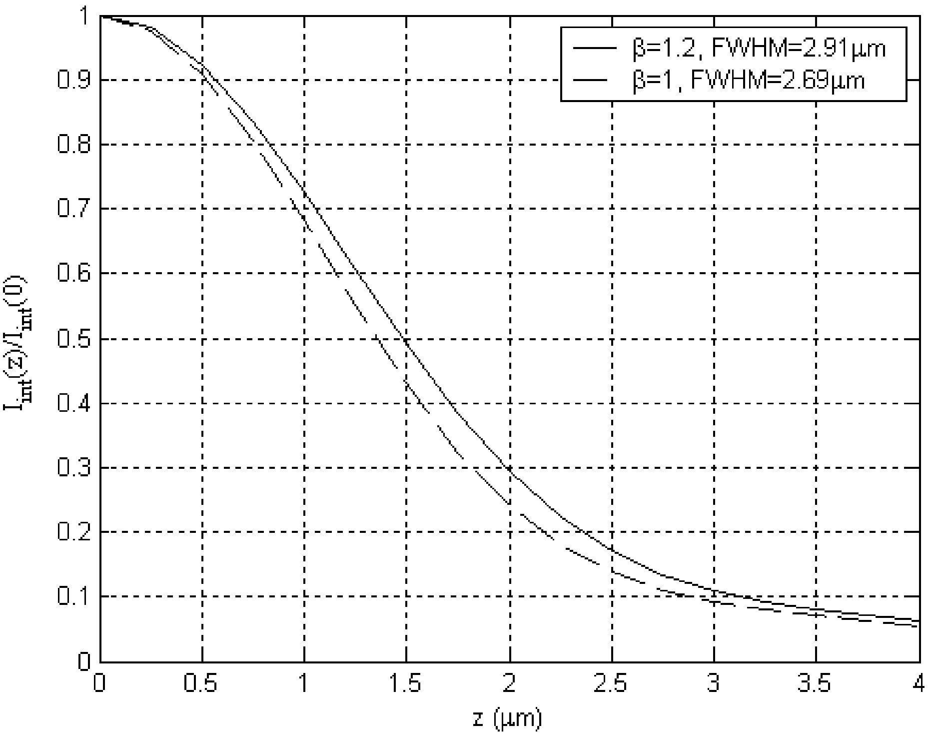

Fig. 2.5. Depth discrimination property with the scalar solution ($\lambda_1 = 0.5\ \mu$m, $NA = 0.5$)

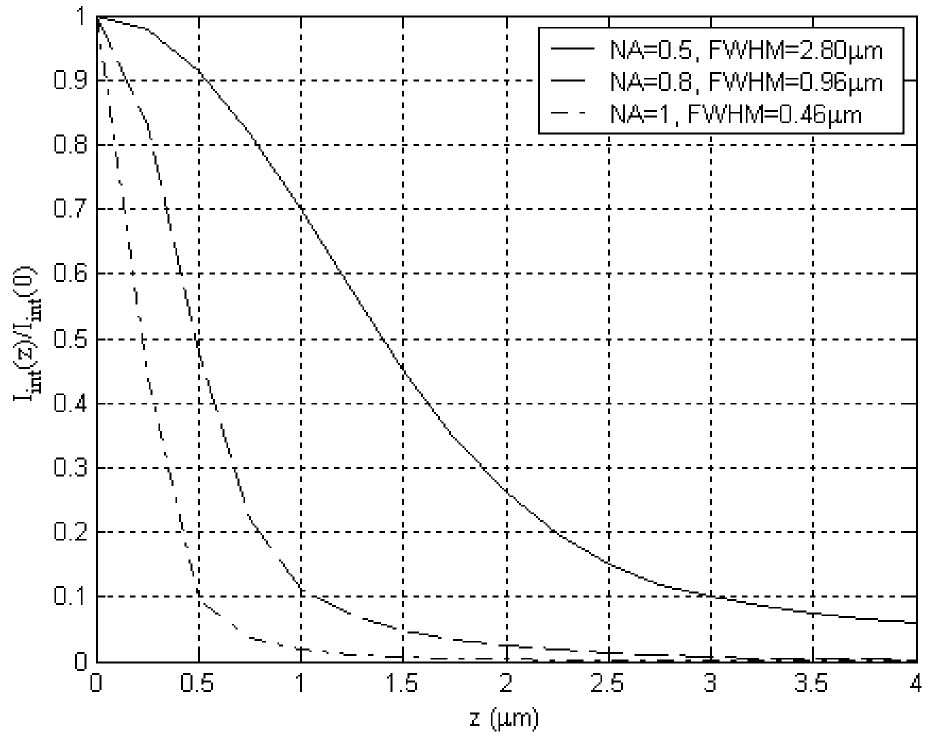

Fig. 2.6. Depth discrimination property with the vector solution ($\lambda_1 = 0.5\ \mu$m, $\lambda_2 = 0.6\ \mu$m)

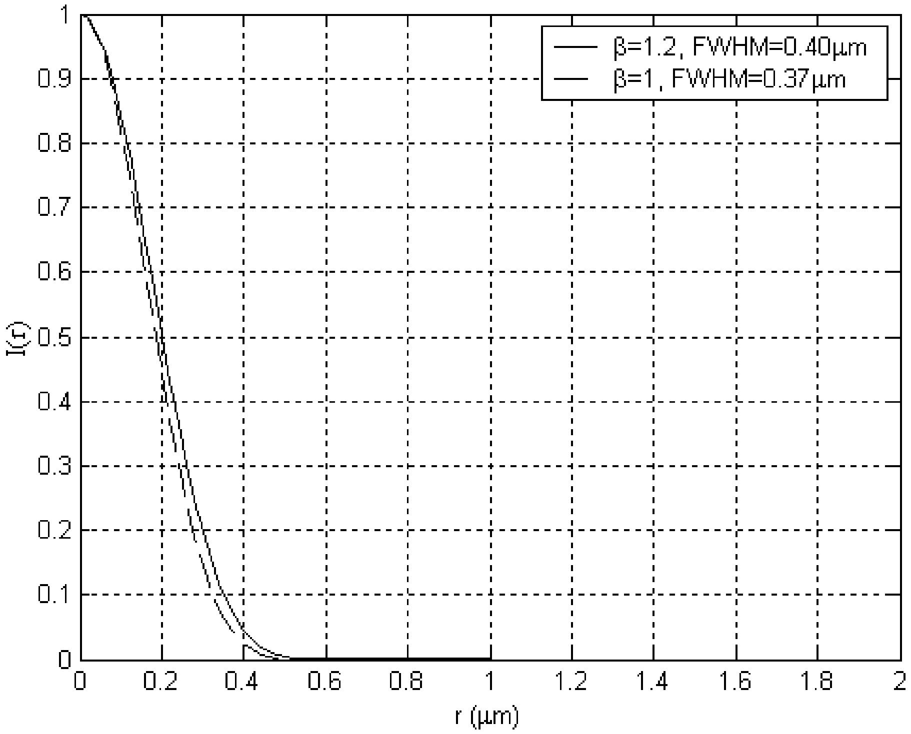

Fig. 2.7. Image intensity distribution for a single point source with the scalar solution ($\lambda_1 = 0.5\ \mu\text{m}$, $NA = 0.5$)

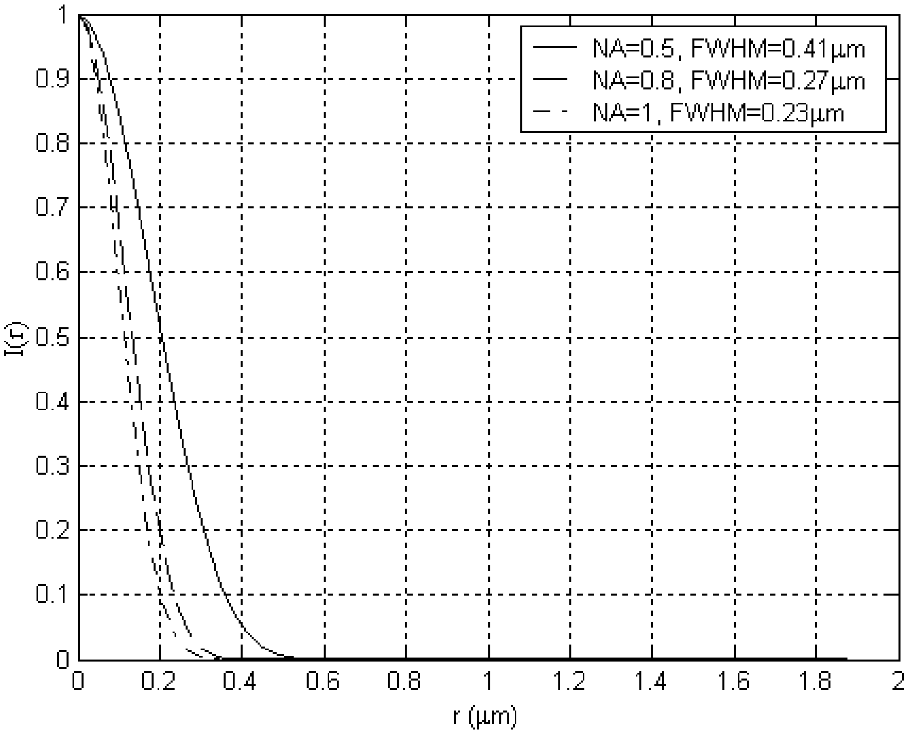

Fig. 2.8. Image intensity distribution for a single point source with the vector solution ($\lambda_1 = 0.5\ \mu\text{m}$, $\lambda_2 = 0.6\ \mu\text{m}$)

2.4 Non-scanning fluorescence confocal microscopy using speckle illumination

The optical arrangement for non-scanning fluorescence confocal microscopy is illustrated in Fig. 2.9. Illumination from an expanded laser beam is passed through a rotating diffuser so that a time-varying Gaussian speckle pattern is formed throughout the specimen region. The dichroic beam splitter directs a portion of the scattered light at wavelength λ_1 to the reference detector. The fluorescent light from the object at a longer wavelength λ_2 is imaged onto the imaging detector. By selecting the appropriate Cartesian coordinates shown in the figure, the intensity falling on the imaging detector can be expressed by

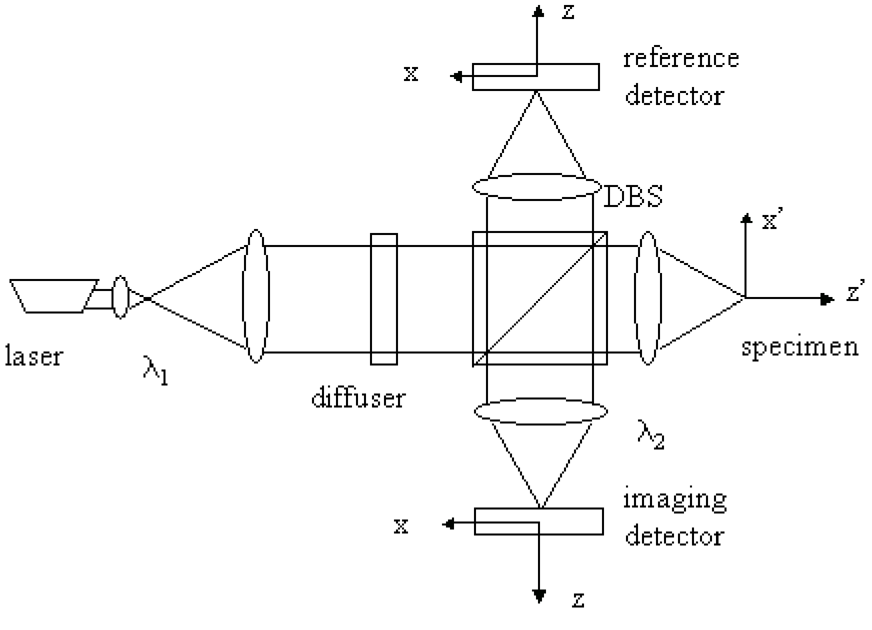

Fig. 2.9. A schematic diagram of the optical arrangement (From Ref. 38)

$$I_{im}(x,y,z)=\iiint O(x',y',z')S(x',y',z')\,|\,h_2(x-x',y-y',z-z')\,|^2\ \mathrm{d}x'\mathrm{d}y'\mathrm{d}z' \tag{2.14}$$

where O is the fluorophore concentration, h_2 is the amplitude point response of the imaging lens at λ_2, which in the low aperture case may be written as

$$h_2(x,y,z)=\iint P(x_1,y_1)\exp(-\frac{i\pi z}{\lambda_2 f^2}(x_1^2+y_1^2))\exp(-\frac{i2\pi}{\lambda_2 f}(xx_1+yy_1))\mathrm{d}x_1\mathrm{d}y_1 \quad (2.15)$$

S is the speckle intensity in the object region given by

$$\begin{aligned}S(x',y',z')=|\iint P(x_1,y_1)\exp(i\phi(x_1,y_1))\exp(-\frac{i\pi z'}{\lambda_1 f^2}(x_1^2+y_1^2))\\ \exp(-\frac{i2\pi}{\lambda_1 f}(x'x_1+y'y_1))\mathrm{d}x_1\mathrm{d}y_1|^2\end{aligned} \quad (2.16)$$

where P is the pupil function of the imaging lens, f is the focal length and ϕ is the phase introduced by the diffuser. The intensity falling on the reference detector I_{ref} has the same form as (2.16):

$$I_{ref}(x,y,z)=S(x,y,z) \quad (2.17)$$

If an infinitive ensemble of frames is recorded and then processed by the formula

$$I_p(x,y,z)=\langle I_{im}(x,y,z)I_{ref}(x,y,z)\rangle-\langle I_{im}(x,y,z)\rangle\langle I_{ref}(x,y,z)\rangle \quad (2.18)$$

where the angular brackets represent averaging over the sequence of frames, the processed image I_p will be identical to the response from a scanning fluorescence confocal microscope:

$$I_p(x,y,z)=O\otimes|h_1h_2|^2 \quad (2.19)$$

where h_1 is the amplitude point response of the imaging lens at λ_1:

$$h_1(x,y,z)=\iint P(x_1,y_1)\exp(-\frac{i\pi z}{\lambda_1 f^2}(x_1^2+y_1^2))\exp(-\frac{i2\pi}{\lambda_1 f}(xx_1+yy_1))\mathrm{d}x_1\mathrm{d}y_1 \quad (2.20)$$

The physical basis of equation 2.18 was explained in Chapter 1 following equation 1.5. The derivation of (2.19) from formula (2.18) was first conducted by John G. Walker [38]. As the formula is of vital importance, the derivation will be given here again. By inserting (2.14) and (2.17) into (2.18) and bringing the averaging brackets inside the integral, equation (2.18) may be written as

$$\begin{aligned}I_p(x,y,z)=\iiint O(x',y',z')h_2(x-x',y-y',z-z')|^2\\ [\langle S(x,y,z)S(x',y',z')\rangle-\langle S(x,y,z)\rangle\langle S(x',y',z')\rangle]\mathrm{d}x'\mathrm{d}y'\mathrm{d}z'\end{aligned} \quad (2.21)$$

The speckle pattern intensity S is related to the complex amplitude u by

$$S(x,y,z) = |u(x,y,z)|^2 \tag{2.22}$$

and u is a circular complex Gaussian random variable because it is the sum of a large number of random phasors, each arising from a different scattering point on the surface of the diffuser. By making use of the Gaussian moment theorem (see Eq. (3.9-3) on page 109 of Ref. [53]), the term inside the square brackets in (2.21) can be expressed as

$$\begin{aligned}&\langle S(x,y,z)S(x',y',z')\rangle - \langle S(x,y,z)\rangle\langle S(x',y',z')\rangle \\ &= |\langle u(x,y,z)u^*(x',y',z')\rangle|^2\end{aligned} \tag{2.23}$$

where $\langle u(x,y,z)u^*(x',y',z')\rangle$ is a statistical autocorrelation function (see Eq. (3.8-30) on page 106 of Ref. [53]) which measures the statistical similarity of $u(x,y,z)$ and $u(x',y',z')$ over the ensemble. The complex amplitude u is related to the pupil function by

$$\begin{aligned}u(x,y,z) = \iint P(x_1,y_1)\exp(i\phi(x_1,y_1))\exp(-\frac{i\pi z}{\lambda_1 f^2}(x_1^2+y_1^2)) \\ \exp(-\frac{i2\pi}{\lambda_1 f}(xx_1+yy_1))\mathrm{d}x_1\mathrm{d}y_1\end{aligned} \tag{2.24}$$

Substituting (2.24) into (2.23), we have

$$\begin{aligned}&\langle S(x,y,z)S(x',y',z')\rangle - \langle S(x,y,z)\rangle\langle S(x',y',z')\rangle \\ &= |\iint\iint P(x_1,y_1)P^*(x_2,y_2)\langle\exp(i(\phi(x_1,y_1)-\phi(x_2,y_2)))\rangle \\ &\exp(-i\pi(z(x_1^2+y_1^2)-z'(x_2^2+y_2^2))/\lambda_1 f^2) \\ &\exp(-i2\pi(xx_1+yy_1-x'x_2-y'y_2)/\lambda_1 f)\mathrm{d}x_1\mathrm{d}y_1\mathrm{d}x_2\mathrm{d}y_2|^2\end{aligned} \tag{2.25}$$

The averaged term in the above equation represents also a statistical autocorrelation. For a diffuser with a scale of roughness much smaller than its pupil diameter, the averaged term can be approximated to a Dirac-delta function:

$$\langle\exp(i(\phi(x_1,y_1)-\phi(x_2,y_2)))\rangle = \delta(x_1-x_2, y_1-y_2) \tag{2.26}$$

Inserting (2.26) into (2.25) and integrating with respect to x_2 and y_2 leads to

$$\begin{aligned}&\langle S(x,y,z)S(x',y',z')\rangle - \langle S(x,y,z)\rangle\langle S(x',y',z')\rangle \\ &= \left| \iint |P(x_1,y_1)|^2 \exp(-i\pi(z-z')(x_1^2+y_1^2)/\lambda_1 f^2) \right. \\ &\left. \exp(-i2\pi((x-x')x_1+(y-y')y_1)/\lambda_1 f)\mathrm{d}x_1\mathrm{d}y_1 \right|^2\end{aligned} \tag{2.27}$$

which, compared with (2.20), can be replaced by $|h_1(x-x',y-y',z-z')|^2$. Hence equation (2.21) becomes

$$\begin{aligned}I_p(x,y,z) = \iiint O(x',y',z')\,&|h_1(x-x',y-y',z-z') \\ &h_2(x-x',y-y',z-z')|^2\ \mathrm{d}x'\mathrm{d}y'\mathrm{d}z'\end{aligned} \tag{2.28}$$

which is a convolution operation and can be denoted by equation (2.19).

Of course, in reality only a finite number of frames in (2.18) may be used and the resulting image will be imperfect.

3. Simulation

"Well begun is half done."

— Aristotle, 384 – 322 BC

This chapter aims to investigate the simulated behaviour of a non-scanning system with finite frame averaging using formula (2.18). The effects of shot noise, additive white noise and quantisation present in a CCD detector are also investigated. The simulation is restricted to the low-aperture case ($NA \leq 0.5$) and the optical systems involved are assumed aberration-free, so that standard Fourier optics approach can be used.

3.1 Fourier optics approach

Assuming the object is infinitely thin and imaged at an arbitrary focal position, the fluorophore concentration in (2.14) can be written as

$$O'(x',y',z') = O(x',y')\delta(z'-\Delta z) \tag{3.1}$$

where δ is a delta function, Δz is the defocus distance. Inserting (3.1) into (2.14), the image observed at position $z = 0$ can then be expressed by

$$\begin{aligned} I_{im}(x,y,0) &= \iiint O(x',y')\delta(z'-\Delta z)S(x',y',z') \\ &\qquad |\, h_2(x-x',y-y',-z')\,|^2 \; \mathrm{d}x'\mathrm{d}y'\mathrm{d}z' \\ &= \iint O(x',y')S(x',y',\Delta z)\,|\, h_2(x-x',y-y',\Delta z)\,|^2 \mathrm{d}x'\mathrm{d}y' \\ &= (O(x,y)S(x,y,\Delta z)) \otimes |\, h_2(x,y,\Delta z)\,|^2 \end{aligned} \tag{3.2}$$

This is a two-dimensional convolution operation but can be converted into a multiplication operation in the Fourier space:

$$I_{im}(x,y,0) = F^{-1}\{F\{O(x,y)S(x,y,\Delta z)\}F\{|\, h_2(x,y,\Delta z)\,|^2\}\} \tag{3.3}$$

In most cases the pupil function is radially symmetrical. By changing the Cartesian coordinates to polar coordinates, the amplitude point response in (2.20) or (2.15) will be reduced to a one-dimensional integral

$$h(r,z) = 2\pi\int_0^\infty P(r_1)\exp(-\frac{ikr_1^2}{2f^2}z)J_0(\frac{kr_1r}{f})r_1dr_1 \tag{3.4}$$

where $k = 2\pi/\lambda$ is the wave number, $r_1 = \sqrt{x_1^2 + y_1^2}$, $r = \sqrt{x^2 + y^2}$. If we denote by a the radius of the pupil, let $\rho = r_1/a$, $\sin\alpha = a/f$, and normalise by dividing by the pupil area πa^2, integral (3.4) will have the same form as (2.3) and is also termed *Fourier-Bessel transform* or *Hankel transform* [54]. Since the analytical form of the transform is not available except when $z = 0$, thus giving $h(r,0) = 2J_1(kar/f)/(kar/f)$, the amplitude point response can be found numerically by taking the two-dimensional Fourier transform of the *effective pupil function* [55]

$$P_{eff}(x_1, y_1) = P(x_1, y_1)\exp(-\frac{i\pi(x_1^2 + y_1^2)}{\lambda f^2}\Delta z) \tag{3.5}$$

So, the amplitude point response at λ_1 can be written as

$$h_1(m,n,\Delta z) = F\{P(x_1, y_1)\exp(-\frac{i\pi(x_1^2 + y_1^2)}{\lambda_1 f^2}\Delta z)\} \tag{3.6}$$

where $m = x/\lambda_1 f$ and $n = y/\lambda_1 f$ are the spatial frequency components. To obtain $h_2(m,n,\Delta z)$, we rewrite (2.15) as

$$h_2(x, y,\Delta z) = \iint P(x_1, y_1)\exp(-\frac{i\pi\Delta z}{\lambda_2 f^2}(x_1^2 + y_1^2))\exp(-\frac{i2\pi}{\lambda_1 f}(x\frac{x_1}{\beta} + y\frac{y_1}{\beta}))\mathrm{d}x_1\mathrm{d}y_1$$

where β is the ratio of the wavelengths as defined in Chapter 2, or

$$h_2(x,y,\Delta z)=\iint P(\beta x_1,\beta y_1)\exp(-\frac{i\pi\Delta z\beta^2}{\lambda_2 f^2}(x_1^2+y_1^2))$$
$$\exp(-\frac{i2\pi}{\lambda_1 f}(xx_1+yy_1))\mathrm{d}x_1\mathrm{d}y_1 \tag{3.7}$$

It is useful to define $x_2=x_1/a$, $y_2=y_1/a$ and to change the integration to variables of these new dimensionless variables. This leads to

$$h_2(x,y,\Delta z)=\iint P'(\beta x_2,\beta y_2)\exp(-\frac{i\pi\Delta z\beta^2 N^2}{\lambda_2}(x_2^2+y_2^2))$$
$$\exp(-\frac{i2\pi N}{\lambda_1}(xx_2+yy_2))\mathrm{d}x_2\mathrm{d}y_2 \tag{3.8}$$

where $N=a/f$ is the numerical aperture of the objective (within the Fourier approximation) and $P'(x_2,y_2)$ is a scaled version of the pupil function, such that $P'(x_2,y_2)=0$ for $\sqrt{x_2^2+y_2^2}\geq 1$. It may be seen from (3.8) that the lens radius a has disappeared from the equation and that the form of h_2 depends only on N, λ_1, Δz and β. Equation (3.8) may be written as

$$h_2(m,n,\Delta z)=F\{P'(\beta x_2,\beta y_2)\exp(-\frac{i\pi\beta^2 N^2(x_2^2+y_2^2)}{\lambda_2}\Delta z)\} \tag{3.9}$$

Analogously, equation (3.6) may be written as

$$h_1(m,n,\Delta z)=F\{P'(x_2,y_2)\exp(-\frac{i\pi N^2(x_2^2+y_2^2)}{\lambda_1}\Delta z)\} \tag{3.10}$$

Comparing (3.9) with (3.10), it may be seen that keeping the coordinates of h_2 the same as h_1 in the Fourier space leads to a *contraction* of the coordinates of the second lens' effective pupil function in the $x_2\,y_2$ space by a factor of $1/\beta$.

Using (2.16) and (2.17), the speckle intensity S and the reference speckle pattern I_{ref} can also be expressed by

$$S(m,n,\Delta z)=|F\{P'(x_2,y_2)\exp(i\phi(x_2,y_2)\exp(-\frac{i\pi N^2(x_2^2+y_2^2)}{\lambda_1}\Delta z)\}|^2 \tag{3.11}$$

$$I_{ref}(m,n,0) = |\,F\{P'(x_2,y_2)\exp(i\phi(x_2,y_2))\}\,|^2 \tag{3.12}$$

Based on (3.3), (3.9), (3.10), (3.11), (3.12), the averaging formula (2.18) and expression (2.19), a computer programme coded in MATLAB is written to simulate optical fluorescence imaging in a conventional microscope, a confocal scanning microscope and a non-scanning confocal microscope respectively. In this programme a subroutine is frequently called to perform two-dimensional *discrete Fourier transform*. The coordinates x_2, y_2 and the spatial frequency components m and n then take the form of integers and are represented by the element indices of complex matrices.

3.2 Shot noise

Shot noise is the noise arising from the statistical distribution of the recorded photons. Its statistical property is clearly elucidated in Goodman's works [53]. When electromagnetic fields are incident on a photosurface, a complex set of events can occur. These include (1) absorption of a quantum of light energy (i.e., a photon) and the transfer of that energy to an excited electron, (2) transport of the excited electron to the surface, (3) release of the electron from the surface. The release of such an electron from the photosurface is referred to as a *photoevent*, which obeys *Poisson impulse process*. If K denotes the number of photoevents occurring in a given time interval, or the number of photocounts, the probability $p(K)$ that K impulses fall within the time interval can be expressed as

$$p(K) = \frac{\overline{K}^K}{K!} e^{-\overline{K}} \tag{3.13}$$

where the mean number of photoevents $\overline{K}$ is given by

$$\overline{K} = \alpha I A \tau \tag{3.14}$$

where α is a proportionality constant, I is the intensity of light incident on the photosurface of illuminated area A during the measurement time of interest τ. An important property of Poisson distribution is that its variance is equal to its mean:

$$\sigma_K^2 = \overline{K} \tag{3.15}$$

A plot of function (3.13) is shown in Fig. 3.1. The signal-to-noise ratio associated with this distribution, as defined by the ratio of mean to standard deviation, is given by

$$SNR = \frac{\overline{K}}{\sigma_K} = \sqrt{\overline{K}} \tag{3.16}$$

The uncertainty in the number of photons collected during the given period of time is simply the shot noise given by

$$\sigma_{shot} = \sigma_K = \sqrt{\overline{K}} \tag{3.17}$$

Photon shot noise is expressed in electrons. So a 10,000-electron exposure will have a shot noise of 100 electrons. This implies that the best signal-to-noise ratio possible for a 10,000-electron signal is 10,000/100 = 100.

In our simulation a MATLAB function imnoise(I, 'poisson') is used to generate shot noise from the incident intensity distribution I.

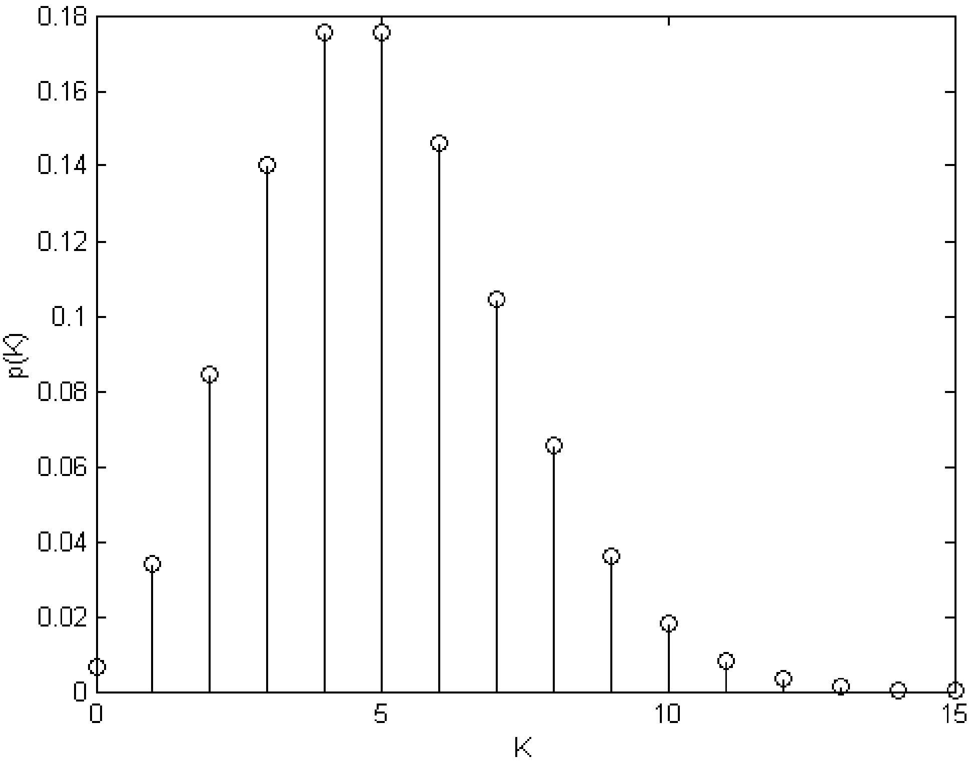

Fig. 3.1. Probability masses associated with the Poisson distribution ($\overline{K} = 5$)

3.3 Additive white noise

For a CCD image sensor, there is a noise source caused by the chaotic motion of electrons in the components of the detector, including

- *dark current* — thermally induced charge carriers
- *transfer noise* — additional or lost charge carriers due to shift of charge carriers between the registers of a CCD image sensor
- *readout noise* — caused by the amplifier processing chain and the A/D conversion process

This type of noise may be modelled as additive Gaussian noise. Gaussian noise obeys Gaussian distribution with a probability density function of the form:

$$p(x) = \frac{1}{\sqrt{2\pi\sigma^2}} \exp\left(-\frac{(x-\mu)^2}{2\sigma^2} \right) \tag{3.18}$$

where μ is the mean and σ^2 is the variance. Since the noise is signal-independent, the observable image is given by

$$I_o(x,y) = I(x,y) + n(x,y) \tag{3.19}$$

where I is the true image and n is the noise described by its mean and variance. The signal-to-noise ratio is given by

$$SNR = \sigma_s^2 / \sigma_n^2 \tag{3.20}$$

where σ_s^2 and σ_n^2 are the variances of the true image and the noise. It should be noted that the readout noise is characterized by a zero-mean Gaussian distribution. A MATLAB function imnoise(I,’Gaussian’,m,v) adds Gaussian noise of mean m and variance v to the image I. Fig. 3.2 shows the simulated image of additive white noise. The noise has a mean of 0.4 and a variance of 0.0001 as shown in Fig. 3.3. These values are chosen to emulate the performance of the CCD detector used in the experiments reported in Chapters 6 and 7.

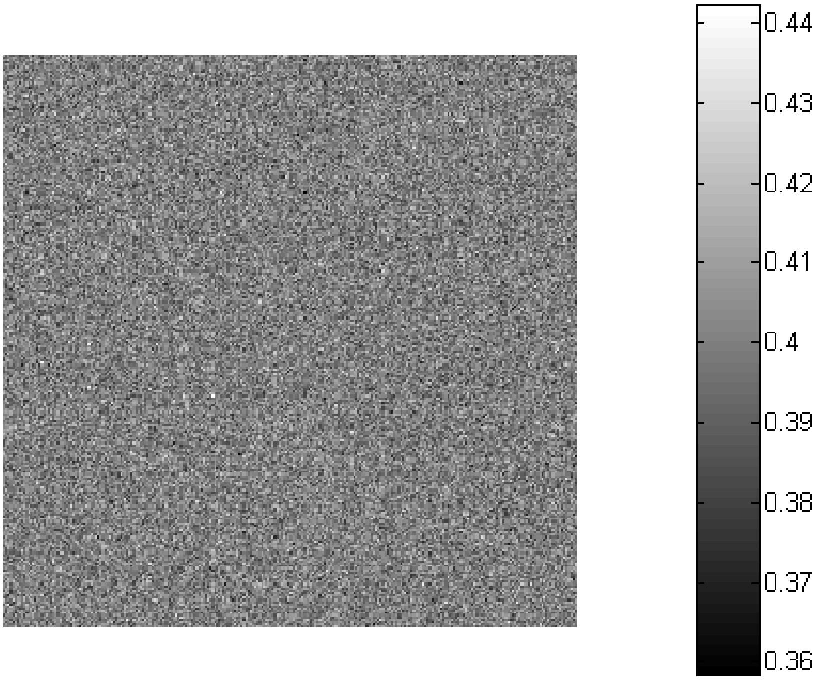

Fig. 3.2 A simulated 250×250 image of additive white noise

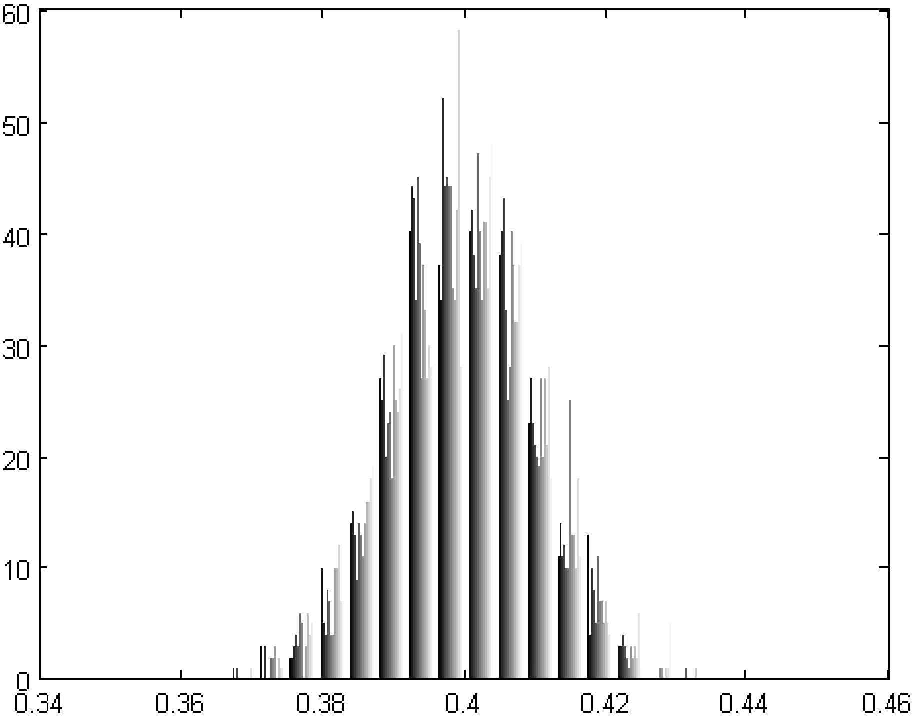

Fig. 3.3 The histogram of the image shown in Fig. 3.2

3.4 Quantisation

An optical detector converts optical energy into electrical energy in a square-law fashion — the electrical power is proportional to the square of the time-averaged optical power. A general square-law detector with an input beam of intensity I and a responsivity R will produce an output signal S given by

$$S = R\iint_{A} \langle I(x, y, t) \rangle \mathrm{d}x\mathrm{d}y \tag{3.21}$$

where angle brackets denote time averaging through the temporal response of the detector, and A is the area of the active surface of the detector. The output signal S is an analogue voltage, it is then put to the A/D converter (ADC) and a binary code is generated. The voltage range, from zero for black to some maximum value for the highest light intensity, is divided into a number of (usually) equal intervals. This process is often referred to as *quantisation*.

ADCs usually have a resolution of 8 to 12 bits corresponding to 256 to 4096 intensity grades known as *grey levels*. Each grey level can be determined by

$$I_i = \frac{I_{\max}}{2^n - 1} i \quad i = 0, 1, \cdots, 2^n - 1 \tag{3.22}$$

where i is the grey level index, and n is the number of bits of the ADC. All the pixel values within the same input interval are mapped to the same output grey level. A MATLAB function uencode(U, N) performs uniform quantisation of the input array U into N-bits.

The “round-off” error when an analogue signal is quantised is called the *quantisation error*. All ADCs have rms noise that the quantisation error generates. The rms quantisation voltage for an ADC equals $e_{rms} = q / \sqrt{12}$, where q is the LSB (least significant bit) size. As an example, the rms quantisation noise for a 8-bit ADC with a 2.5V full scale value is 2.82mV. The quantisation error is random and can be treated as white noise. The minimum levels of quantisation for the system not dominated by this error can be determined in terms of the desired signal-to-noise ratio defined by (3.20).

3.5 Results

The parameters necessary for the simulation are listed in table 3.1.

Numerical aperture N	0.5
Wavelength of illumination light λ_1	0.5 μm
Wavelength of fluorescent light λ_2	0.6 μm
Size of an individual frame	256×256 pixels
Scale factor	1 μm = 16 pixels
Defocus interval	0.5 μm

Table 3.1. Parameters for the simulation

3.5.1 Laser speckle

According to Eq. 3.11 a computer-generated laser speckle pattern is shown in Fig. 3.4. The phase variations introduced by the diffuser are *uniformly* distributed over (−π, π). The pupil function was set to unity within a pupil with a diameter of 32 pixels and zero elsewhere. It is well known that the intensity distribution in a laser speckle pattern obeys a negative-exponential probability density function given by [53]

$$p_I(I) = \begin{cases} \frac{1}{\overline{I}}\exp\left(-\frac{I}{\overline{I}}\right) & I \geq 0 \\ 0 & \text{otherwise} \end{cases} \tag{3.23}$$

Theoretically the speckle intensity I can go to infinity, but in reality it falls into a limited range [0, $I_{\max}$]. It is reasonable to set $I_{\max} = 10\bar{I}$, because in this case the probability of speckle intensity larger than $I_{\max}$ is only

$$\begin{aligned} F\{I > I_{\max}\} &= 1 - F\{I < I_{\max}\} = 1 - \int_0^{I_{\max}} p_I(x)dx \\ &= \exp(-I_{\max}/\bar{I}) = \exp(-10) \approx 0.00005 \end{aligned} \tag{3.24}$$

A histogram corresponding to the speckle pattern in Fig. 3.4 is shown in Fig. 3.5 where $\bar{I} = 793$, $I_{\max} = 6557$.

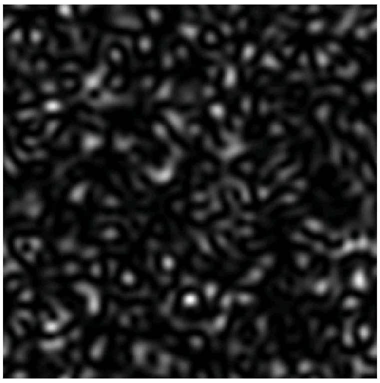

Fig. 3.4. Simulated speckle pattern

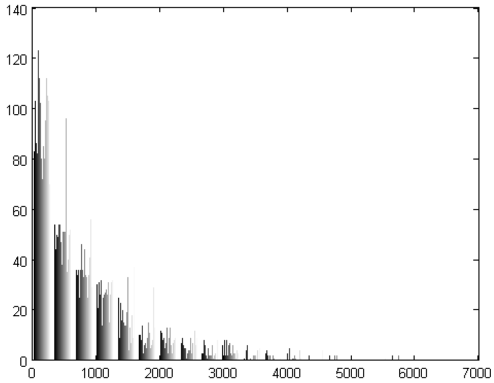

Fig. 3.5. Histogram

3.5.2 *Uniform fluorescent planar object*

A simulation result using a uniform fluorescent planar object is shown in Fig. 3.6. It may be seen that a conventional microscope (or type 1 microscope) cannot resolve axially an infinite and featureless structure which contains only dc frequency components, while a confocal microscope (or type 2 microscope) can. Non-scanning confocal microscope does provide axial resolution similar to scanning microscopes, but with unwanted intensity variations in the image. This intensity non-uniformity decreases as the number of image frames increases, as shown in Fig. 3.6(b). For validation purposes, a comparison of depth discrimination property for a scanning system between theory and simulation is shown in Fig. 3.7, where the solid line is obtained from Eq. (2.12) and the crosses from the simulated data. Quantitative assessment of the depth discrimination property and the intensity non-uniformity for a non-scanning system will be given in Chapter 4.

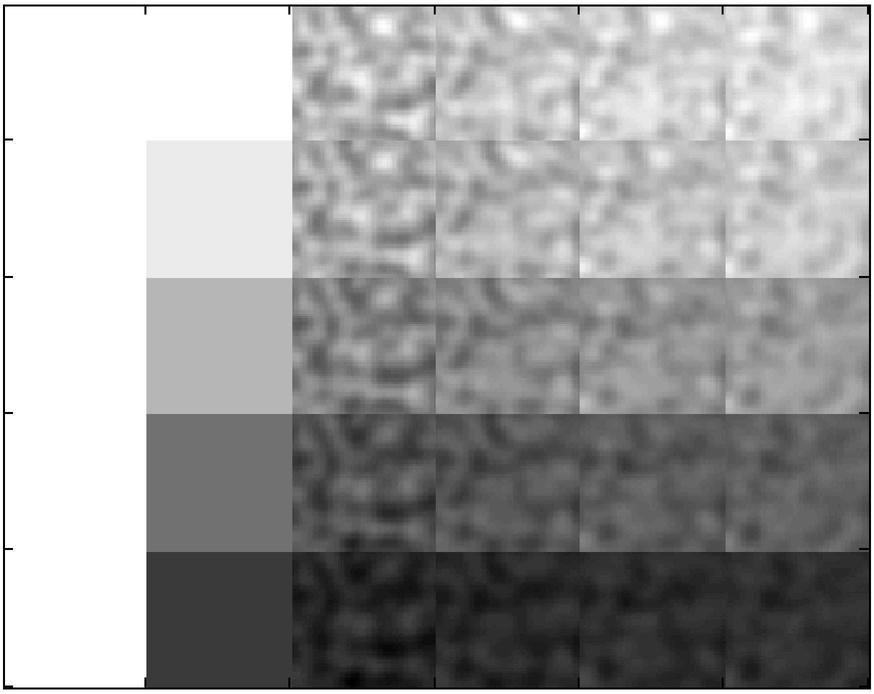

(a) For comparison purposes, the first column shows sets of images of the object at a number of focal positions generated using the calculated response from a conventional microscope. The second column shows the images using the calculated response from a fluorescence scanning confocal microscope. The third to sixth columns show a series of simulated images of the same object calculated using the formula 2.18, but averaged over 500, 1000, 1500 and 2000 independent frames. The images are shown for the in-focus case (top row) and for the object defocused by 0.5, 1, 1.5 and 2 μm respectively (rows two to five).

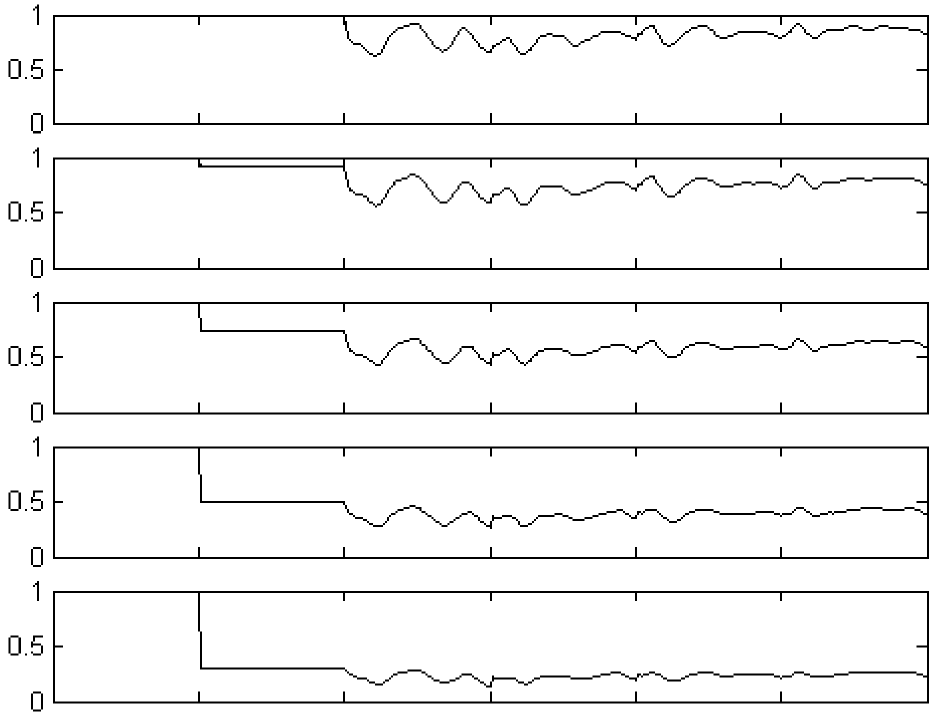

(b) The same data as in (a) but shown as a slice along the central line of each row

Fig. 3.6. Simulated results. Image of a uniform fluorescent planar object

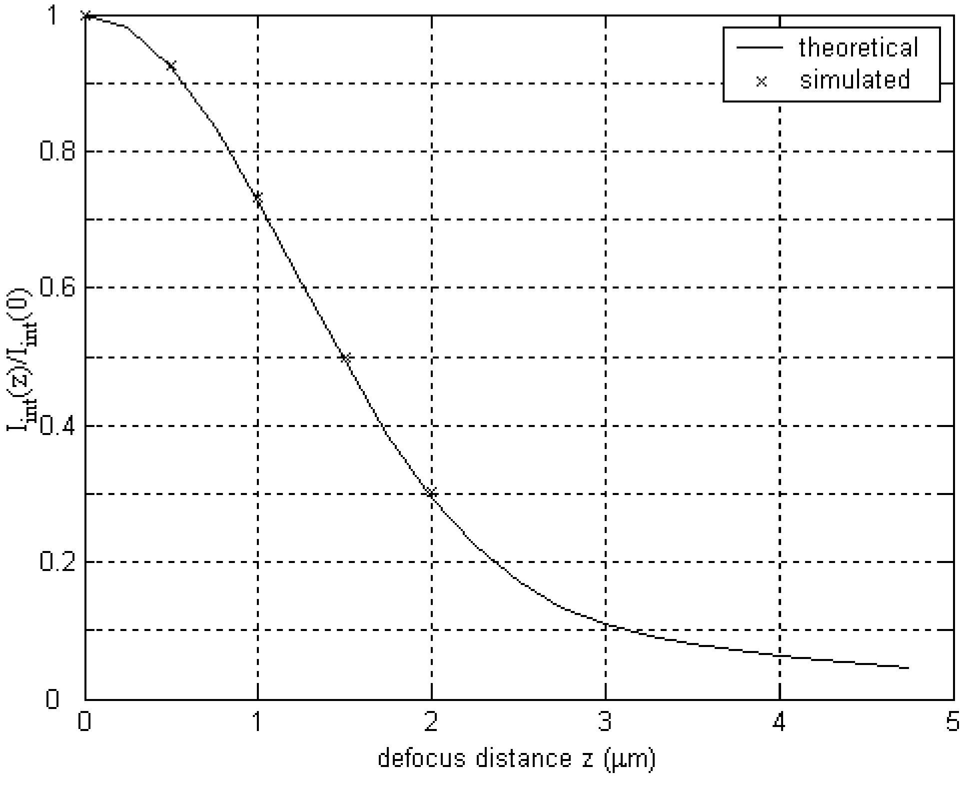

Fig. 3.7. Depth discrimination property for the scanning system.

3.5.3 Point object

The test specimen $O(x', y')$ consisting of a set of nine isolated points being 30 pixels (≈2μm) apart from each other is shown in Fig. 3.8. The simulation results using this object are shown in Fig. 3.9. Unlike the situation for a uniform object, the type 1 microscope can resolve axially a single or multi-point object, because it has a finite longitudinal frequency pass-band for higher transaxial frequency components [56]. The type 2 and non-scanning microscopes exhibit improved axial and lateral resolution, as shown in Fig. 3.9(b). For validation purposes, a comparison of the point spread function at the focal plane for a scanning system between theory and simulation is shown in Fig. 3.10, where the solid line is obtained from Eq. (2.13) and the crosses from the simulated data. To find the FWHM, we set $I(v) = 0.5$. From (2.13) and the parameters in Table 3.1, we work out $v = 1.2599$ or $r \approx 0.20\mu\mathrm{m}$. Since 1μm = 16 pixels, the FWHM in a pixelated image occupies about 6.22 pixels, as indicated by the stars in the figure.

To examine what effects additive Gaussian noise will have on the processed image, we add Gaussian white noise to each individual fluorescence image expressed by Eq. 3.3. This can be done by simply adding a line of the MATLAB function mentioned in Section 3.3 to the simulation programme. We set the mean m=0.4, the variance v=0.0001 for the image intensity $0 \le \mathrm{I} \le 1$ (equivalent to a mean equal to 40% of the maximum signal level and a standard deviation of 2.5% of the mean) to emulate the performance of a CCD detector. We did not add Gaussian white noise to each speckle pattern whose signal-to-noise ratio is good enough so that the influence of Gaussian noise on the reference speckle pattern can be ignored.

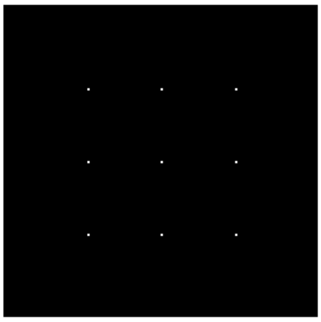

Fig. 3.8. The test object

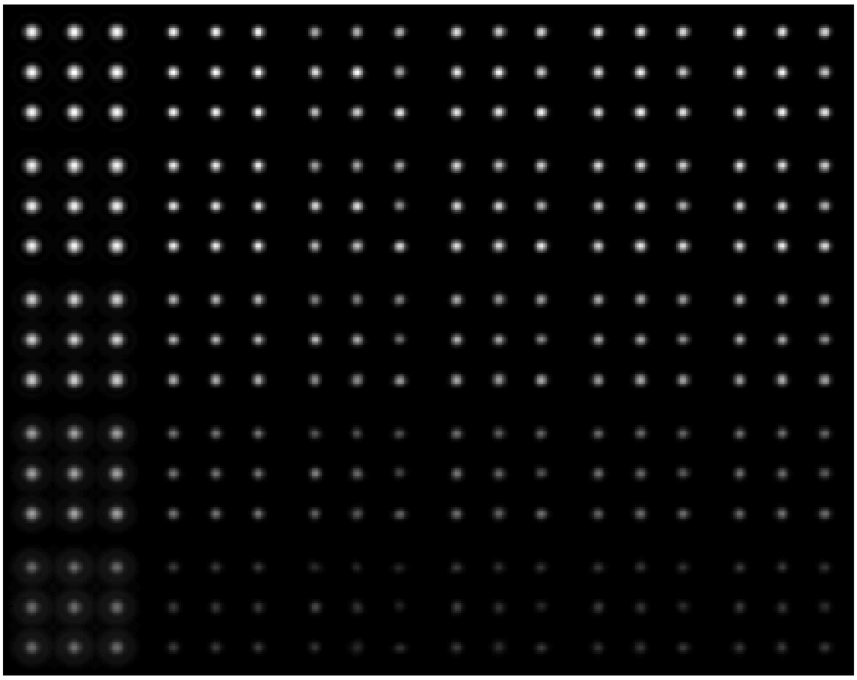

(a) For comparison purposes, the first column shows sets of images of the object at a number of focal positions generated using the calculated response from a conventional microscope. The second column shows the images using the calculated response from a fluorescence scanning confocal microscope. The third to sixth columns show a series of simulated images of the same object calculated using the formula 2.18, but averaged over 500, 1000, 1500 and 2000 independent frames. The images are shown for the in-focus case (top row) and for the object defocused by 0.5, 1, 1.5 and 2 μm respectively (rows two to five).

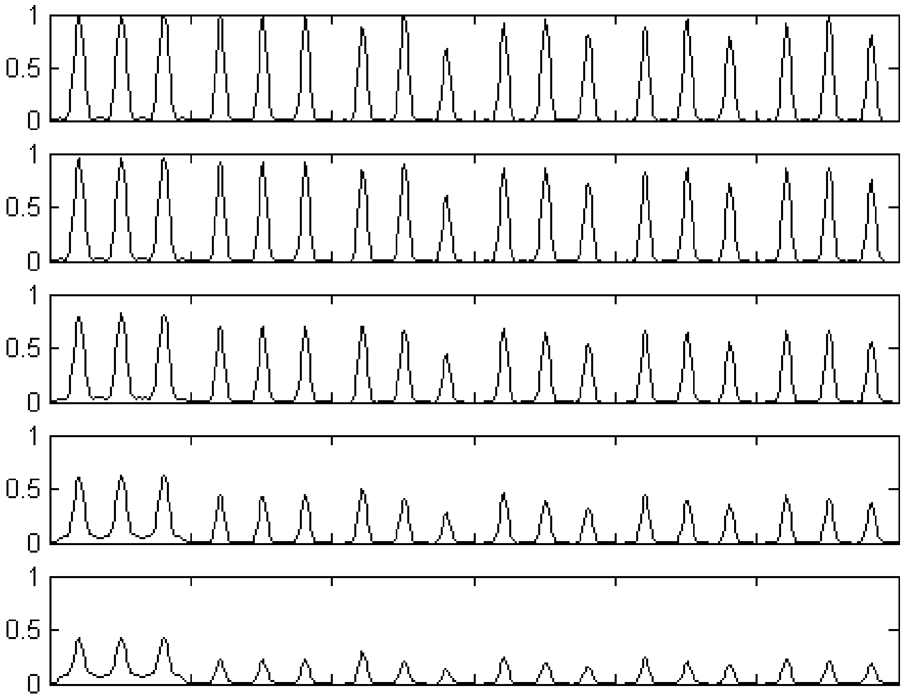

(b) The same data as in (a), but shown as a slice along the central line of each row
Fig. 3.9. Simulated results. Image of a multipoint object

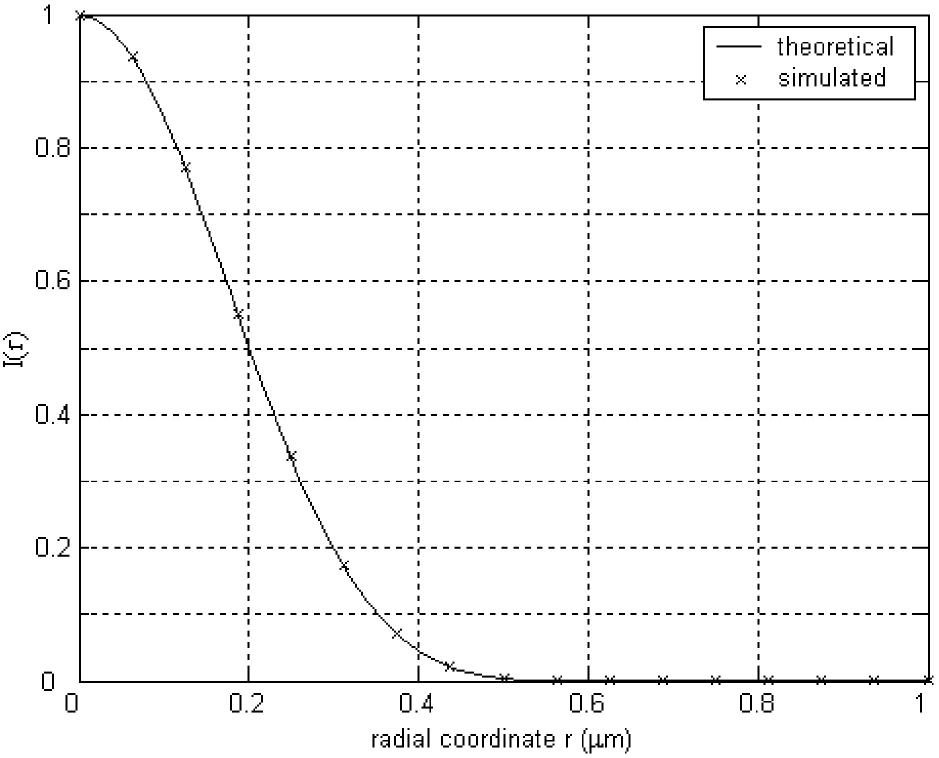

Fig. 3.10. The intensity distribution in the focal plane for a point source in the scanning system

Fig. 3.11 shows the simulation result with shot noise, additive nonzero-mean white noise and quantisation being considered for both the reference and imaging detectors. There is no broadening of PSFs observed compared with the scanning system (free of noise). The FWHM of PSFs for the non-scanning system will be discussed in Chapter 4. Surprisingly, a very low level of residual noise can be observed in the processed image though the noise level is much higher in each individual frame. This can be accounted for by substituting Eq. 3.19 for the I_{im} in the averaging formula 2.18:

$$\begin{aligned} I_p &= \langle (I+n)S \rangle - \langle I+n \rangle \langle S \rangle \\ &= \langle IS \rangle - \langle I \rangle \langle S \rangle + \langle nS \rangle - \langle n \rangle \langle S \rangle \end{aligned} \tag{3.25}$$

Since the noise is random and is uncorrelated to the speckle pattern, the ensemble average of their product is equal to the multiplication of their ensemble averages:

$$\langle nS \rangle = \langle n \rangle \langle S \rangle \tag{3.26}$$

Eq. 3.25 is then reduced to

$$I_p = \langle IS \rangle - \langle I \rangle \langle S \rangle \tag{3.27}$$

which is a type 2 image with most of the noise removed.

A quantitative analysis of the signal-to-noise ratio for each non-scanning bead image with added Gaussian noise was conducted, following the procedure developed by Murray [57]. For measurements of signal, the noise free image in Fig. 3.9 was used. First, a threshold was determined to create a "bead mask" and signal was measured from the mean intensity of pixels within the mask. Another complementary "background mask" was chosen to give an estimate of the background of the noise added image. The noise free image was then subtracted from the noise added image, after background correction, to give a "noise image" (whose mean should be close to zero). The noise image was then squared, and the square root of the mean value (the mean was calculated over only the pixels passed by the bead mask) of the squared noise image was denoted the “root mean square (rms) noise”. Dividing the signal from each image by its rms noise gives the signal-to-noise ratio. The calculated signal-to-noise ratio of a non-scanning system (with the threshold value equal to 0.005) is plotted in Fig. 3.12. It is easy to show that the SNR of the processed image is ten times that of an individual image.

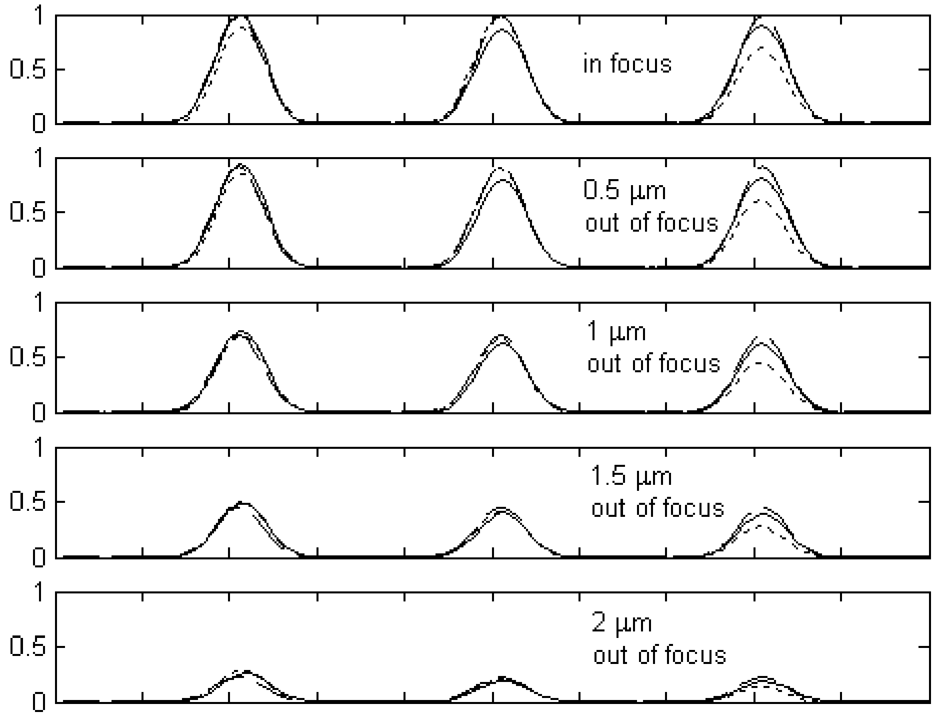

Fig. 3.11. Intensity distribution of PSFs. Dashed line: scanning confocal. Solid line: non-scanning with shot noise and 8-bit quantisation (500 averages). Dotted line: non-scanning with additive white noise (500 averages)

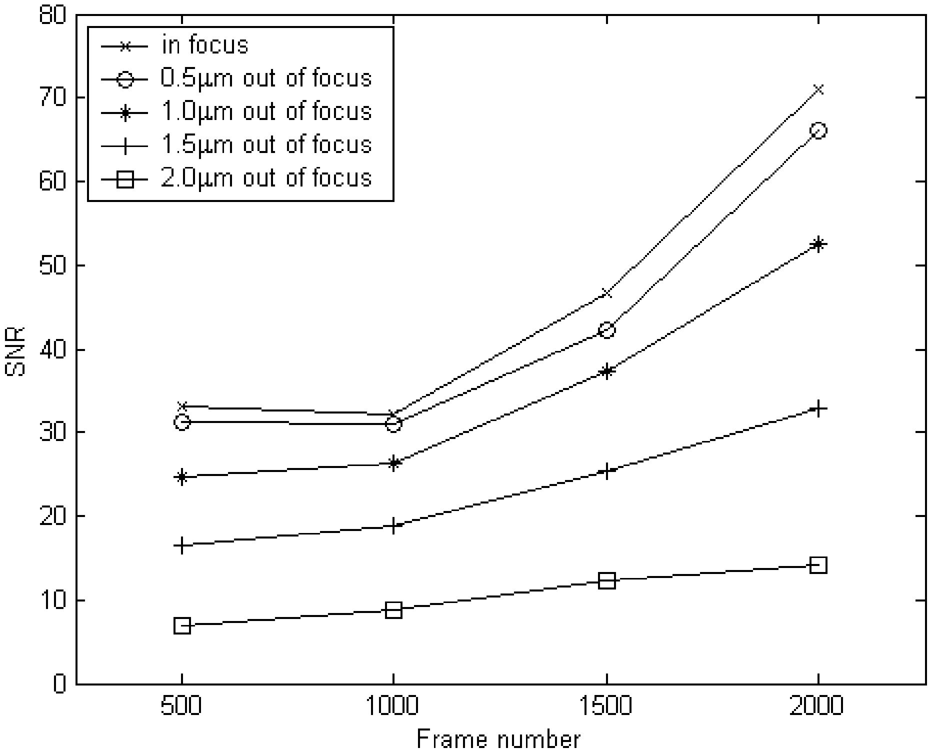

Fig. 3.12. The image signal-to-noise ratio of a non-scanning system

4. Performance evaluation

We have seen in Chapter 3 that the postprocessed image in the non-scanning microscope is imperfect due to a finite number of frames used. In this chapter a number of quantitative evaluation criteria for the imaging performance are given including the depth discrimination property, lateral resolution and, in particular, intensity non-uniformity and non-linearity, and performance evaluation in terms of these criteria are conducted.

4.1 Intensity non-uniformity

It has been shown in Fig 3.6 that unwanted intensity variations in the images from the non-scanning confocal arrangement are evident and it is worth noting that this non-uniformity decreases slowly as the number of frames increases. A suitable evaluation criterion for this intensity non-uniformity may be expressed, for a uniform object, in terms of the ratio of the standard deviation of the image intensity to its mean:

$$\sigma = \frac{\sqrt{< I^2 > - < I >^2}}{< I >} \tag{4.1}$$

where I denotes the intensity in the image. For a scanning confocal microscope, σ should approach zero. A plot of σ averaged over four images of a uniform planar specimen obtained by simulation with four different initial random seeds is shown in Fig 4.1. The error bars indicate the maximum deviation of σ from the average value. It may be noted that σ decreases approximately with the square root of the number of frames.

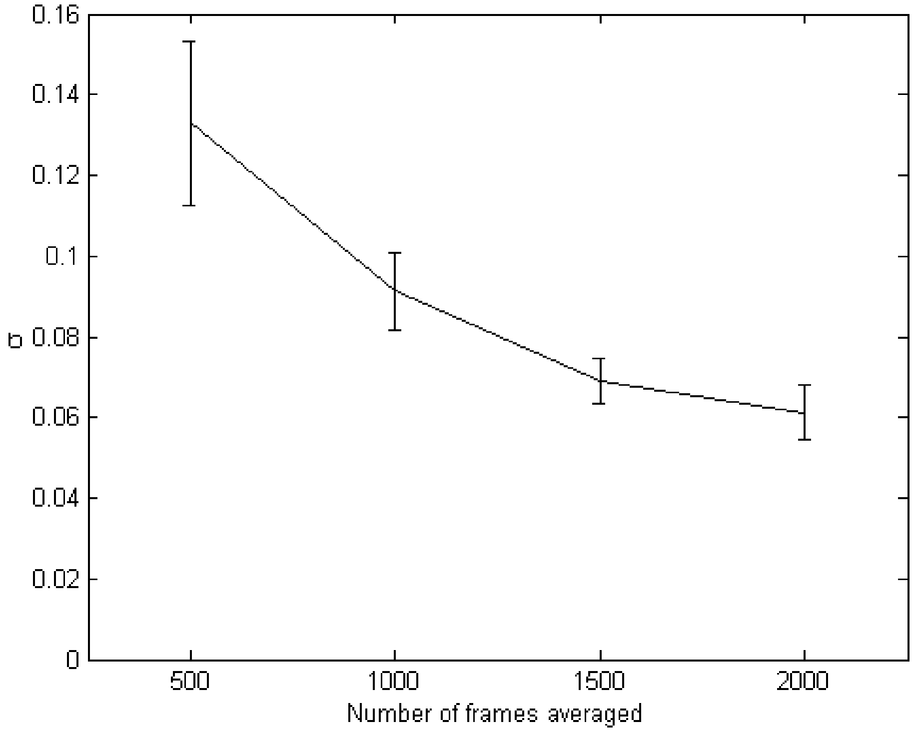

Fig 4.1. A plot of intensity non-uniformity σ averaged over four random images against the number of frames averaged. The error bars indicate the maximum deviation from the average value

4.2 Nonlinear variation of image intensity

A further criterion to judge the output of a microscope arrangement is whether the final image intensity varies linearly with the strength of the fluorescence. To investigate this, a test object consisting of nine isolated points with fluorescence radiation level varying from 1 to 9 is used. Two sample simulated images are shown in Fig 4.2. Non-linearity is tested by comparing the energy contained in each peak against the fluorescent radiation level in the corresponding point source. Fig 4.3 shows the energy in the peaks of Fig. 4.2, together with the corresponding results for a scanning confocal system. A measure of non-linearity called average deviation from linearity (ADL) can be used. The ADL is defined as

$$ADL = \frac{\sqrt{\sum_{i=1}^{N}(y'_i - y_i)^2 / N}}{\sum_{i=1}^{N} y_i / N} \times 100\% \tag{4.2}$$

where y_i are the ordinates for the scanning confocal microscope in Fig. 4.3, y'_i are the ordinates for non-scanning, and $N = 9$ is the number of peaks. A plot of the ADL calculated from four random images with (4.2) against the number of frames is shown in Fig. 4.4. It is interesting to see that ADL decreases, in the same fashion as the intensity non-uniformity σ, with the square root of the number of frames, as the intensity nonlinearity in essence arises from the intensity non-uniformity. The minimum number of frames is 1000 if a 10% intensity nonlinearity can be tolerated.

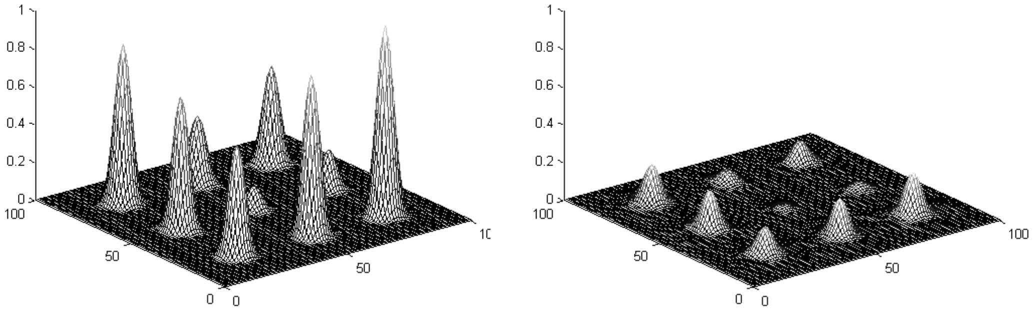

(a) in focus (b) 2 μm out of focus

Fig 4.2. Image of a test object consisting of 9 isolated points with fluorescence radiation level varying from 1 to 9 in a non-scanning confocal microscope.

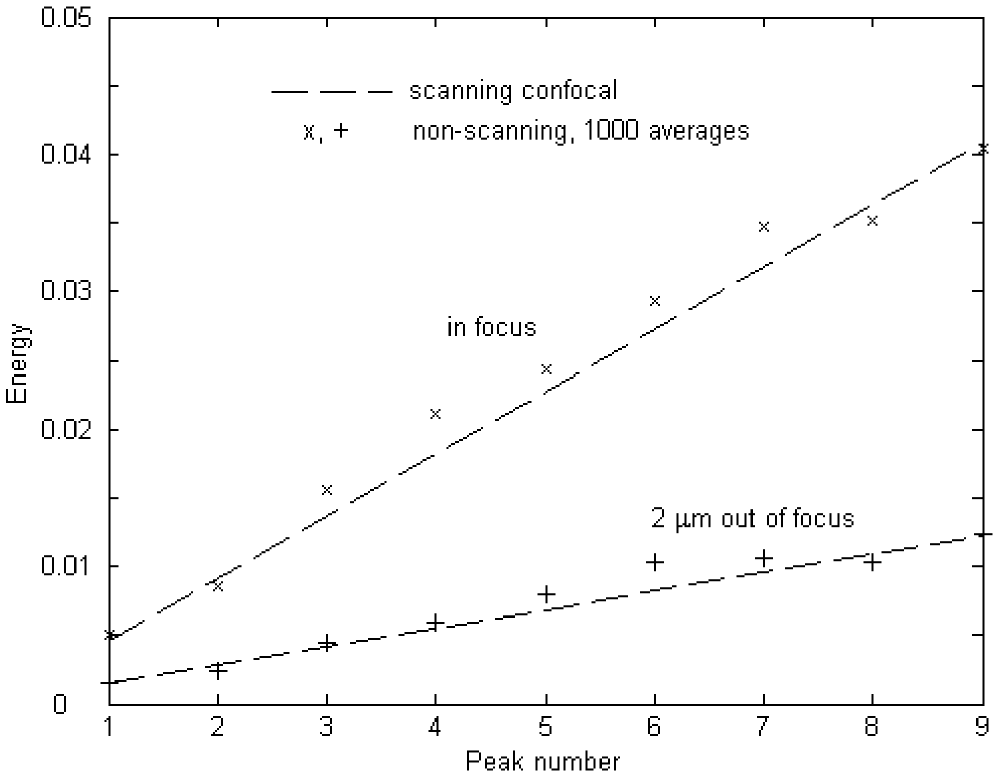

Fig 4.3. Plot of the energy in the peaks of Fig. 4.2, together with the corresponding results for a scanning confocal system.

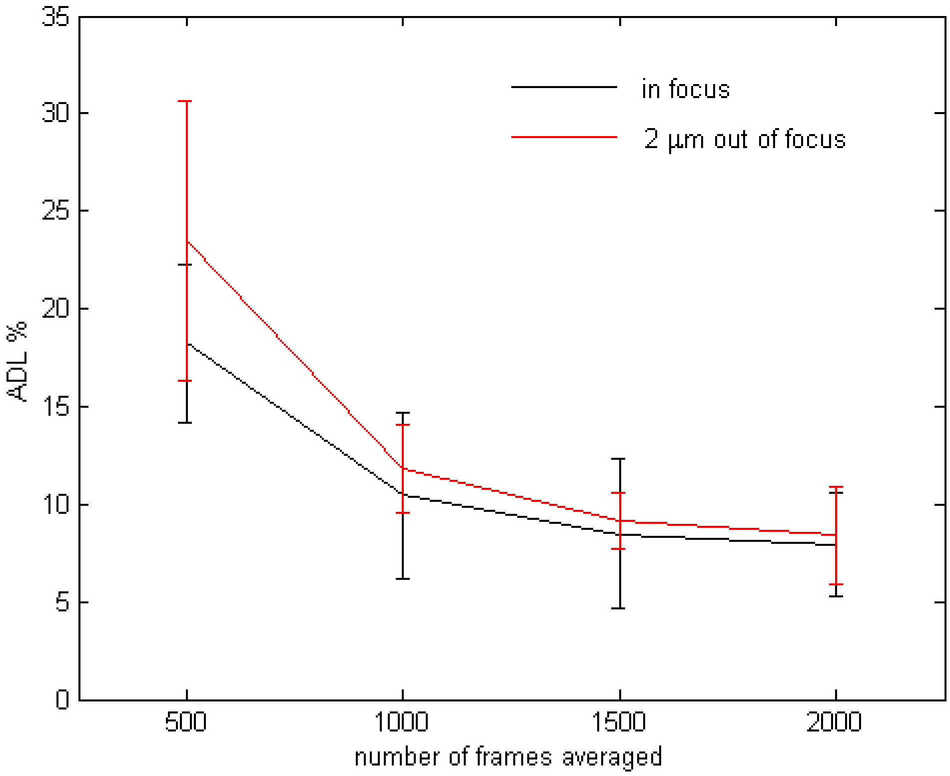

Fig. 4.4. A plot of image intensity nonlinearity averaged over four random images. The error bars indicate the maximum deviation from the average value

4.3 Depth discrimination property

The depth discrimination property for the non-scanning arrangement can be evaluated in the way discussed in Chapter 2.2, although the image intensity is not uniform. The integrals in (2.12) may be replaced with the mean of intensity:

$$< I(z) > / < I(0) > \qquad (4.3)$$

Fig 4.5 shows the depth discrimination property calculated with (4.3) using the data from the images of Fig 3.6. It may be seen that the scanning and non-scanning confocal microscopes have indistinguishable responses to defocus, and the shape of curve does not depend on the number of averaging.

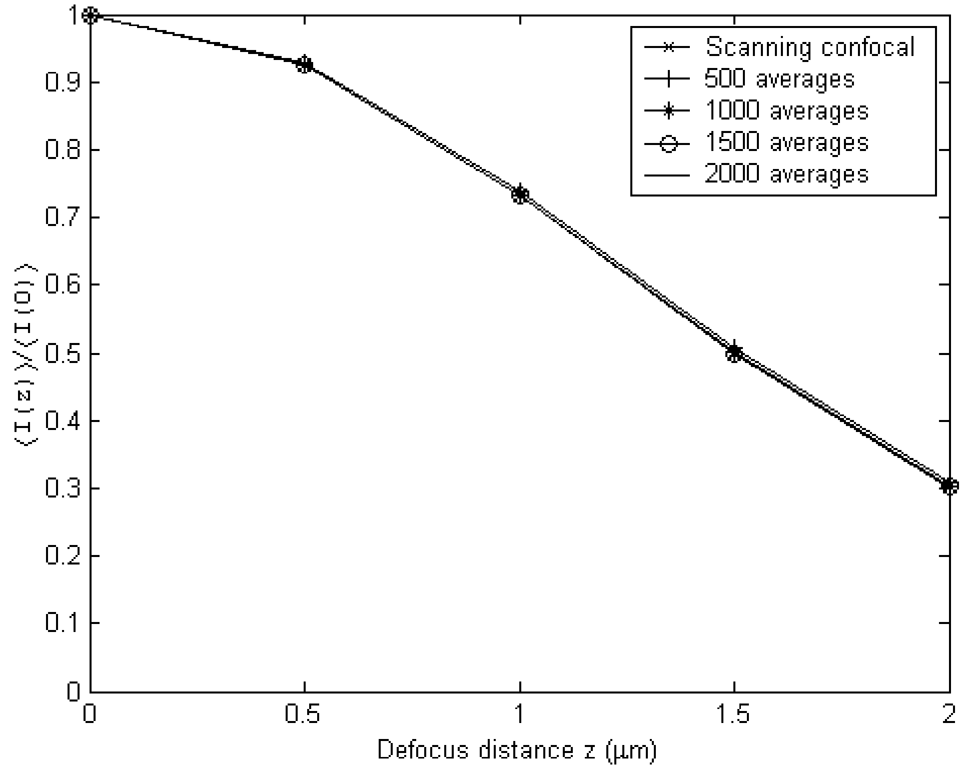

Fig 4.5. Comparison of depth discrimination property between scanning and non-scanning fluorescence confocal microscopes

4.4 Lateral resolution

Lateral resolution may be assessed by measuring the FWHM of the PSF. A simulated image of 9 isolated point sources with equal fluorescence emission in a non-scanning microscope is shown in Fig 4.6 where the peaks are slightly different from each other in height due to the non-uniformity phenomenon. To calculate the FWHM of each peak in this pixelated image, the analytical expression of the one-dimensional intensity distribution for the PSFs has been found by means of *cubic spline interpolation*. The average FWHM is given by

$$\bar{\delta} = \frac{1}{n}\sum_{i=1}^{n}\delta_i \tag{4.4}$$

where n is the number of peaks, δ_i is the FWHM of the ith peak. A measure of the dispersion of the values (standard deviation) is given by

$$\sigma = \sqrt{\frac{1}{n-1}\sum_{i=1}^{n}(\delta_i - \bar{\delta})^2} \tag{4.5}$$

The calculation results for the non-scanning microscope are presented in Fig 4.7. which are very similar to those for the scanning microscope.

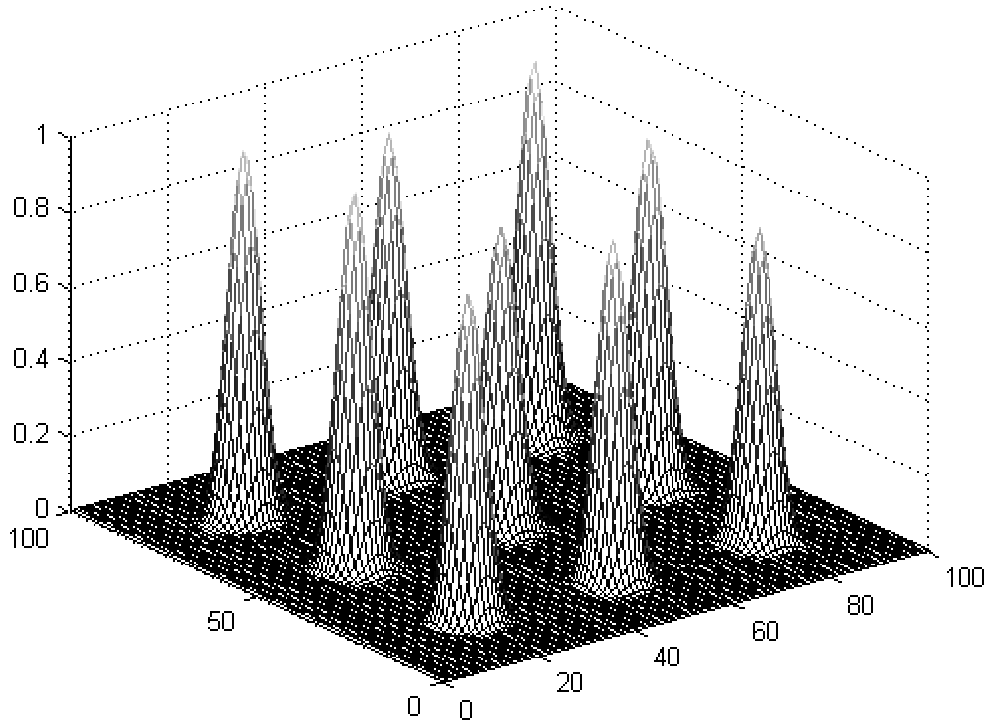

Fig 4.6. Simulated image of 9 isolated point sources in a non-scanning confocal microscope

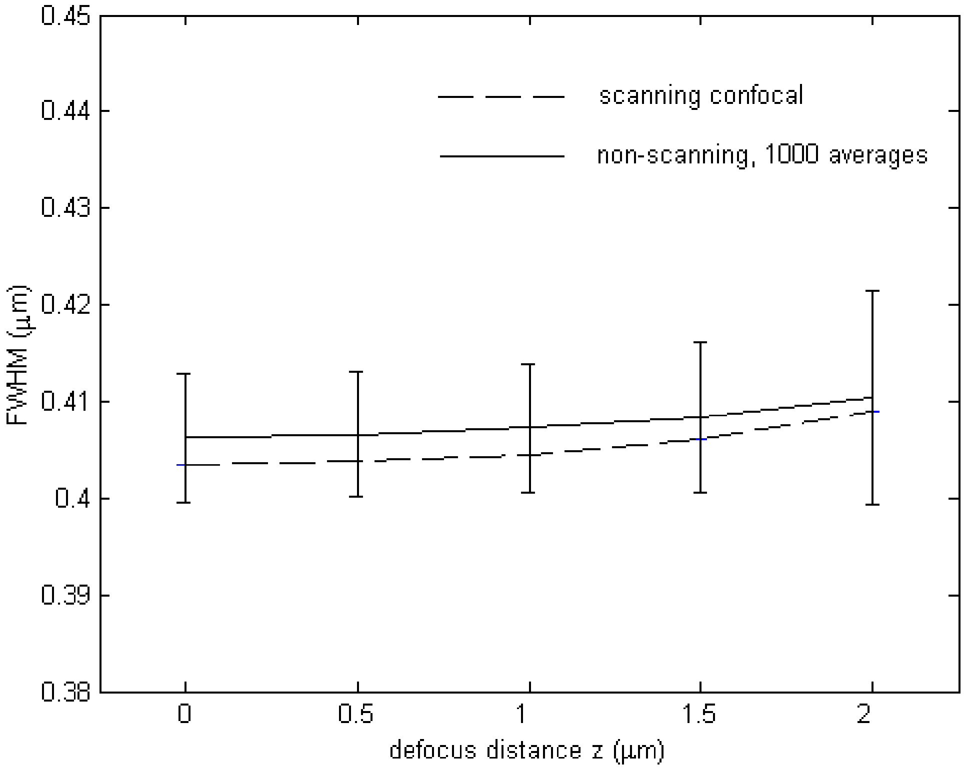

Fig 4.7. Average FWHM of the nine peaks in the simulated image of a scanning and non-scanning confocal microscope. The error bars indicate the standard deviation.

5. Speckle processing

From Fig. 3.9 it may be seen that at least 500 raw images are required for a postprocessed image of acceptable quality. The frame rate of a typical cooled digital CCD camera is 25-30 frames/sec for a 512×512 image, so it will take about 15-20 seconds for the camera to capture 500 frames sequentially. This is too slow compared with the scanning systems.

As discussed in Chapter 3, the intensity distribution in a laser speckle pattern has a high probability of low intensities and a lower probability of higher intensities. This wide variation in intensity levels has the effect of lowering the efficiency of the averaging process in equation (2.18) and accounts for the large number of frames required to get a reasonable value for image uniformity illustrated in Fig. 4.1. For the application of speckle modulation, the important information is contained in the placement and size of the speckles and not in the intensity fluctuation between them. Therefore, a possible way to improve the efficiency of the averaging process is to alter the intensity distribution in the reference speckle pattern by using some sort of transfer functions, such as sigmoid function, hyperbolic tangent function and so on. After the transformation, the mean relative to the maximum of the output data is increased compared with the input data but the important information about the speckle placement and size is preserved, so that the efficiency of the averaging process can be improved and the number of frames required can be reduced.

In this chapter two methods are described which effectively reduce the number of frames via speckle processing. They can be readily applied to the raw speckle pattern recorded from the reference detector $I_{ref}(x, y, 0)$ but can hardly be applied to the illumination speckle pattern $S(x', y', z')$ which is a three-dimensional distribution in space. New simulation results show that they do not adversely affect the performance in terms of the evaluation criteria considered in Chapter 4.

5.1 A-Law compression

A method known as *A-Law compression* [58] is commonly used in telephone systems. The input signal I is divided into three regions and the output signal is given by

$$I_m = \begin{cases} \dfrac{AI}{1+\ln A} & \text{for } 0 \le I \le \dfrac{V}{A} \quad (\textit{linear}) \\ \dfrac{V(1+\ln(AI/V))}{1+\ln A} & \text{for } \dfrac{V}{A} \le I \le V \quad (\textit{logarithmic}) \\ V & \text{for } I > V \quad (\textit{limited}) \end{cases} \tag{5.1}$$

where V is the maximum value of the signal, and A is the *compression coefficient*. The characteristic is shown in Fig. 5.1. For large values of A the characteristic is predominantly logarithmic. When $A = 1$, the logarithmic region vanishes.

For the limited region, the intensities above the range [0, V] will be mapped to the maximum value V, which is known as *thresholding*. The simulation of thresholding can be easily performed in MATLAB by using function uint8(I/V*255) or uint16(I/V*65535), where the values of input matrix I higher than V will be brought back to 255 or 65535.

A MATLAB function compound (I, A, V, ‘A/compressor’) can be used to implement logarithmic compression for the input signal I when the thresholding operation is complete. The scalar A is the A-Law parameter, and V is the threshold value. Example processed laser speckle images using A-Law compression are shown in Fig. 5.2, where the threshold value V is set to ten times the mean of speckle intensity $\overline{S}$.

Sigmoid function and hyperbolic tangent function are frequently used in artificial neural networks. They can be expressed as $S(x)=1/(1+e^{-ax})-0.5$ and $\tanh(ax)$ respectively, where a is the weights. The speckle patterns processed with these two functions are shown in Fig. 5.2(c) and (d) respectively. It seems that sigmoid and tanh are also worthwhile methods for speckle processing, but with only one parameter that can be selected. The A-Law method is more general and provides more options for data compression. In fact, as we shall see later, the form of compression within the nonlinear region is not very critical to the level of performance in terms of the intensity non-uniformity, light efficiency and so on. The thresholding-only method and binary speckle which do not contain nonlinear regions give comparable or even better overall performance than the nonlinear compression methods.

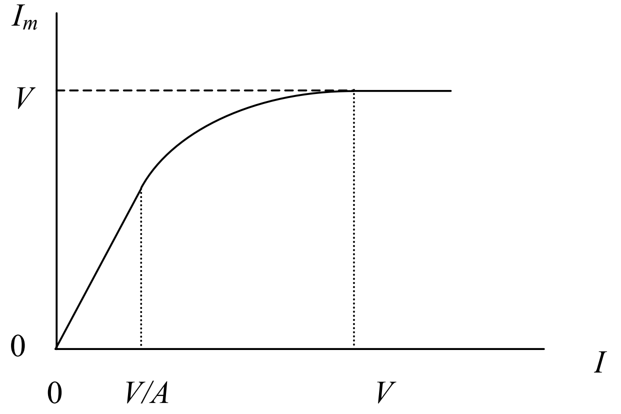

Fig. 5.1. The A-Law compression characteristic

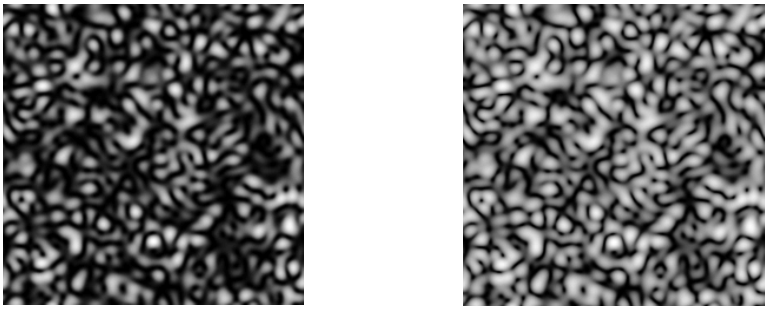

(a) A=10, $V = 10\bar{S}$ (b) A=40, $V = 10\bar{S}$

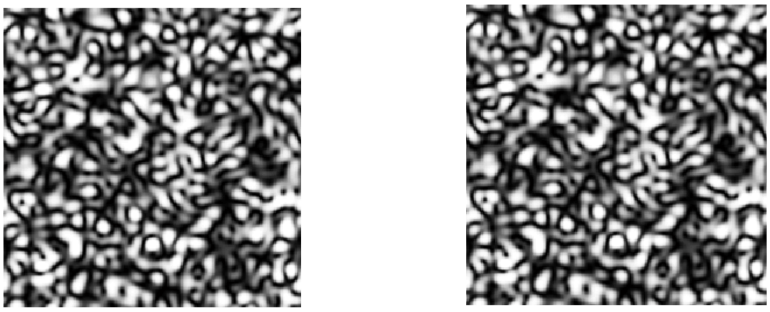

(c) $a = 0.0002$ (d) $a = 0.0001$

Fig. 5.2 Laser speckle patterns processed with (a) and (b): A-Law, (c): sigmoid, (d): hyperbolic tangent

Applying A-Law processing to each individual reference speckle pattern $I_{ref}(x, y, 0)$ before the averaging process (2.18), new simulation results are obtained and these are shown in Fig. 5.3. Compared with Fig. 3.6, it may be seen that the image uniformity for a given number of frames is significantly improved. Or, conversely, for a given image quality the number of frames can be reduced by about 50% when $A = 10$ and $V = 10\bar{S}$, as shown in Fig. 5.4. Fig. 5.5 shows a comparison of the depth discrimination performance of the non-scanning arrangement using A-Law processing and the conventional scanning system. Fig. 5.6 shows a comparison of the average resolution measure FWHM obtained in conventional scanning and with the A-Law processed non-scanning system. Compared with Fig. 4.7, it may be seen that the non-scanning system with A-Law processing improves the lateral resolution at small defocus. The improvement is not significant at large defocus because the reference speckle patterns are no longer correlated with the fluorescence frames generated at large defocus and the A-Law method becomes less effective. Fig. 5.7 shows a comparison of the linearity of the A-Law and scanning arrangements. No significant deterioration of performance is observed using the A-Law processing.

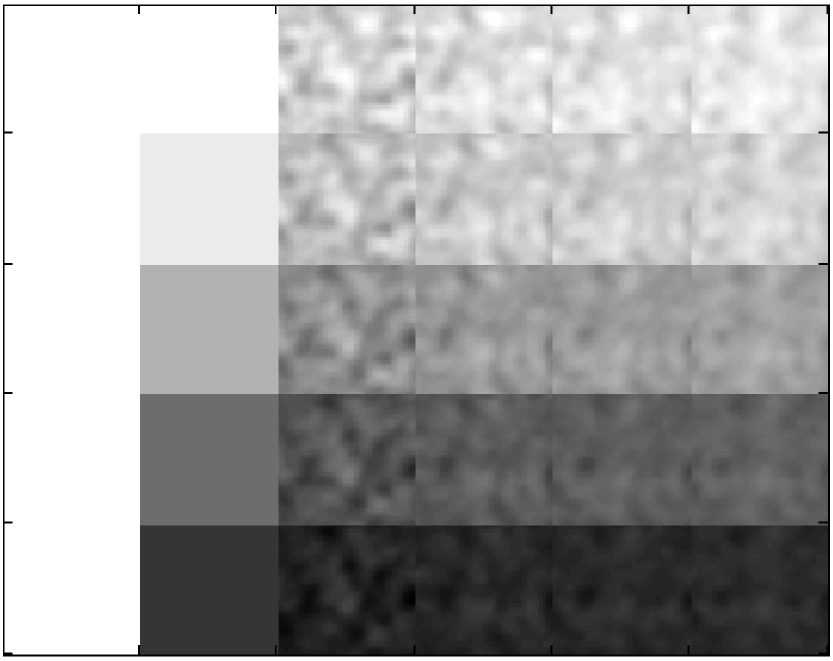

(a) Grayscale images

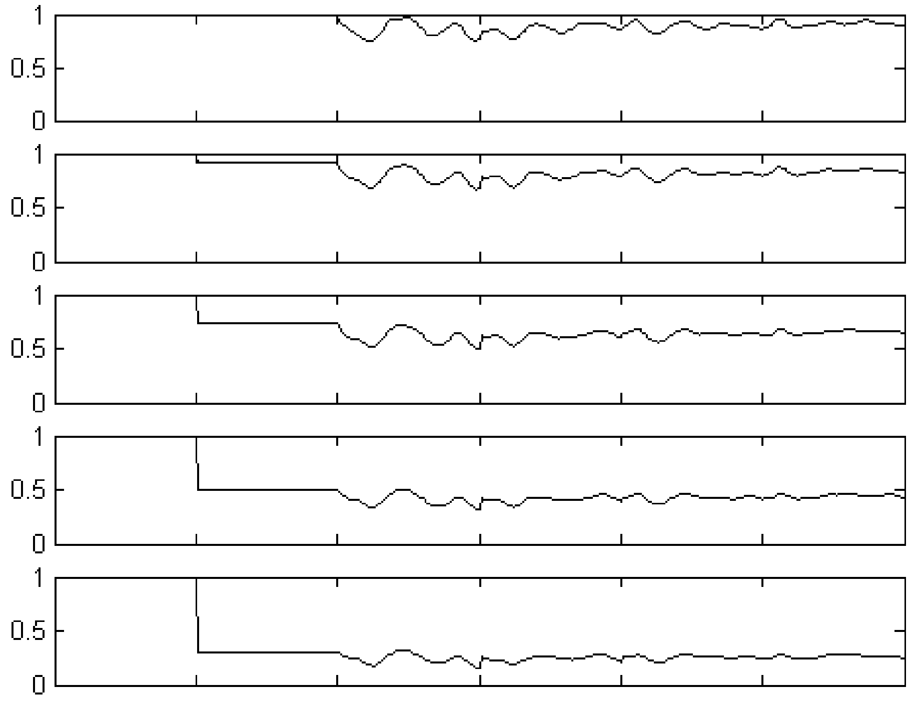

(b) The same data as in (a) but shown as a slice along the central line of each row
Fig. 5.3. Simulated images of a uniform fluorescent object with A-Law processing applied to the reference speckle patterns (A=10, $V = 10\bar{S}$)

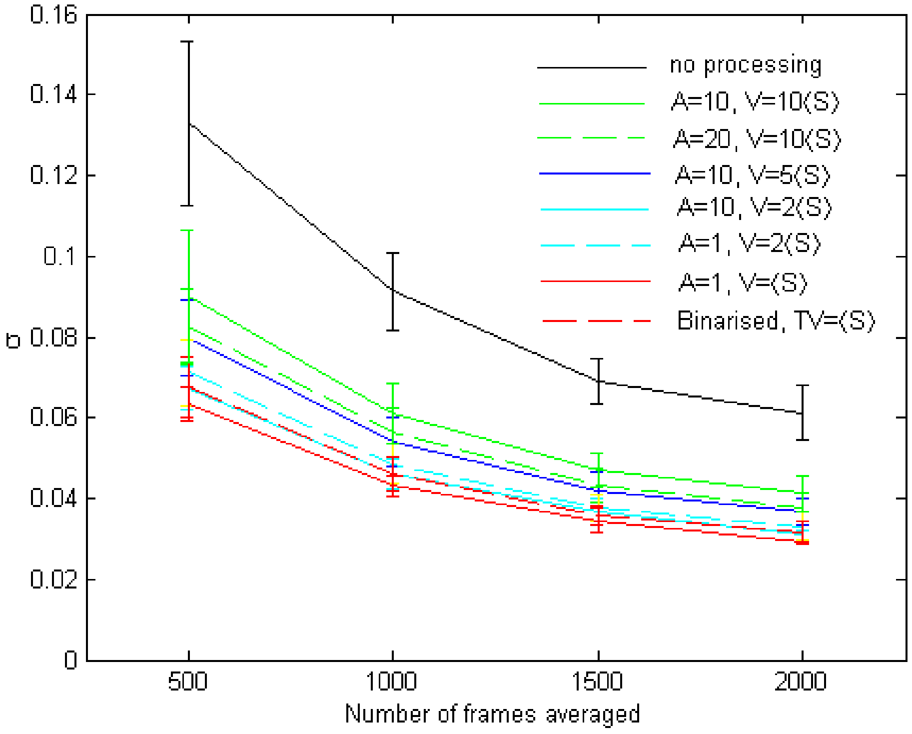

Fig. 5.4. A plot of intensity nonuniformity σ against the number of frames averaged

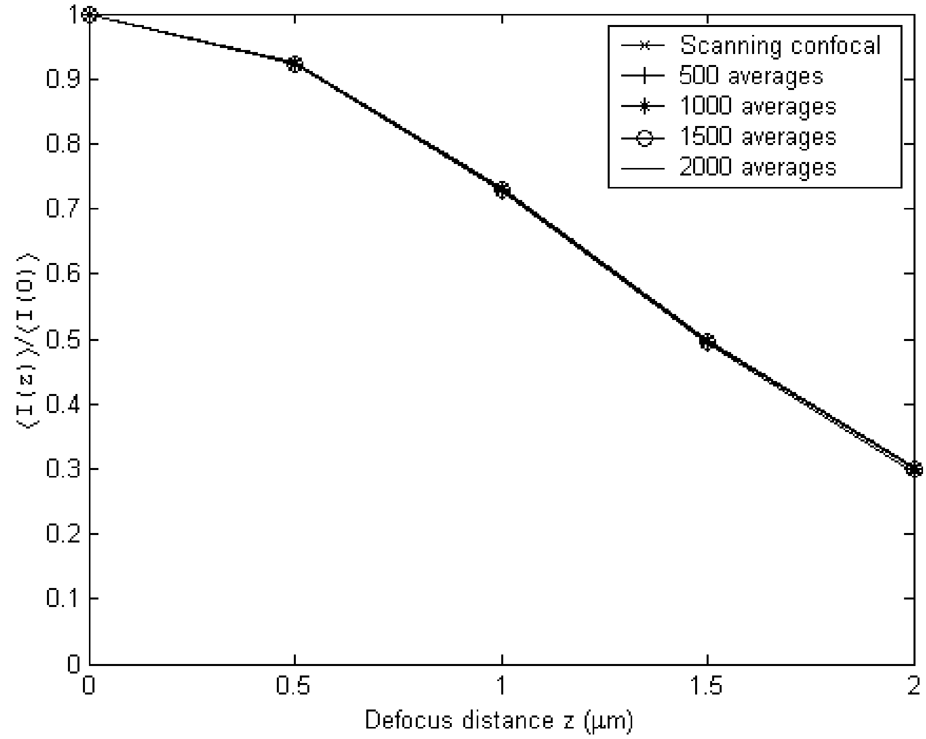

Fig. 5.5. Comparison of depth discrimination property between scanning and non-scanning with A-Law processing ($A = 10$, $V = 10\overline{S}$)

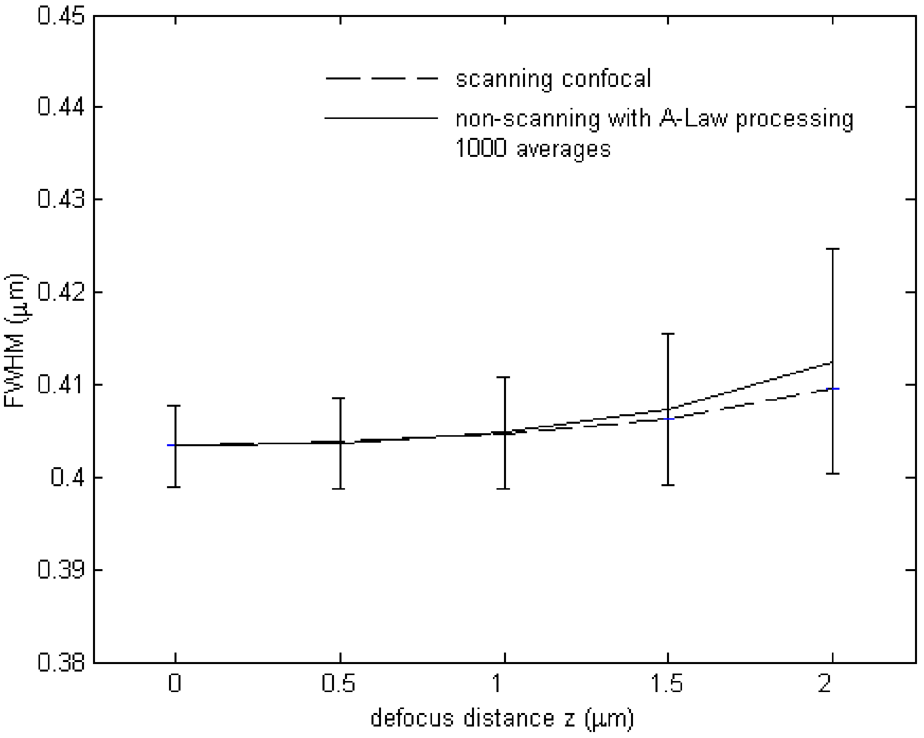

Fig. 5.6. Average FWHM of the nine peaks in the simulated image of a non-scanning confocal microscope with A-Law processing ($A = 10$, $V = 10\overline{S}$). The error bars indicate the standard deviation

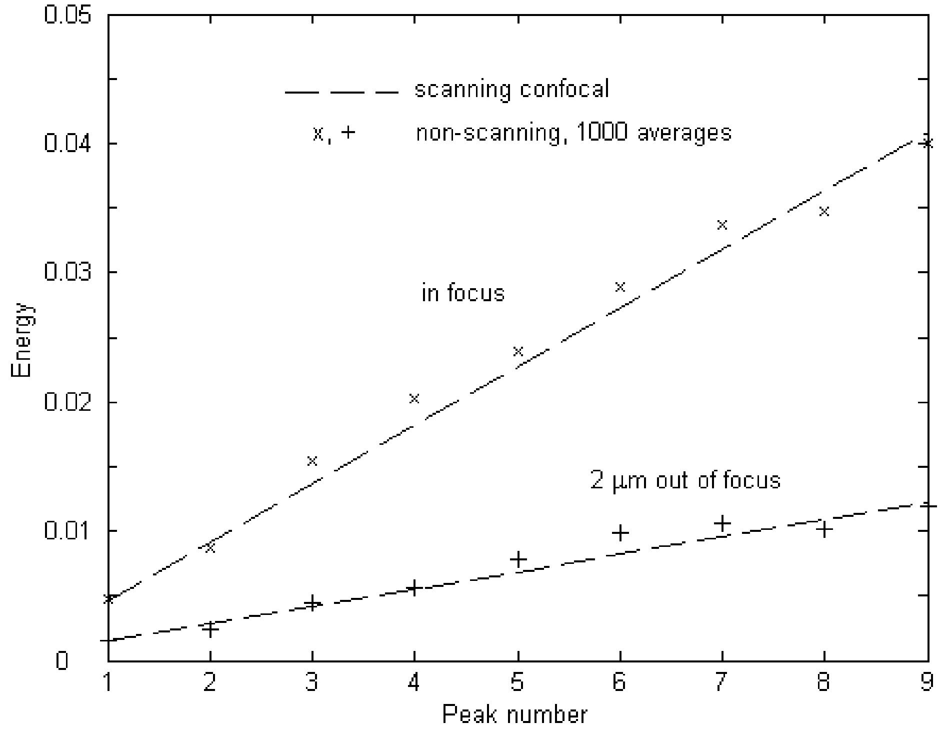

Fig. 5.7. Plot of energy against the peak number for the case of A-Law processing ($A = 10$, $V = 10\overline{S}$)

As mentioned above, the logarithmic region vanishes when A=1, hence only thresholding operation exists. Interest has been drawn to this case because the thresholding operation can be automatically performed if the input speckle intensity exceeds the saturation level of the CCD detector (with antiblooming protection). It may be seen from Fig. 5.4 that the intensity uniformity is greatly improved via thresholding operation. For a given image quality the number of frames can be reduced by about 75% when $A = 1$ and $V = \overline{S}$. Figs. 5.8, 5.9 and 5.10 show the comparison of performance of scanning and non-scanning system with the thresholding applied to the speckle patterns. It is worth noting that the lateral resolution is improved slightly at small defocus distances compared with the A-Law processing case.

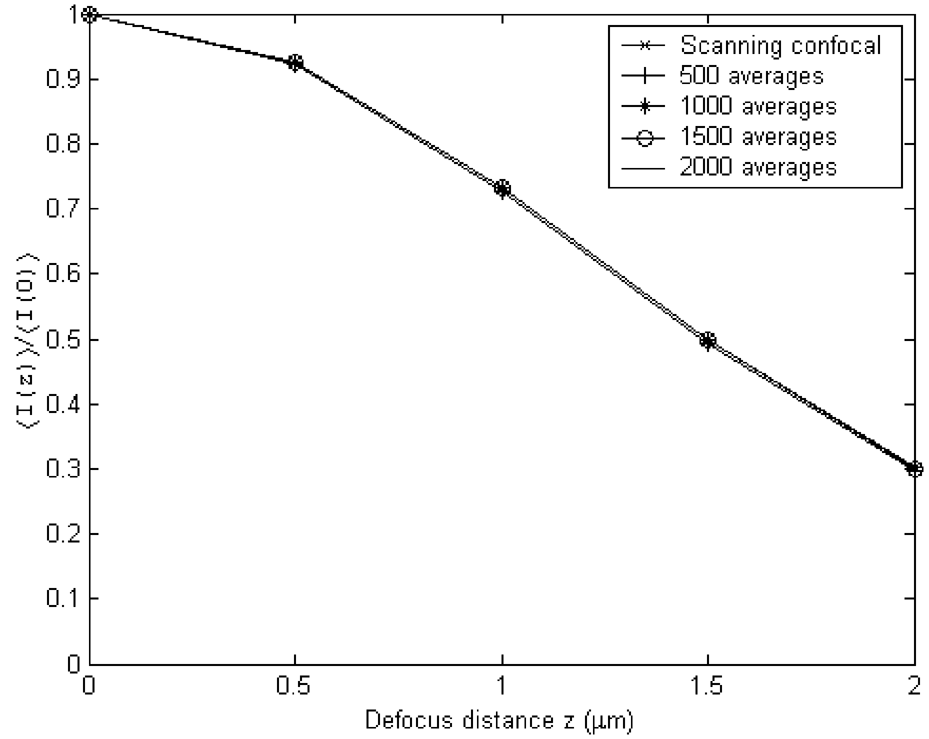

Fig. 5.8. Comparison of depth discrimination property between scanning and non-scanning with thresholding operation ($A=1$, $V=\overline{S}$)

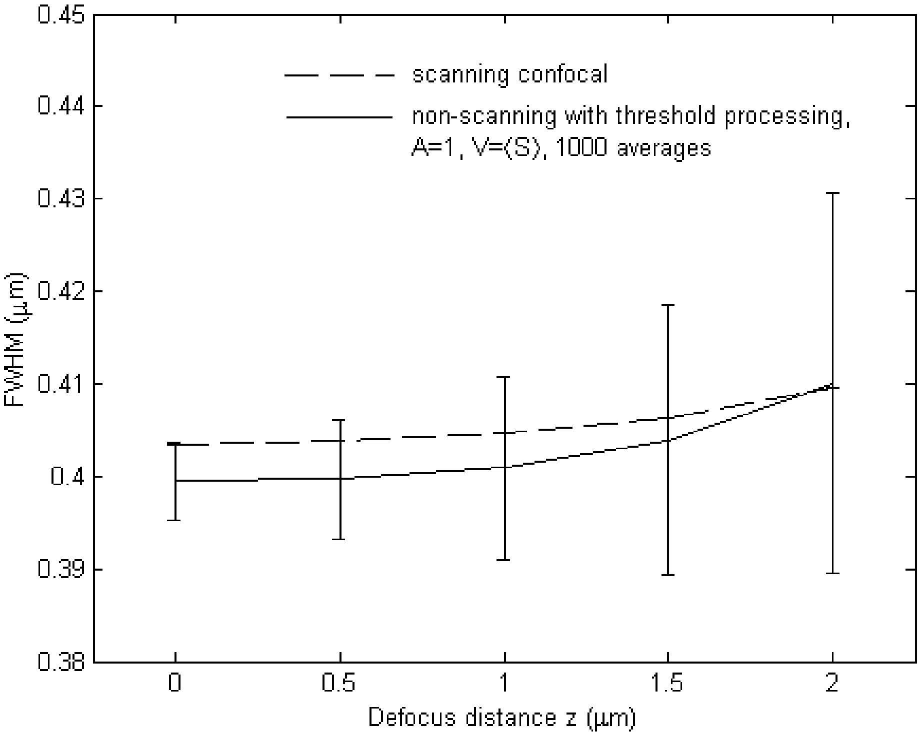

Fig. 5.9. Average FWHM of the nine peaks in the simulated image of a non-scanning confocal microscope with thresholding operation ($A=1$, $V=\overline{S}$). The error bars indicate the standard deviation

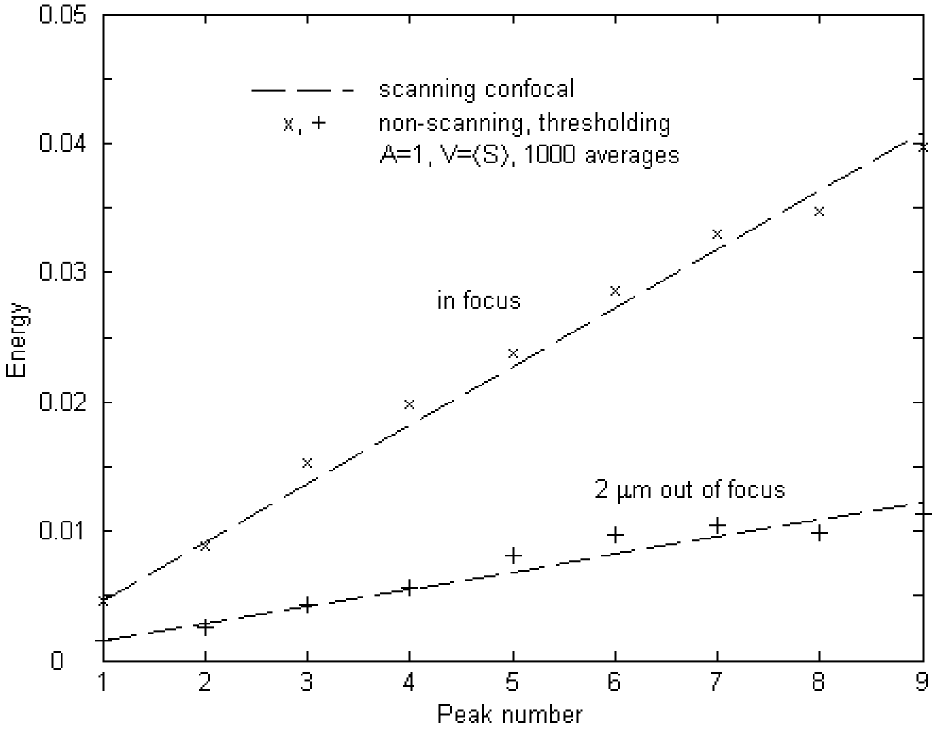

Fig. 5.10. Plot of energy against the peak number for the case of thresholding

5.2 Binary speckle

A continuous laser speckle pattern can be represented by a binary one, shown in Fig. 5.11, in many applications, if a suitable threshold value is determined for a given aperture, because the main features of the *power spectral density* of the speckle intensity are maintained after a binarisation operation is performed [59].

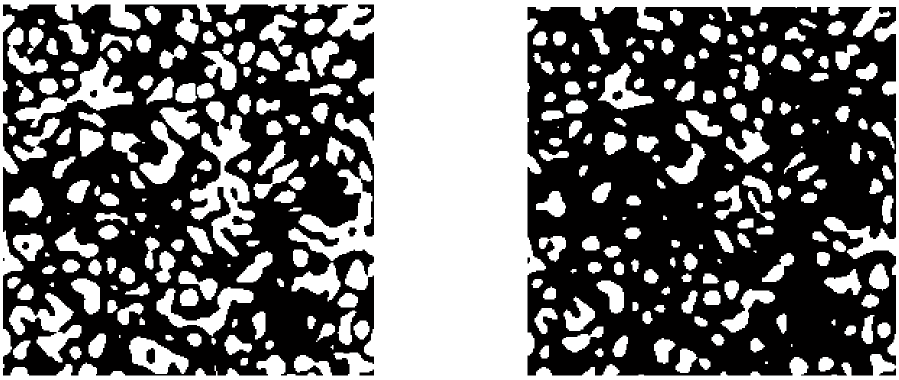
(a) Threshold value $\overline{S}$ (b) Threshold value $1.5\overline{S}$

Fig. 5.11. Binary speckle patterns

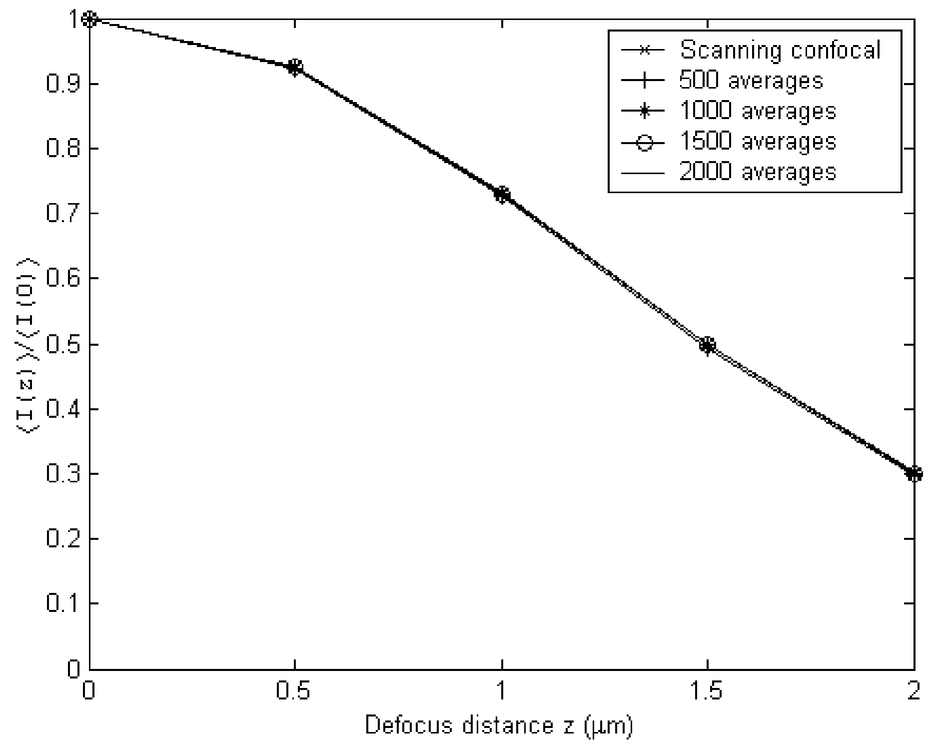

Fig. 5.12. Comparison of depth discrimination property between scanning and non-scanning with binary speckle (threshold value= $\overline{S}$)

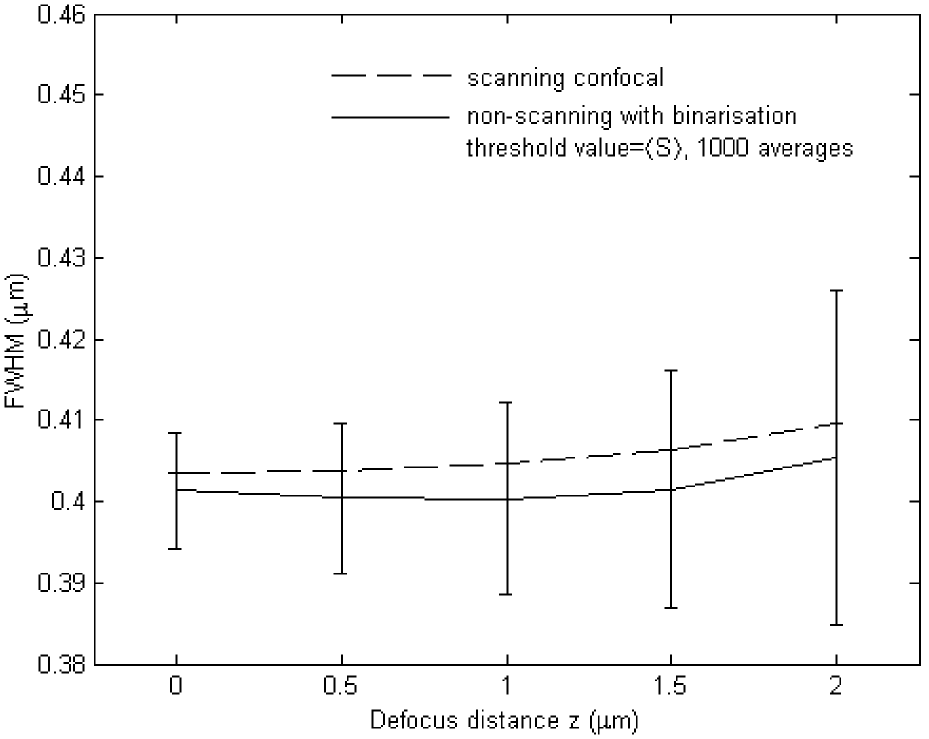

Fig. 5.13. Averaged FWHM of the nine peaks in the simulated image of a non-scanning confocal microscope with binarisation. The error bars indicate the standard deviation

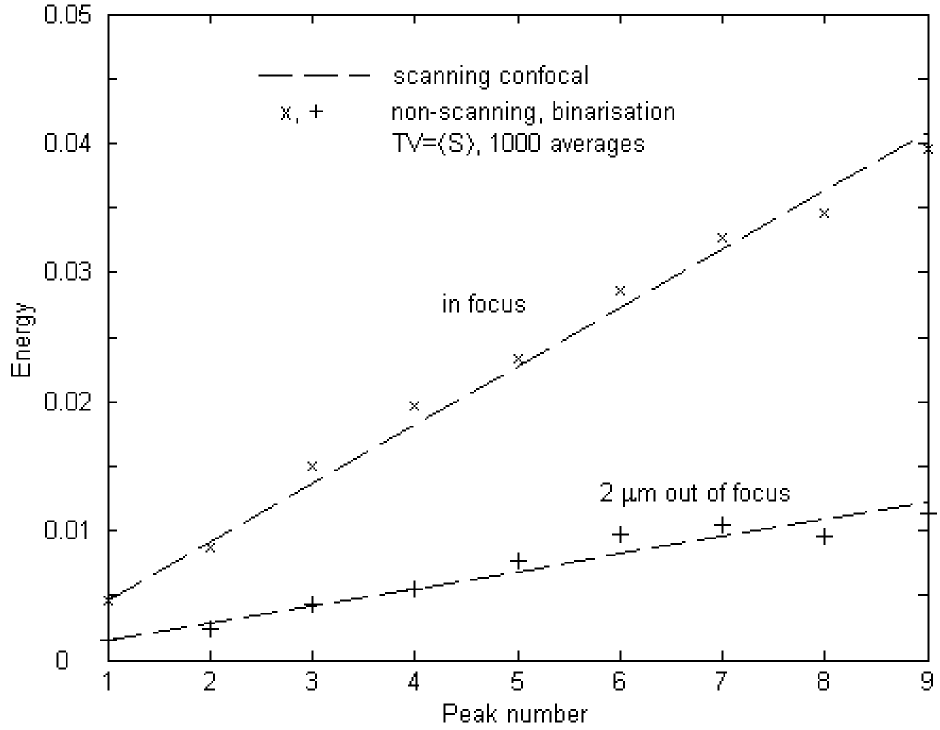

Fig. 5.14. Plot of energy against the peak number for the case of binary speckle (threshold value $=\overline{S}$)

By using binary speckle patterns the intensity non-uniformity can be reduced by about a factor of 2 as shown in Fig. 5.4. Figs 5.12, 5.13 and 5.14 show the comparison of performance of scanning and non-scanning system with binary speckle patterns. No significant change in depth discrimination property and linearity of the system is observed. However the FWHM values are widely distributed at higher defocus distances.

Compared with A-Law compression and thresholding-only, binary speckle not only reduces the number of frames effectively but also reduces the amount of digital storage space. For example, transforming a speckle pattern of 256 grey levels into a pattern of 2 levels results in an 8:1 savings in digital storage space. This is useful for the real-time image processing which will be discussed in Chapter 7, as the speckle patterns recorded from a CCD camera need to be transmitted to a miniature LCD and reproduced on the LCD instantaneously. The use of binary speckle should reduce the response time or may lead to the exploitation of binary optically addressed spatial light modulator [60, 61].

5.3 Analysis

The above simulation of non-scanning confocal imaging with the application of speckle processing shows that both the A-Law and binarisation operations have significant positive influences on the intensity non-uniformity and the intensity non-linearity, some degree of influences on the FWHM of the point spread function, but no effect on the depth discrimination in terms of the performance evaluation criteria considered. Since the simulation is performed based on the parameters chosen by chance, it is therefore necessary to examine how the intensity non-uniformity σ and the FWHM vary jointly with the compression coefficient A and the threshold value V, so that optimum parameters may be determined by the compromise between σ and FWHM. Note that σ also acts as a measure of light efficiency since by definition it is inversely proportional to the mean of image intensity, and the ADL which acts as a measure of the intensity nonlinearity can be represented by σ, since the intensity nonlinearity arises actually from the intensity non-uniformity and both have the same dependence on the number of frames as pointed out in section 4.2.

An analysis for this purpose is conducted and the results for the cases of $A = 1$, $A = 10$, $A = 20$ and binarisation operation are shown in Figs. 5.15 to 5.18 respectively. The FWHMs are calculated for the point object at two focal positions (in focus and 2μm out of focus). It may be seen that optimum parameters can be determined by making a compromise. For the case of A=1, or the thresholding-only operation, the optimum threshold value appears between $< S >$ and $2 < S >$. The choice of compression coefficient A is not very critical to the level of performance. The optimum threshold value for the case of A=10 or A=20 is the same which is $2 < S >$. For the binarisation case, the optimum threshold value should be $< S >$. A summary of the above analysis is given in Table 5.1 where the crosses indicate the corresponding optimal parameters.

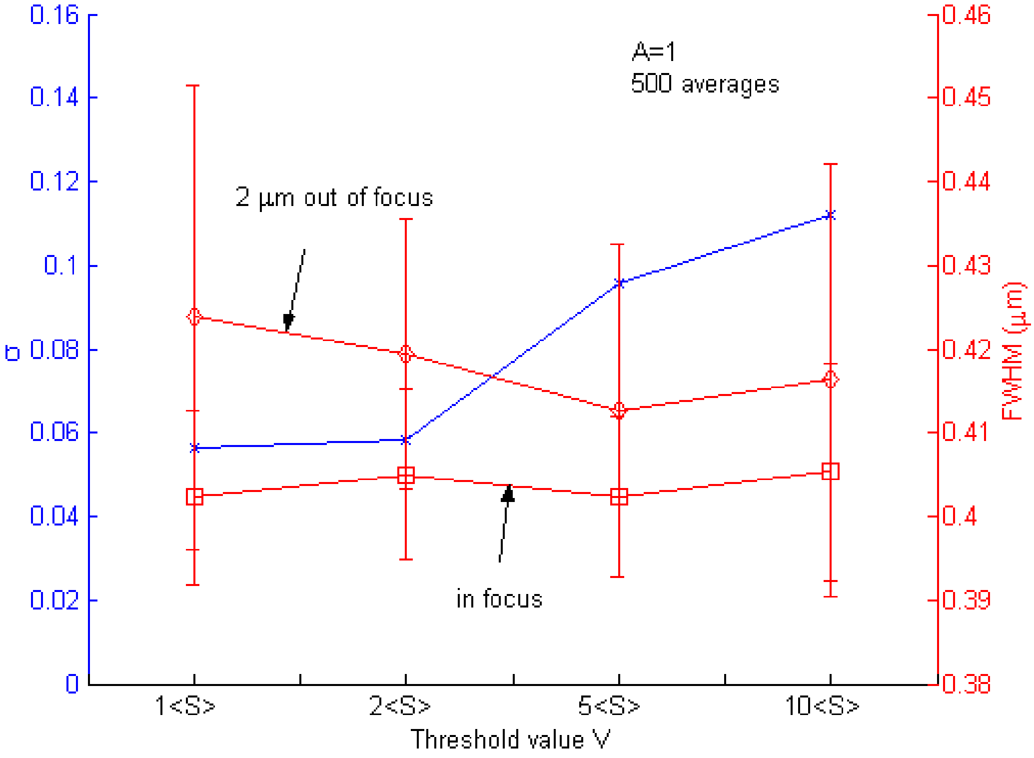

Fig. 5.15 The relations of σ and FWHM with threshold value V (A=1)

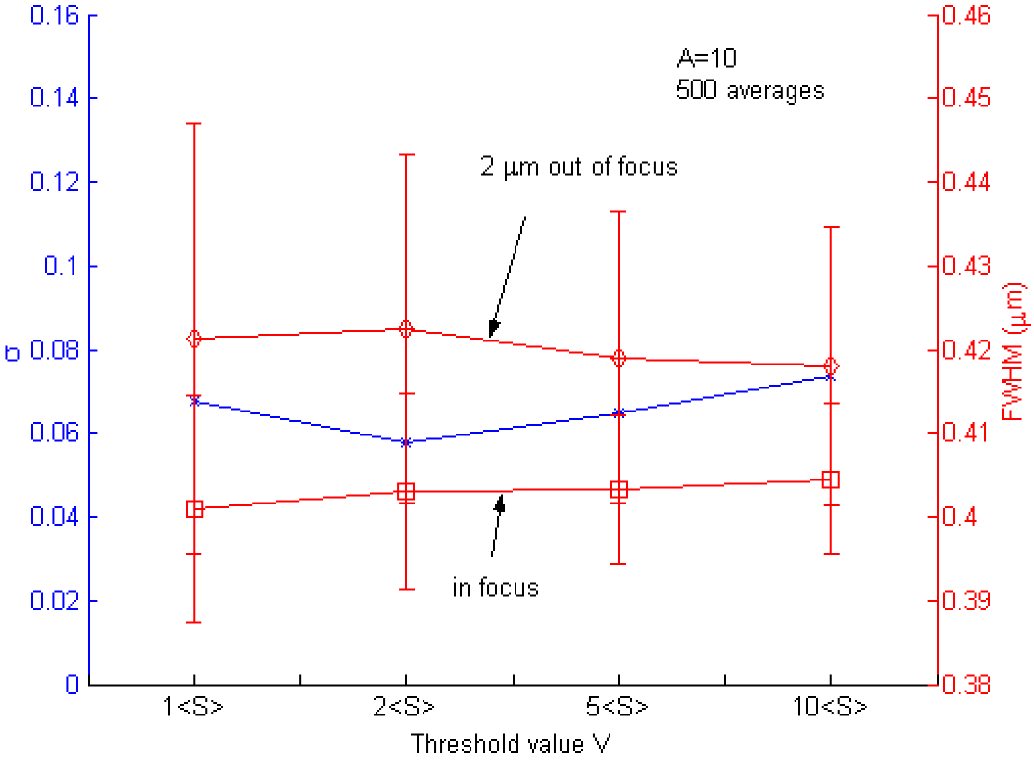

Fig. 5.16. The relations of σ and FWHM with threshold value V (A=10)

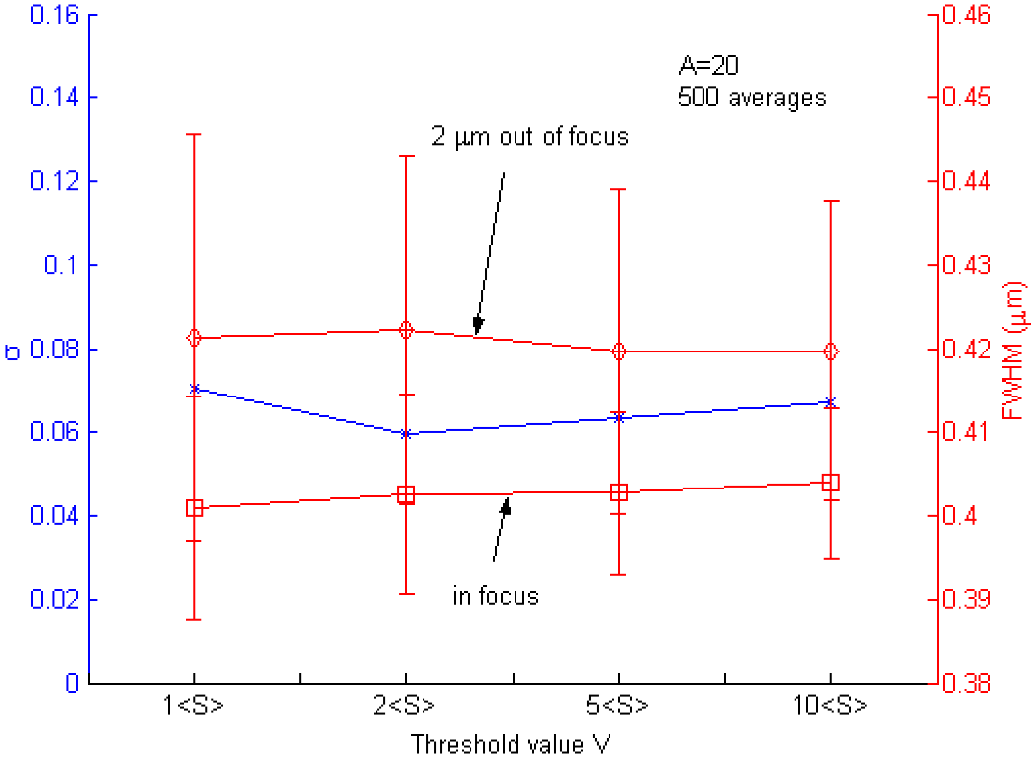

Fig. 5.17. The relations of σ and FWHM with threshold value V (A=20)

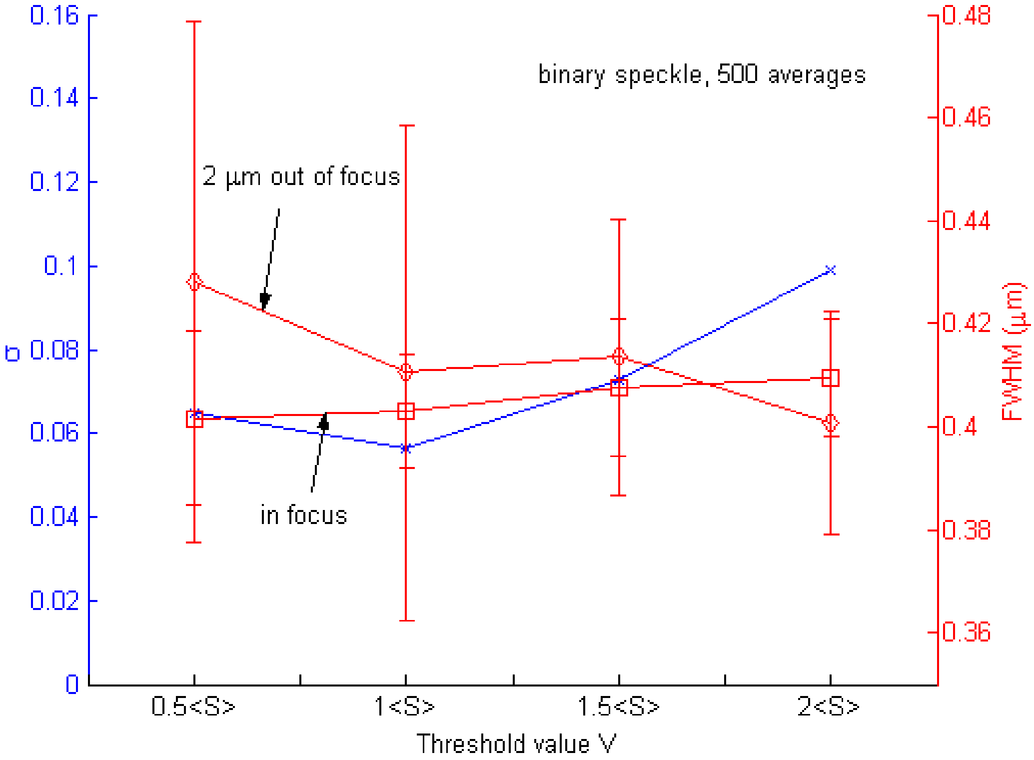

Fig. 5.18. The relations of σ and FWHM with threshold value V (binary speckle)

	A-Law			Binary
A V	1	10	20	
<S>				x
1.5<S>	x			
2<S>		x	x	
5<S>				

Table 5.1. Optimal parameters for speckle processing

It can be concluded that all the methods work at an acceptable standard when optimal parameters are chosen. In the practical system the choice of method could be made on the basis of which method is easier to implement.

6. Experimental confirmation

"Success is going from failure to failure without a loss of enthusiasm."

— Sir Winston Churchill, 1874-1965

A prototype optical bench system is constructed to demonstrate the practicality and effectiveness of the non-scanning confocal microscopy idea.

6.1 Experimental arrangement

A schematic diagram of the experimental arrangement is shown in Fig. 6.1. Illumination is from a laser beam passed through a rotating diffuser, a collimating lens and an objective. The dichroic beamsplitter directs the beam to form a speckle pattern throughout the specimen region. The fluorescent light from the object at a longer wavelength is imaged via the lenses and the beamsplitter onto the CCD camera. In this system, the fluorescence images and their corresponding illumination speckle patterns are recorded separately. This requires that the diffuser "remember" all the positions in a duty cycle and generate precisely the same sequence of speckle patterns repetitively. A stepper motor is used for this purpose. At every diffuser position, the camera takes a frame. A filter centred on the emission wavelength is used for blocking unwanted laser light in the fluorescence image recording session. In the speckle pattern recording session, the beamsplitter is replaced with a mirror turned by 90 degrees and a diaphragm is added to generate the correct speckle size. The experiment is aimed at demonstration of principle although the current arrangement would be slower than conventional scanning systems.

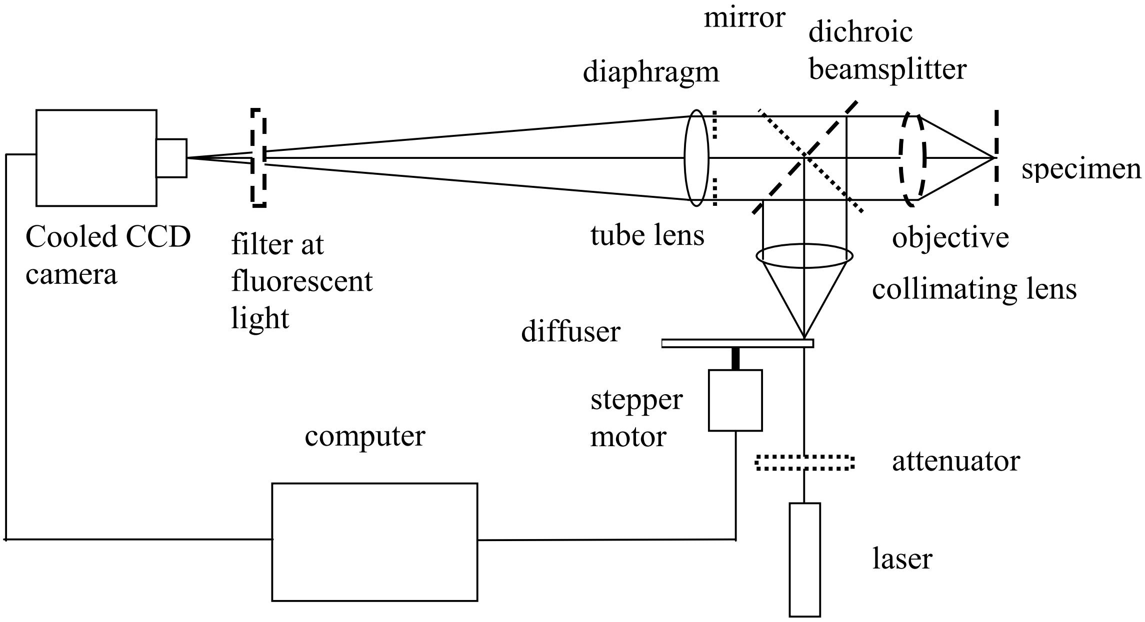

Dotted components: used in the speckle pattern recording session

Dashed components: used in the fluorescence image recording session

Solid components: used in both sessions

Fig. 6.1. A schematic diagram of the experimental arrangement

6.2 Apparatus

The apparatus which plays an important role in the experiment is described in this section.

6.2.1 Laser

A Sapphire 488-20 solid state laser supplied by Coherent Inc was chosen. The features of importance for this application are the 488 nm wavelength as many fluorescent dyes work at this wavelength and the variable output power. Its main specifications are given in Table 6.1 [62]. The Sapphire 488-20 belongs to a class of devices called Vertical External Cavity Surface Emitting Lasers (VECSEL). In conventional VECSELs, laser emission is driven (pumped) by electrical current. The Sapphire laser, in contrast, is optically pumped. It comprises a semiconductor pump laser, focusing optics, a unique InGaAs quantum-well semiconductor that serves as a gain medium and an output coupler, as illustrated in Fig. 6.2. Pump radiation from an 808 nm diode laser is focused on the OPS chip and absorbed by the quantum wells of the chip, providing gain at the fundamental IR wavelength. With the inclusion of an intra-cavity, nonlinear crystal, the infrared emission of the OPS chip is converted, via second harmonic generation, to visible light at 488 nm. A remarkable property of Sapphire is that the output is both single transverse mode (TEM00) and single longitudinal mode (single frequency). In addition, Sapphire consumes 98% less input power than argon iron lasers. It draws a maximum 60 W of electrical power, 50 W of which goes to the thermoelectric cooler that stabilizes the resonator independent of the environmental conditions. The remaining 10 W generates blue output. By comparison, the air-cooled iron laser requires 1.0 to 1.5 kW of power.

Wavelength	488 ±2 nm
Coherence length	>20 m
Output Power	1 ~ 20mW
Spatial Mode	TEM00, M2 <1.1
Beam Asymmetry	<1:1.1
Beam Diameter@ $1/e^2$	0.70 ±0.05 mm
Beam Divergence	<1.2 mrad
Pointing Stability (over 2 hours after warm-up and ±3°C)	<30 μrad
Noise 20 Hz to 2 MHz 20 Hz to 20 kHz, peak-to-peak	 <0.25% <1%
Long-term Power Stability (2 hours, ±3°C)	<2%
Polarization Ratio	>100:1, vertical

Table 6.1 Laser specifications

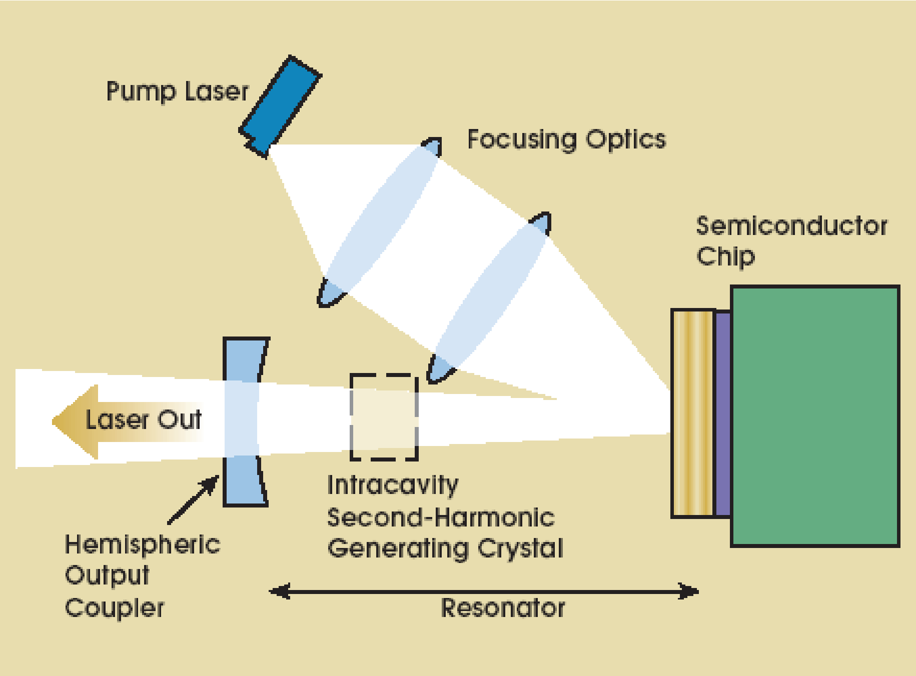

Fig. 6.2. Sapphire resonator

(From the May 2001 issue of PHOTONICS SPECTRA © Laurin Publishing)

6.2.2 *CCD camera*

The ORCA cooled CCD camera supplied by Hamamatsu Photonics has low dark noise and high quantum efficiency and is ideal for low-light level imaging. Its main specifications and spectral response characteristics are given in Table 6.2 and Fig. 6.3 respectively [63].

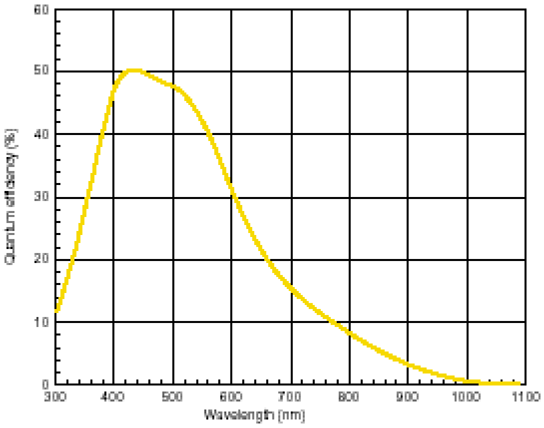

Fig. 6.3. Spectral response characteristics

Effective number of pixels	1280 (H) × 1024 (V)
Cell size	6.7 μm × 6.7 μm (square format)
Effective area	8.58 mm × 6.86 mm
Pixel clock rate	14.75M Hz/pixel
Frame rate	9 Hz
2 × 2 binning	18 Hz
4 × 4 binning	32 Hz
8 × 8 binning	53 Hz (option)
Readout noise (r.m.s.)	8 to 12 electrons
Full well capacity	13000 electrons
Dynamic range	1300:1
Cooling method	Peltier cooling, air radiation system
Cooling temperature	+5 °C
Dark current	1 electron/pixel/sec
A/D converter	12 bit
Output signal (digital output)	RS-422A 10/12-bit parallel output
Exposure time	130 μsec to 10 sec
Contrast enhancement	1 to 10 times
Power consumption	70 VA

Table 6.2. CCD camera specifications

6.2.3 Specimen

The TetraSpeck fluorescent microsphere supplied by Molecular Probe are stained with four different fluorescent dyes, displaying four well-separated excitation/emission peaks —365/430 nm (blue), 505/515 nm (green), 560/580 nm (orange), 660/680 nm (dark red). These microspheres are available in five diameters — 0.1, 0.2, 0.5, 1.0, 4.0 μm, ideal for subresolution sources and system calibration, especially in three-dimensional applications. The TetraSpeck Fluorescent

Microspheres Size Kit (T-14792) includes a sample of each size, plus a mixture of each size, mounted on six separate slides.

6.2.4 *Filters*

The dichroic beamsplitter is supplied by Omega Optical Inc. The spectra of the dichroic beamsplitter is shown in Fig. 6.4. The emitter, supplied by Ealing Electro Optics, has a central wavelength of 520 nm with a tolerance of ±10 nm.

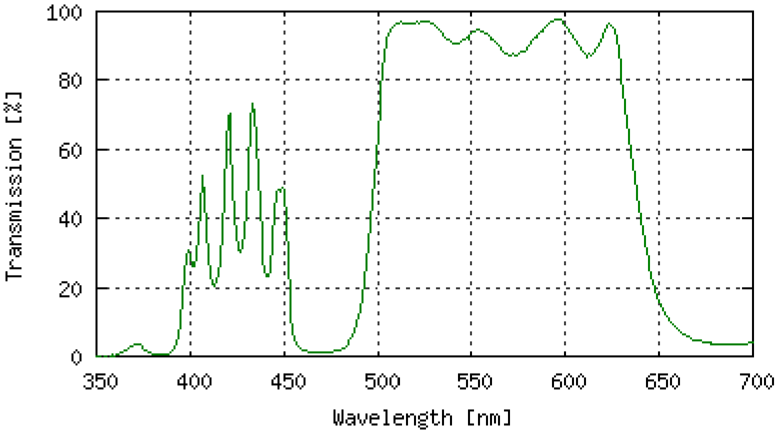

Fig. 6.4. Spectra of the beamsplitter

6.2.5 *Rotating diffuser*

At least 500 different speckle patterns for each image recording session are required. Such a great number of patterns are generated by a rotating diffuser which, driven by a stepper motor through a gearbox, has a high resolution of up to 1000 steps per degree. There are two types of speckle motion from a rotating diffuser [64]. If the observation plane in the extreme near field of the illuminated area, speckle translation will occur; the entire speckle pattern will move parallel to the motion of the illuminated surface with little change in the shape or relative position of the individual speckles. In the extreme far field, speckle boiling will occur; the speckles will randomly evolve with no apparent displacement of the overall pattern. It is easy to see from Fig. 6.1 that the speckle motion in our experiment just belongs to the first type. In this case, the overall pattern at two consecutive diffuser positions appears to move some distance without boiling. If the diffuser moves a distance smaller than the illuminating spot, the two identical patterns may partly overlap within the field of view. It is not clear whether this scenario will affect the averaging process, so the diffuser is required to move a distance larger than the laser spot to avoid overlapping. As the size of the laser spot is 0.7 mm and the disc is 120 mm in diameter, the maximum number of frames within one turn will be limited to $120\pi/0.7\approx538$. For convenience it is rounded to an integer of 500 by setting 720 steps for an angular movement each time, which is 360/500 = 0.72°.

6.3 Principal parameters

The experimental system must meet the following requirements:

1. The Rayleigh resolution distance of the objective should be greater than the size of fluorescent beads which are used as subresolution point sources
2. The numerical aperture of the objective is sufficiently large, as the light emanating from the fluorescent beads is very weak
3. Each fluorescent bead should be magnified large enough so that its image occupies a reasonable number of CCD pixels to satisfy the Nyquist sampling condition (at least 2 pixels across the FWHM of a star image)
4. There are a reasonable number of beads within the field of view, preferably 10 or more, depending on the sample

Obviously the first requirement calls for a low-aperture objective and smaller beads while the second calls for a high-aperture objective and larger beads. As a compromise, we select the 4 μm fluorescent beads as the test specimen and a 5 time objective with an NA of 0.12. Such an objective cannot resolve two 4 μm beads separated 2 μm from each other when working in the type 1 (conventional) mode but should be able to resolve them in the type 2 (confocal) mode. Given a magnification of 20 which enables the image of a single bead to occupy 12 CCD pixels with a cell size of 6.7 μm, the focal length of the tube lens is then determined. Note that the image of the bead actually occupies 6 pixels because 2×2 binning[*] is used throughout the experiment. This is equivalent to 7.5 pixels across the intensity PSF (a bit oversampling). The principal parameters for the experimental system are listed in Table 6.3.

Size of sample fluorescent beads	4 μm in diameter
Wavelength of laser light	$\lambda_1 = 488$ nm
Wavelength of fluorescence light	$\lambda_2 = 520$ nm
Numerical aperture of the objective	NA = 0.12
Focal length of the objective	$f_1 = 25.5$ mm
Rayleigh resolution distance	$\sigma = 0.61\lambda_2/\mathrm{NA} = 2.64$ μm
Speckle size on the object plane	$1.22\lambda_1/\mathrm{NA} \approx 5$ μm
Focal length of the tube lens	$f_2 = 500$ mm
Magnification between the object and image planes	M = f2/f1=19.61 ≈ 20
Aperture diameter of the diaphragm	$2f_1\mathrm{NA}$=6.12 mm
Field of view	≈ 430 μm × 340 μm
CCD resolution	640 × 512 pixels (2 × 2 binning)
Focal length of the collimating lens	$f_3 = 30$ mm
Angular movement of the diffuser	0.72°
Number of steps per revolution for the diffuser	500

Table 6.3. Principal parameters for the experimental system

---

[*] A way of increasing camera sensitivity by combining signals from multiple pixels, but this process reduces image resolution.

6.4 Light budget

A major problem experienced is the heavy loss of light due to the diffuser. With the laser of 20 mW output power the incident power at the specimen is measured to be only 0.6 mW which is not sufficient for fluorescence emission. A collimating lens is therefore employed to converge the light scattered by the diffuser, thus increasing the illumination power to 3 mW, and giving about 10^{-6} – 10^{-7} mW of emerging fluorescent light at 520 nm emanating from the 4μm fluorescent bead specimen.

6.5 Image noise analysis

For the cooled CCD camera, *thermal noise* is not dominant, so noise in the image can be considered as coming from two sources, *readout noise* and *Poisson noise* (shot noise). From Table 6.2 the readout noise of the CCD camera can be assumed to be 20 electrons. The quantum efficiency of the camera is 50% according to Fig. 6.2. In the fluorescence image recording session the CCD camera is exposed to the 4 μm microsphere sample at a signal level of, presumably, 2×10^{-7} mW for 1 sec. Since 1 mW of light intensity at 500 nm is equivalent to 2×10^{15} photons/sec [65], the number of photons absorbed at each pixel would be 400 (assuming an image of 1000×1000 pixels). This is just the case described in Ref. [16] from which a whole paragraph is quoted as follows:

"In general terms, detector noise is most important at very low photon levels, Poisson noise at higher levels. In a typical cooled CCD camera, the measurement noise, mostly *readout noise* from the A/D converter in the camera, is about ten electrons (r.m.s.) per pixel. This means that if many measurements of exactly the same number of electrons were made, the standard deviation (root mean square deviation from the mean value) would be ten. So, if exactly 100 electrons had accumulated in a particular pixel in the array, there would be a probability of about 70% that the measured number would be between 90 and 110. The detective quantum efficiency varies between 20% and 80% depending on the wavelength and the CCD chip design. Let us assume 50%. This means that the detector noise is equivalent to about 20 incident photons. Poisson noise arises because the emission and detection of photons is a random process and fluctuates according to the Poisson distribution. So if many measurements of a 'uniform' flux of photons were made using a perfect measurement device, then the standard deviation of these measurements would be given by the square root of the mean value. So, if the detected number of photons is 100, we can regard this as a sample of a probability distribution whose mean is 100 and whose standard deviation is 10. Thus at a signal level of 400 photons, the Poisson noise would be 20 photons — the same level as the detector noise. At this signal level we could expect an r.m.s. noise-to-signal ratio of around 7% (400 photons measured with 20 photons Poisson noise and the equivalent of 20 photons detector noise — since the two sources of noise are independent we can add their contributions as the square root of the sum of their squares). With a higher signal level, the shot noise would be greater than the (signal-independent) detector noise."

It should be noted that the above analysis does not take into account the influence of external stray light, flare or light scattered by the elements of the optical system and the light scattered through the object, which is thus cross talk between object points. The former, which is constant in intensity over the detector, merely serves to reduce contrast and can be subtracted from the detected signal. The latter in the measured signal can be assumed to be uniformly distributed, so the intensity is proportional to the area of the detector and also depends on the strength of the signal. The quantifying of flare level is difficult and will not be discussed here.

6.6 Experimental results

6.6.1 Acquisition of raw images

The raw images of the specimen and the speckle pattern recorded with the arrangement shown in Fig. 6.1 is different in their orientation, because in the fluorescence image recording session the specimen is imaged inverted on the CCD camera, while in the speckle recording session the image is erect. For this reason either set of raw images must be flipped vertically prior to further processing. In addition, in the speckle recording session the mirror must be accurately adjusted to make sure that the corresponding points of the speckle pattern and the fluorescence image are registered on the same pixel of the CCD camera, otherwise the fluorescent spheres in the image do not look perfectly round. However it is very difficult to find out whether a speckle pattern is correctly registered, as it looks completely different from its corresponding fluorescence image. To solve this problem we replace the fluorescent beads, when the fluorescence image recording session is completed, with a uniform fluorescent microscope slide supplied by Omega Optical Inc., and record an incoherent speckle pattern generated by this slide. This incoherent speckle pattern, as shown in Fig. 6.5(a), looks blurry but bears a resemblance to the coherent one shown in Fig. 6.5(b) and therefore can be used as a reference for judging by the eye whether the coherent speckle pattern is correctly registered while the mirror is being adjusted.

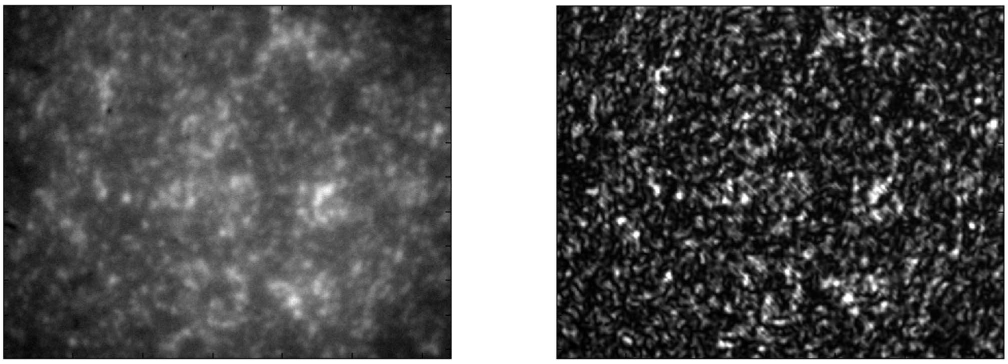

(a) Incoherent speckle pattern (b) Coherent speckle pattern

Fig. 6.5. The incoherent speckle pattern bears a resemblance to the coherent one

The CCD camera is controlled by the image acquisition software WASABI. By means of the Time Lapse Recording function provided, a sequence of images can be acquired easily and stored to the computer's hard disk as digital data. The rotating diffuser is controlled by an in-built script list that specifies all the actions required of the stepper motor before or after each image is acquired. An individual raw image of fluorescent beads taken with an exposure time of 1 sec and a corresponding speckle pattern are shown in Fig. 6.6. The histograms in Fig. 6.7 clearly show a negative exponential intensity distribution in the speckle pattern. Note that the maximum value $S_{\max}$ is equal to 4095 and the mean $\overline{S}$ is equal to 620, giving $S_{\max} \approx 6.6\overline{S}$ rather than $S_{\max} \approx 10\overline{S}$ as mentioned in subsection 3.5.1. This is because the minimum intensity in the speckle pattern is at a level of about 210 rather than zero due to the background noise. Since the recorded speckle pattern is from the extreme near field of the diffuser, as mentioned in section 6.2.5, it should be noted that the bright spots in Fig. 6.6(b) do not look very evenly distributed (the central portion contains more bright spots than the surrounding) due to the surface irregularities of the hand-made diffuser.

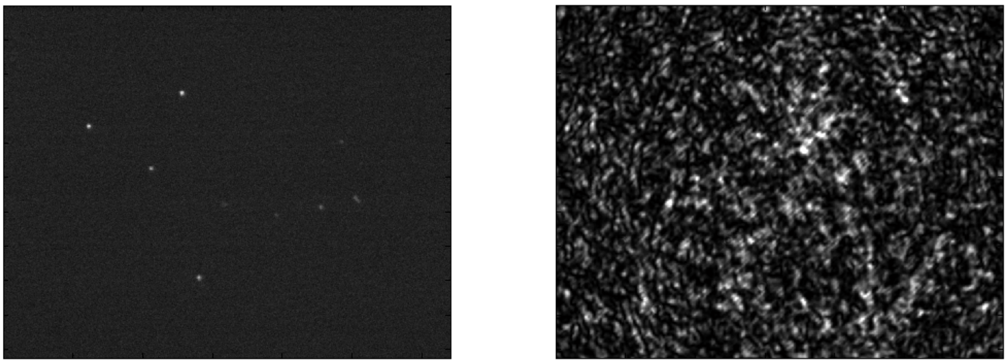

(a) Fluorescent beads (b) Speckle pattern

Fig. 6.6 An individual raw image (640×512×12)

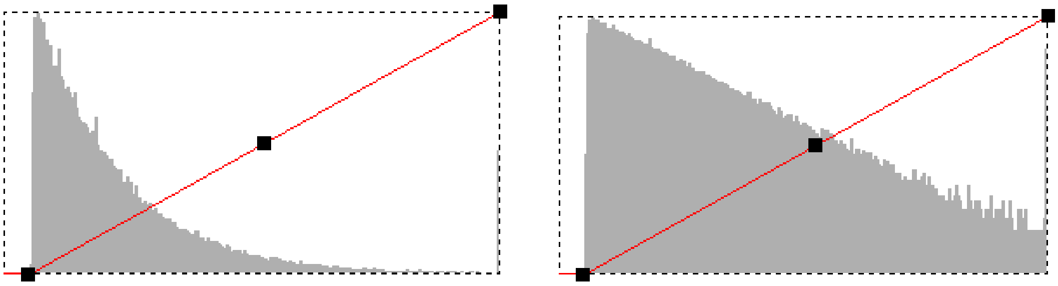

(a) Linear histogram (b) Logarithmic histogram

Fig. 6.7 Histograms of the speckle pattern in Fig. 6.6(b), $V = 4095$, $\overline{S} \approx 625$

6.6.2 *Postprocessed images and discussion*

The recorded raw speckle patterns can be used to generate processed speckle, viz. A-law compressed, intensity thresholded and binary speckle patterns as shown in Fig. 6.8 using the methods mentioned in Chapter 5.

A type 1 image of the 4 μm fluorescent microspheres can be obtained by taking an average over 500 individual fluorescence images each illuminated with a different speckle pattern. A series of such images at focal position of 0, 20 and 40 μm are shown in Figs 6.9(a) to (d) respectively. It may be seen that there is a considerable amount of flare present in the images which comes mostly from external stray light and light scattered by the elements of the optical system. Figs 6.9(e) to (h) show the non-scanning or type 2 images at the same focal positions using equation (2.18) and averaging over 500 frames, giving an evident depth discrimination property, enhanced lateral resolution and reduced effect of flare. Figs 6.10(a) to (h) show the type 2 images averaged with A-Law compressed speckle patterns. Figs 6.11(a) to (h) show the type 2 images averaged with intensity thresholded and binary speckle patterns respectively. Surface and profile plots of the local regions illustrated in Figs 6.9 (a), 6.9(e), 6.10(a), 6.11(a) and 6.11(e) are shown in Figs 6.12 (a), (b), (c), (d) and (e) respectively. In may be seen that the rightmost double bead can hardly be resolved for the type 1 case, but is clearly resolved for the type 2 case.

The effect of speckle processing on the processed images can be discerned from the profile plots of Fig. 6.12, although the differences between the performance of the A-Law processing and binarisation operation are small, as has been pointed out in Section 5.3. The threshold values chosen for the images in Figs. 6.12(c), (d) and (e) are 4095, 2047 and 0.3×4095, which are equivalent to $6.6\overline{S}$, $3.3\overline{S}$ and $2\overline{S}$ respectively. According to the blue curves in Figs. 5.16 to 5.19, their corresponding intensity non-uniformity σ is read to be 0.07, 0.08 and 0.1 respectively. This means that Fig. 6.12(c) has the best image quality in the sense that its intensity non-uniformity σ is the lowest. Fig. 6.12(e) is worse than (c) and (d) since its intensity non-uniformity σ is 0.1, but it is still better than (b) whose intensity non-uniformity σ is around 0.14 according to the black curve of Fig. 5.4. This speculation has been confirmed with the experimental results. It should be emphasized that all the methods improve the image uniformity at an acceptable standard.

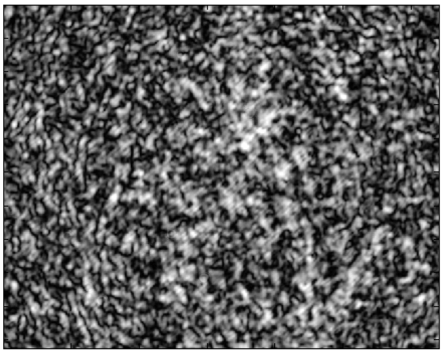

(a) A-law compressed, $A = 10$, $V = 4095$

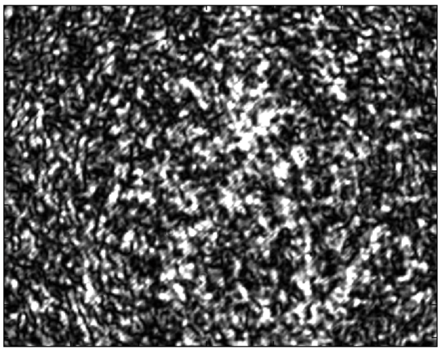

(b) intensity thresholded, $A = 1$, $V = 2047$

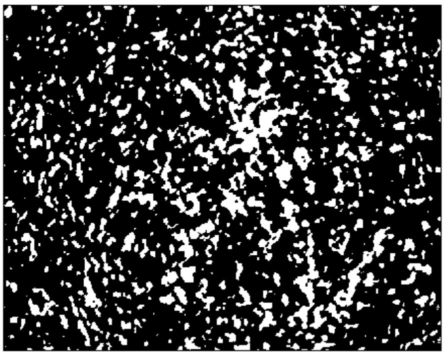

(c) binary, threshold value = 0.3×4095

Fig. 6.8 Processed speckle patterns

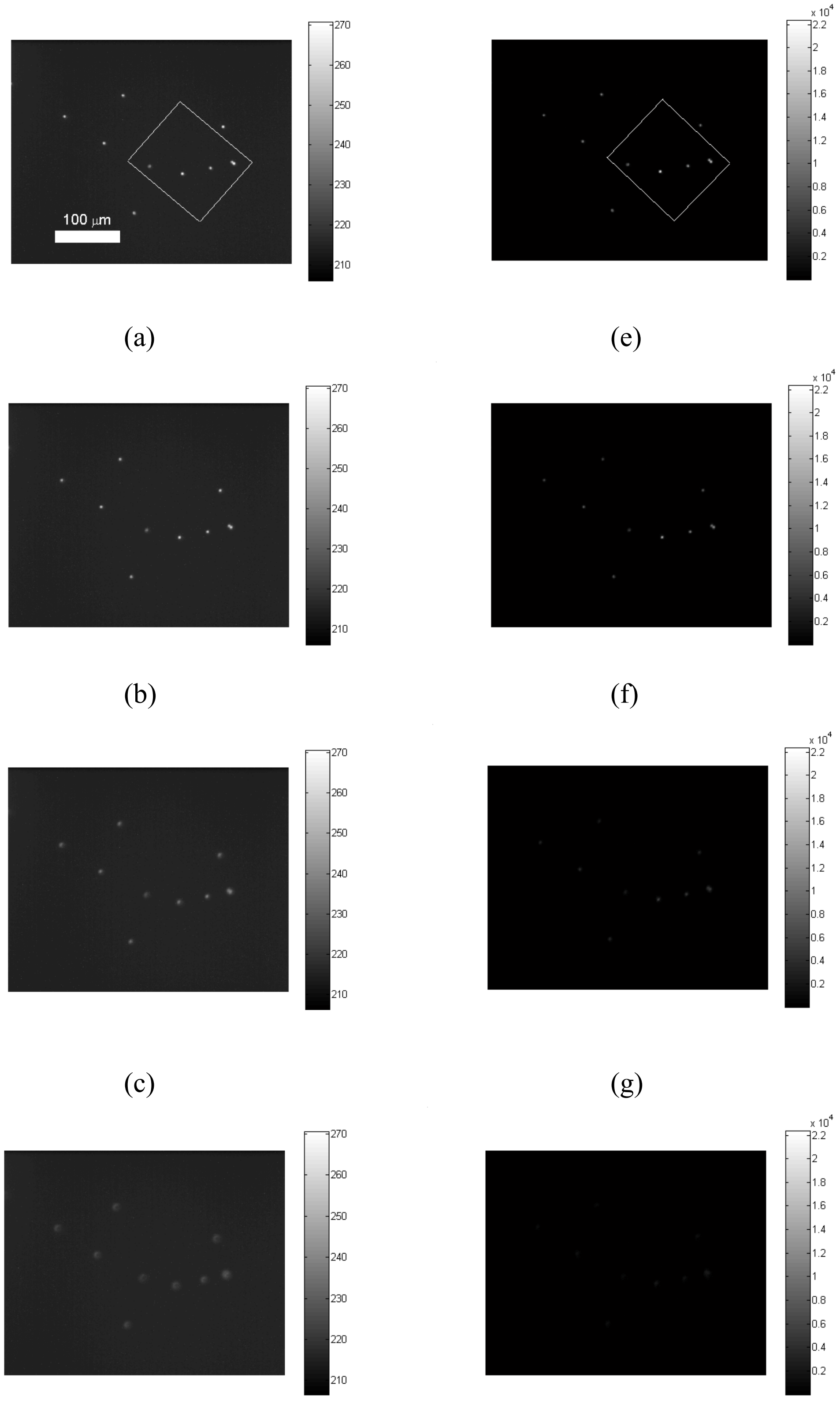

(a) (e)

(b) (f)

(c) (g)

(d) (h)

(a), (b), (c) and (d): type 1 images; (e), (f), (g) and (h): type 2 images

Fig. 6.9. Images of 4 micron fluorescent microspheres (640 × 512 × 12) at focal positions of 0, 20, 40 and 60 μm

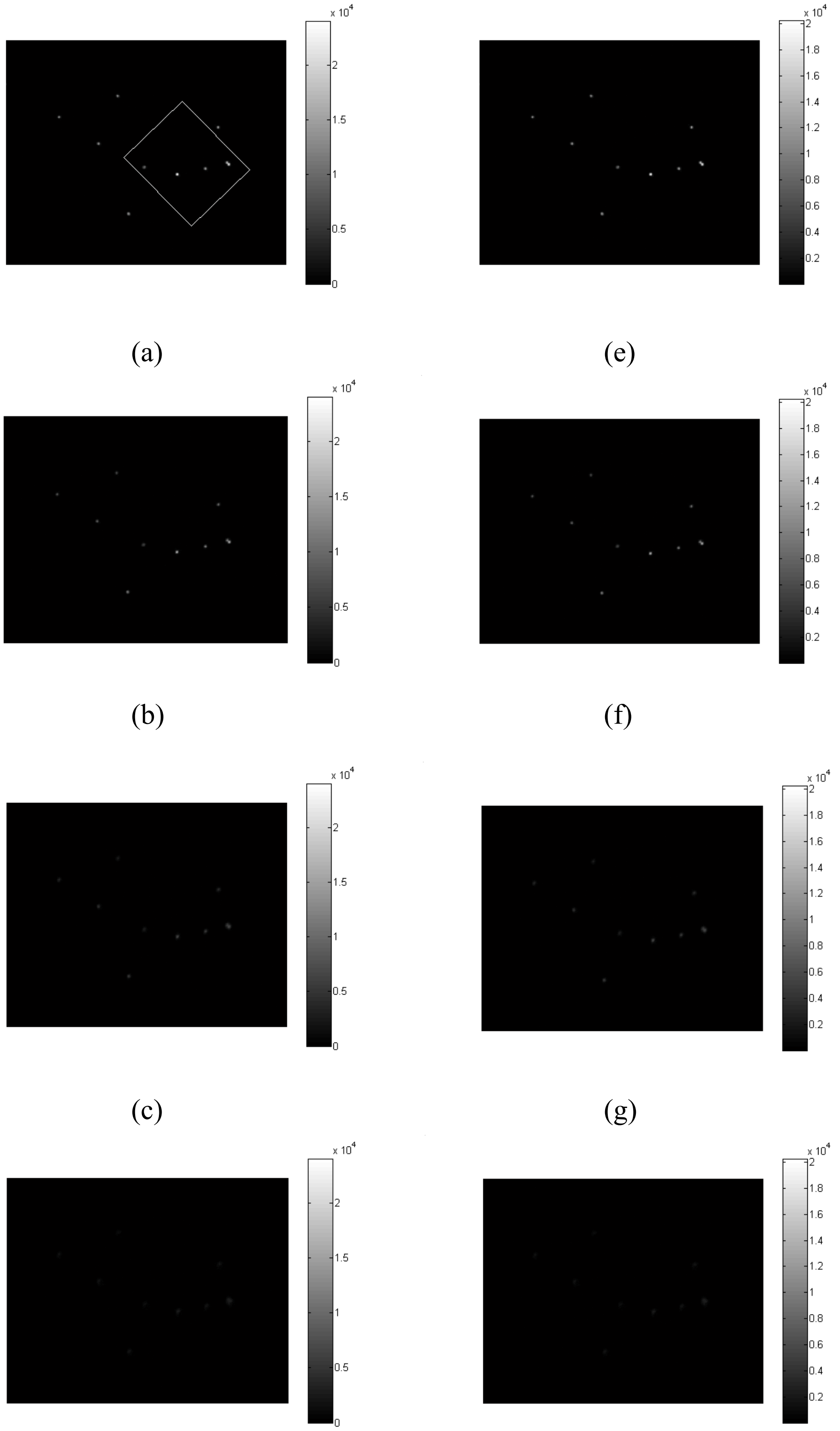

(a) (e)

(b) (f)

(c) (g)

(d) (h)

(a), (b), (c) and (d): A=10, V= 4095; (e), (f), (g) and (h): A=20, V=4095

Fig. 6.10 Images of 4 micron fluorescent microspheres (640 × 512 × 12) at focal positions of 0, 20, 40 and 60 μm, averaged with A-Law compressed speckle

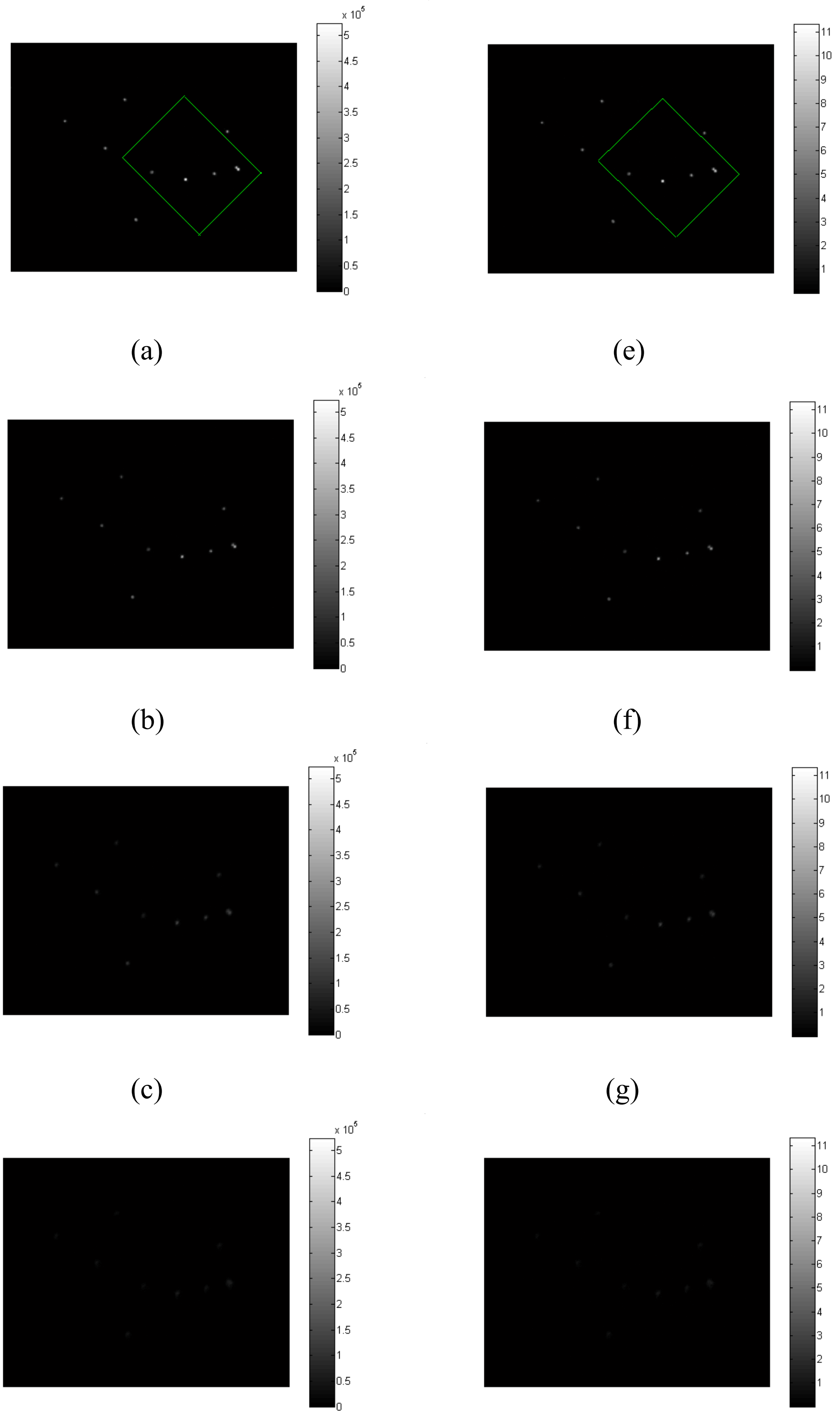

(a) (e)

(b) (f)

(c) (g)

(d) (h)

(a), (b), (c) and (d): Thresholded, V= 2047

(e), (f), (g) and (h): Binary, V=0.3×4095

Fig. 6.11 Images of 4 μm fluorescent microspheres (640 × 512 × 12) at focal positions of 0, 20, 40 and 60 μm, averaged with thresholded and binary speckle respectively

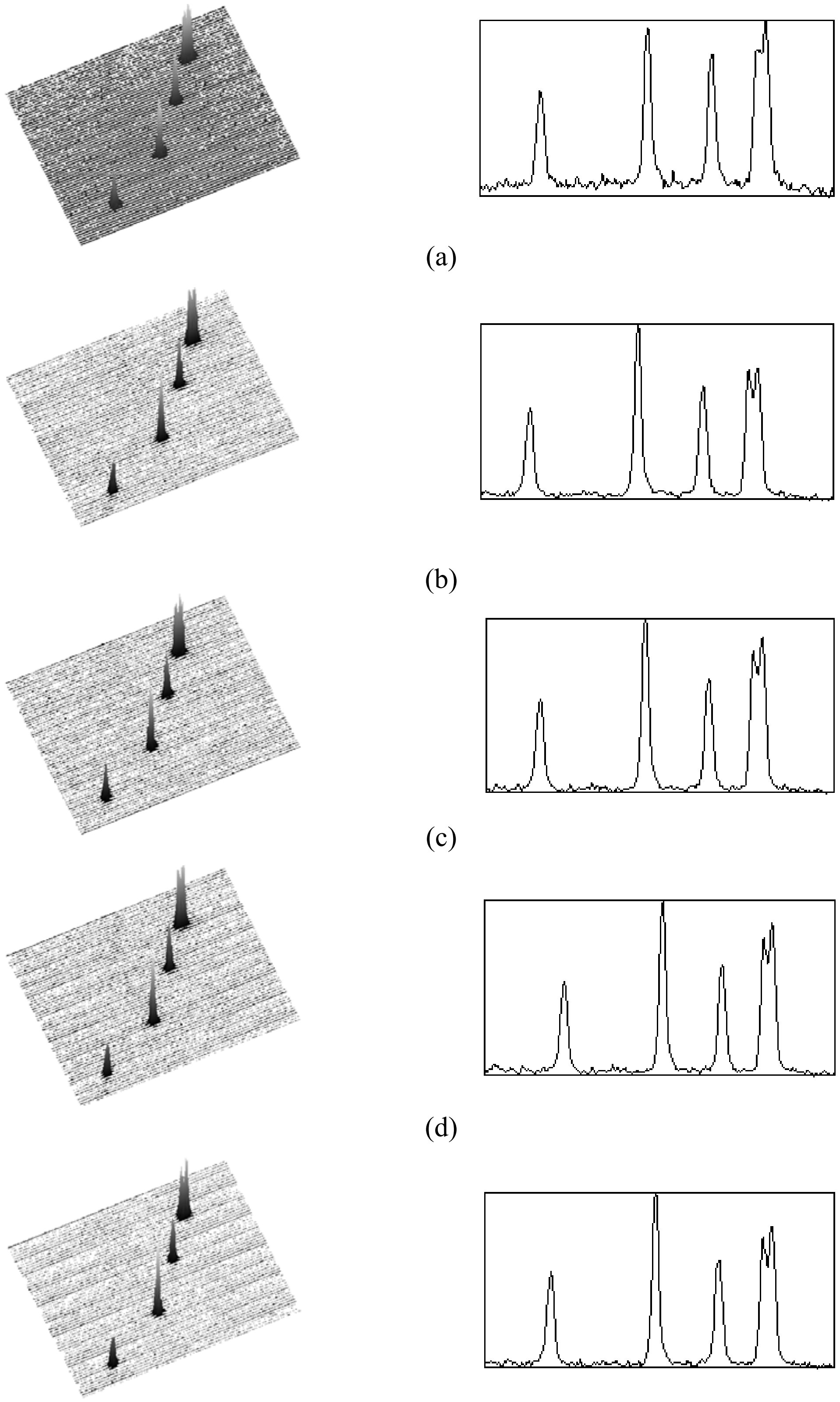

(a): type 1, (b): type 2, (c): type 2 with A-law compression, (d): type 2 with thresholding operation, (e): type 2 with binarisation operation

Fig. 6.12 Surface and profile plots of local regions

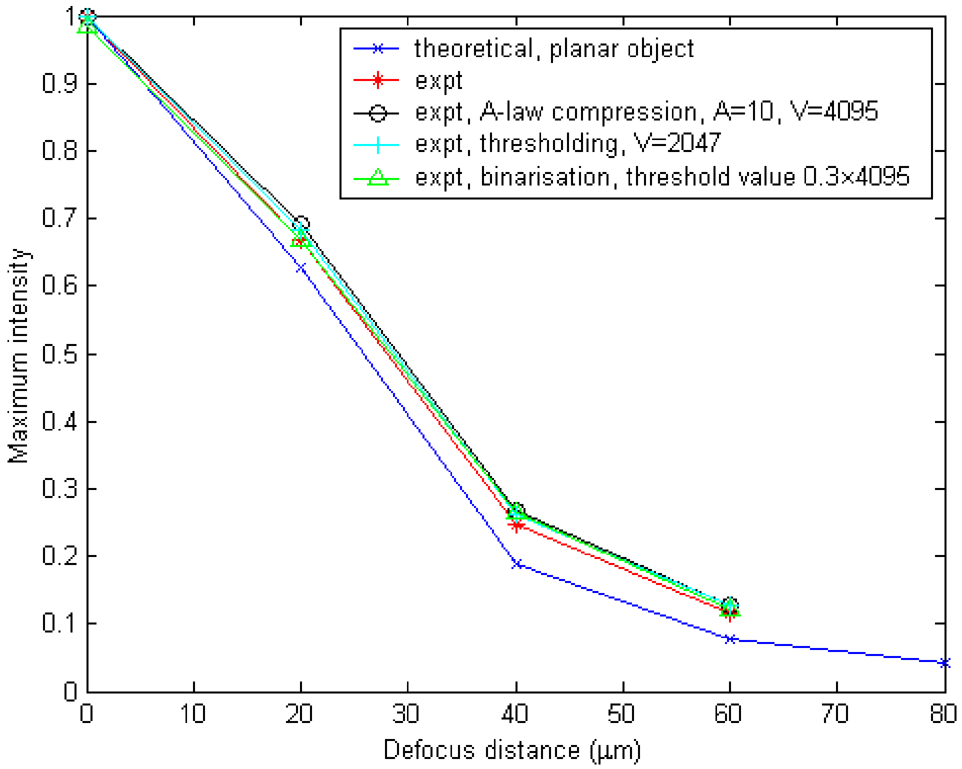

Fig. 6.13 Comparison of depth discrimination property

Fig. 6.13 shows a comparison of depth discrimination property between theory and experiment. Note that the theoretical curve is obtained from a scanning confocal system with a uniform planar object. It is reasonable to do so because theoretically the non-scanning confocal microscope has the same 3-D optical transfer function as a scanning one whose longitudinal frequency bandwidth is identical for both the low and high transaxial frequency components. The intensity variation in a non-scanning system accounts for a discrepancy of less than 10%.

The above experimental results exhibit excellent agreement with theory and improved performance predicted by computer simulation. In particular, the results confirm the dramatic effect of non-scanning microscope on the removal of additive white noise present in each individual frame as mentioned in subsection 3.5.3.

7. Real-time optical data processing

As has been pointed out earlier, the arrangement described in the previous chapter is slow in data collection and hence is unsuitable for imaging of biological tissue like living cells. This chapter is devoted to an investigation of reduction in data collection time by means of optical data processing and analogue frame averaging, because optical data processing can be performed in real time and analogue frame averaging can be implemented by taking a single CCD readout. To this end, a modified experimental system is set up where a miniature transmissive *liquid crystal display* (LCD) is employed to perform a real-time multiplication operation between two individual frames. An LCD used in combination with an analogue CCD camera behaves as an *optically addressed spatial light modulator* (OASLM) [66]. The reason why such a configuration was adopted instead of simply using a commercial OASLM is that the latter is too expensive. For example, the ENST Bretagne OASLM with a frame rate of 1 KHz was priced at 10k euros in 2004. Of course, the cheaper LCD used in our experiment has a low transmission of 22% and a low frame rate of 60 Hz, compared with those high-speed SLM devices whose frame rate can exceed 1 MHz, such as the Lenslet Ablaze SLM based on MQW GaAs technology [67]. A problem associated with such a low transmission and low frame rate is that the LCD will display a smeared image when using dynamic speckle patterns generated with a rotating diffuser. This smearing effect will become serious with the increase in rotating speed of the diffuser and will reduce the transmission of the LCD. Under such circumstances the LCD will seriously block the weak fluorescent light coming from the sample. Because of this limitation, it is required that the speckle patterns change very slowly with time and the exposure time of the CCD camera be long enough to allow the averaging process to complete. Although this will extend the total frame acquisition time to a few tens of seconds, the experimental set-up is still of great value to the demonstration of principle and promises the feasibility of fast confocal imaging. As will be demonstrated later in section 7.7, the experimental results obtained with analogue frame averaging are very encouraging. Fast imaging on the second scale in two exposures should be possible as long as a high-transmission, high-speed device is employed. For comparison purposes, experimental results obtained with digital frame averaging are also presented.

7.1 Experimental arrangement

A schematic diagram of the experimental arrangement is shown in Fig. 7.1. A laser beam passes through a rotating diffuser, a collimating lens and a dichroic beamsplitter where it is split into an illumination beam and a reference beam. The illumination beam is directed through an objective to form a speckle pattern throughout the specimen region. The fluorescent light from the object at a longer wavelength is imaged via the objective and the beamsplitter onto an LCD. The reference beam, after passing through an attenuator, a diaphragm and a zoom lens, forms a speckle pattern on a CCD camera. The diaphragm and the zoom lens are used to generate a speckle pattern that is displayed on the LCD with correct magnification and speckle size via a video-to-VGA converter. The fluorescence image modulated in its intensity by the LCD is then focussed onto a cooled CCD via a relay lens and a filter at the wavelength of the fluorescent light. While the diffuser is rotated, a sequence of fluorescence images can be recorded with each one modulated by a different speckle pattern. Like the arrangement shown in Fig. 6.1, the diffuser is controlled by a stepper motor that can rotate either step by step or continuously. A picture of the experimental set-up is shown in Fig. 7.2.

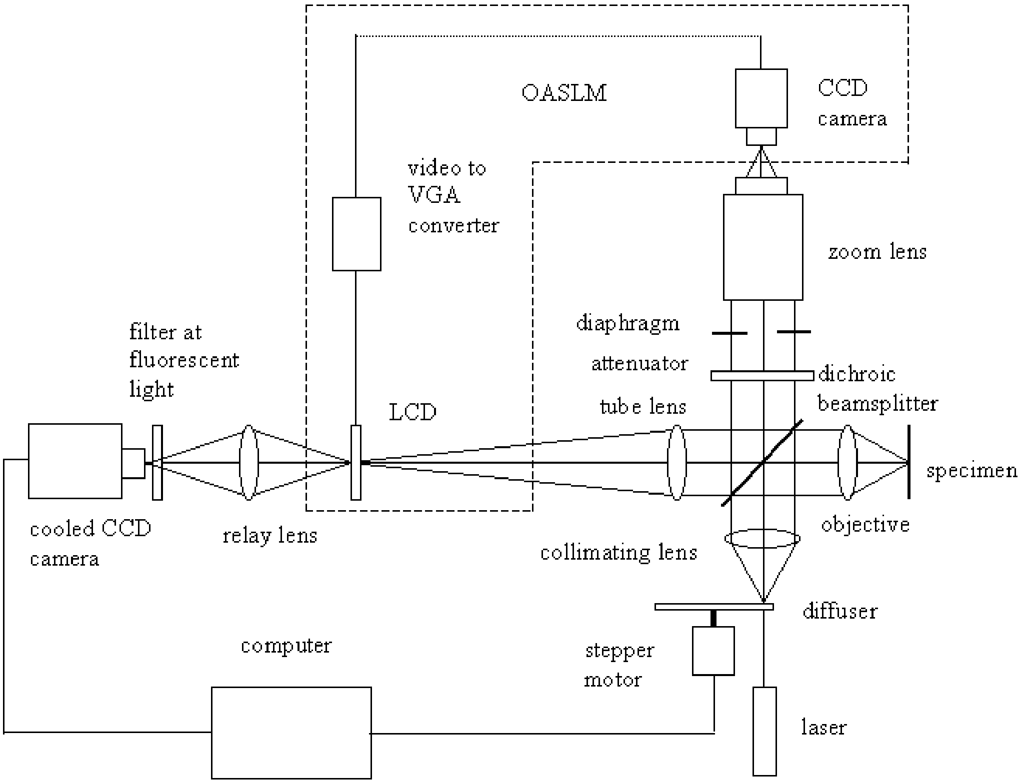

Fig. 7.1. A schematic diagram of the experimental arrangement

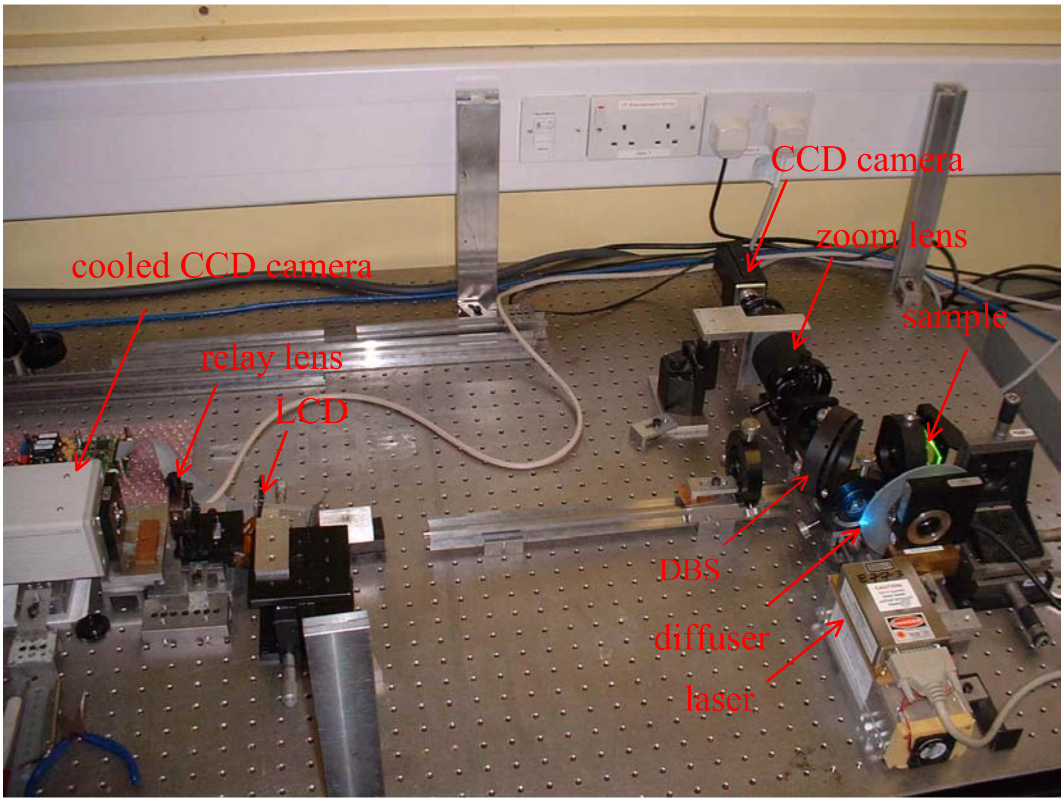

Fig. 7.2. A picture of the experimental set-up

7.2 The transmissive miniature liquid crystal display

The liquid crystal display (LCD) can be used in transmissive or reflective mode. A transmissive LCD is illuminated from one side and viewed from the other side. Activated cells therefore appear dark while inactive cells appear bright. The 1.3″ (33mm) diagonal miniature transmissive LCD for our experiment is supplied by CRL Opto Ltd. The LCD panel is an active matrix, thin film transistor (TFT) type that uses a twisted nematic liquid crystal material. When used in conjunction with suitable external polarisers, the panel is capable of a contrast ratio of greater than 100:1 for greyscale imagery and its response is fast enough to allow the display of motion video with minimal smearing. The panel is connected to the interface PCB via a ribbon cable, allowing the LCD to be mounted remotely from the interface. The interface accepts the standard video graphics signal generated by the video adaptor of a personal computer. Therefore an AV Tool AVT-3300 video-to-VGA converter has been employed to convert the output signal of the analogue CCD from composite video format to VGA mode. The specifications of the LCD unit are listed in Table 7.1 [68].

Interface timing mode	SVGA 800 × 600 @ 60Hz
Spatial resolution	800 (horizontally) by 600 (vertically) monochrome pixels
Pixel pitch	33μm (H) × 33μm (V)
Pixel dimensions	28μm (H) × 24μm (V)
Panel dimensions	Active area 26.6mm (H) × 20.0mm (V)
Transmission	22% typical
Fill factor	62%
Contrast ratio	>100:1

Table 7.1. Specification of the LCD

7.3 Principal parameters

In addition to the points to determine the system parameters discussed in Section 6.3, a new factor that should be considered is the influence of the pixelated structure of the LCD. Since the pixel size of the LCD is about five times that of the cooled CCD camera, the image of the beads falling on the LCD has to be magnified by the same amount to eliminate the effect on resolution. This suggests a change in the magnification between the sample and the LCD from 20, set in the previous experiment, to 100 and requires a subsequent increase in the focal length of the tube lens to 2500 mm if the objective stays the same. Needless to say, the bench system with a lens of such a long focal length will have to be a folded one and not look respectable. For this reason, we keep the magnification unchanged at 20, which results in the image of a single bead occupying about 2.4 LCD pixels with unwanted dark grid pattern imposed due to the pixelated structure of the LCD. However, this shortcoming is trivial and would be overcome if a high-resolution XGA (1024 × 768 pixels) LCD with a smaller pixel pitch of 18×18 μm could be used. The principal parameters determined for the experiment are listed in Table 7.2.

Size of sample fluorescent beads	4 μm in diameter
Wavelength of laser light	$\lambda_1 = 488$ nm
Wavelength of fluorescence light	$\lambda_2 = 520$ nm
Numerical aperture of the objective	NA = 0.12
Focal length of the objective	$f_1 = 25.5$ mm
Rayleigh resolution distance	$\sigma = 0.61\lambda_2/NA = 2.64$ μm
Speckle size on the object plane	$1.22\lambda_1/NA \approx 5$ μm
Focal length of the tube lens	$f_2 = 500$ mm
Magnification between the object and LCD panel	$M_1 = f2/f1 = 19.61 \approx 20$
Focal length of the relay lens	$f_3 = 40$ mm
Magnification between LCD and cooled CCD	$M_2 = 1$
Aperture diameter of the diaphragm	$2f_1NA = 6.12$ mm
Field of view	≈ 430 μm × 340 μm
CCD resolution	640 × 512 pixels (2 × 2 binning)
Focal length of the collimating lens	$f_4 = 30$ mm

Table 7.2. Principal parameters for the experiment

7.4 Optical data processing

Obviously, the ensemble average $\langle I \cdot S \rangle$ in the first term of formula (2.18) can be obtained by recording a sequence of individual LCD modulated images $I \cdot S$ and then calculating the average. The following requirements must be met to ensure the speckle pattern is *correlated*:

- Each image I is modulated with the speckle pattern S which is simultaneously used to illuminate the sample
- The position of the LCD panel must be precisely adjusted to allow the image I to be accurately registered with the corresponding pixel locations on the LCD panel

The modulated image formed at the cooled CCD detector can then be expressed as

$$I(x,y)S(x,y)+n(x,y) \tag{7.1}$$

where n is the inevitable additive white noise. The LCD acts as an optical valve whose liquid crystal cells are individually controlled by variable S to control the amount of light transmitted. Obviously S should fall into the range of $0 \le S \le 1$.

To obtain the second term $\langle I\rangle\langle S\rangle$ in formula (2.18) in a suitable way, several different approaches have been investigated:

1. Recording a sequence of individual fluorescence images without LCD modulation and an additional sequence of speckle patterns. Inserting (7.1) into the first term of the averaging formula (2.18) and (3.15) into the second term gives

$$\begin{aligned} I_p^1 &= \langle IS+n\rangle - \langle I+n\rangle\langle S\rangle \\ &= \langle IS\rangle + \langle n\rangle - \langle I\rangle\langle S\rangle - \langle n\rangle\langle S\rangle \\ &= I_p^0 + \langle n\rangle(1-\langle S\rangle) \end{aligned} \tag{7.2}$$

where $I_p^0 = \langle IS\rangle - \langle I\rangle\langle S\rangle$ is the ideal processed image. It is clear that the noise cannot be removed because the intensity distribution in a speckle pattern obeys a negative-exponential probability density function, its probable maximum intensity is approximately ten times the value of its mean (see Section 3.5.1), hence $\langle S\rangle \approx 0.1$. Figs. 7.3, 7.4 and 7.5 show the simulated averaged image with LCD modulation $\langle IS+n\rangle$, the averaged image without LCD modulation $\langle I+n\rangle$ and the processed image I_p^1 respectively. The simulated white noise with a mean equal to 40% of the maximum signal level and a standard deviation of 2.5% of the mean is added to each fluorescence frame. It may be seen that I_p^0 is seriously masked by noise. Therefore this approach is not usable.

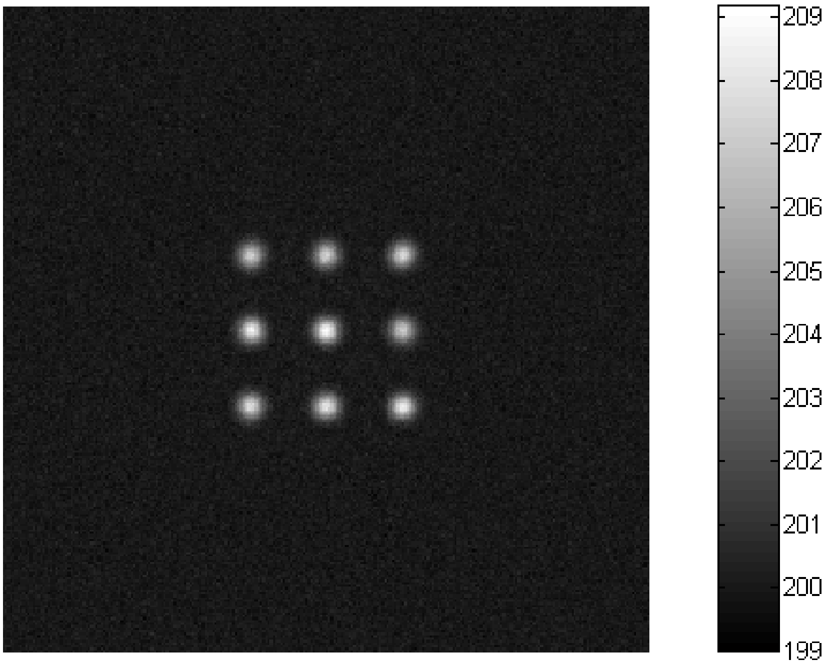

Fig. 7.3. The averaged image with LCD modulation $\langle IS + n \rangle$

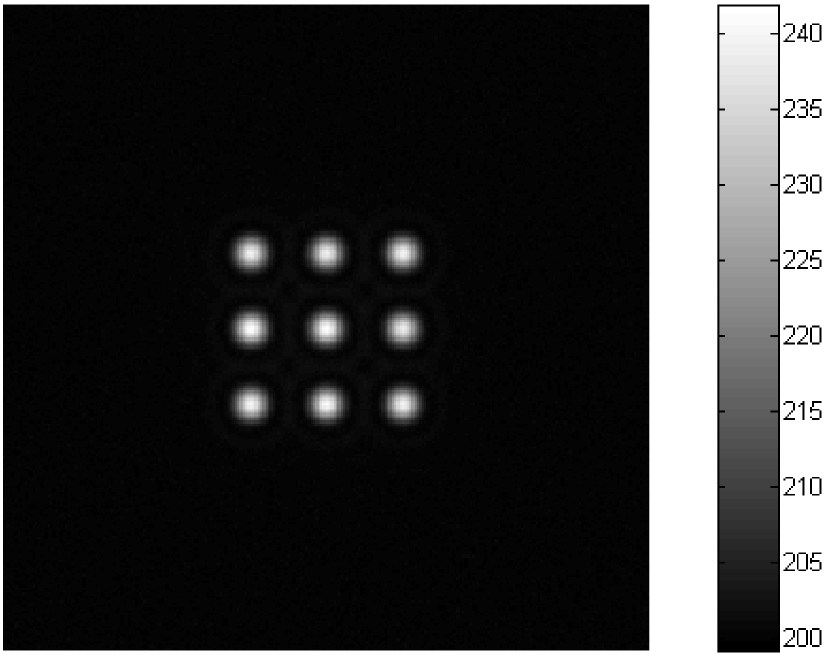

Fig. 7.4. The averaged image without LCD modulation $\langle I + n \rangle$

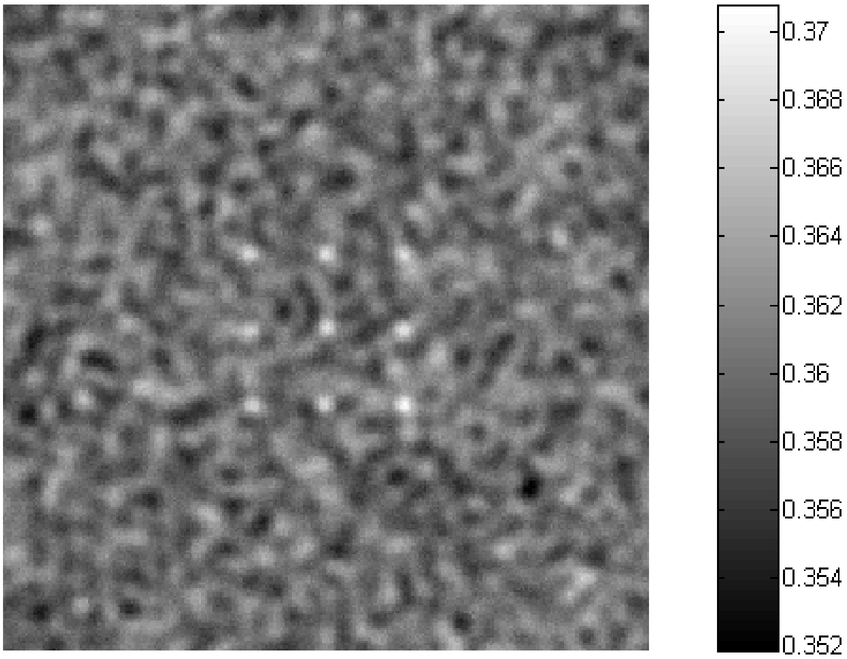

Fig. 7.5. The processed image I_p^1

2. Recording a sequence of individual fluorescence images without LCD modulation and substituting a constant C for $\langle S\rangle$. The processed image then becomes

$$\begin{aligned} I_p^2 &= \langle IS+n\rangle - \langle I+n\rangle C \\ &= \langle IS\rangle + \langle n\rangle - \langle I\rangle C - \langle n\rangle C \\ &= \langle IS\rangle - \langle I\rangle C + \langle n\rangle (1-C) \end{aligned} \tag{7.3}$$

In order to obtain the ideal image I_p^0, we require $C = \langle S\rangle \approx 0.1$, but the noise cannot be removed unless $C = 1$. Apparently both conditions cannot be satisfied with the same constant. Fig. 7.6 show the simulation result when $C = 1$. The processed image I_p^2 obtained by subtracting $\langle I+n\rangle$ in Fig. 7.4 from $\langle IS+n\rangle$ in Fig. 7.3 becomes negative and definitely not a type 2 image although the noise has been completely removed. The experimental results shown in Figs. 7.7, 7.8 and 7.9 confirm the simulation very well. The modulated image $\langle IS+n\rangle$ is obtained with the LCD on, while the unmodulated image $\langle I+n\rangle$ is obtained with the LCD off, so that the constant $C=1$. We conclude that this approach is unusable too.

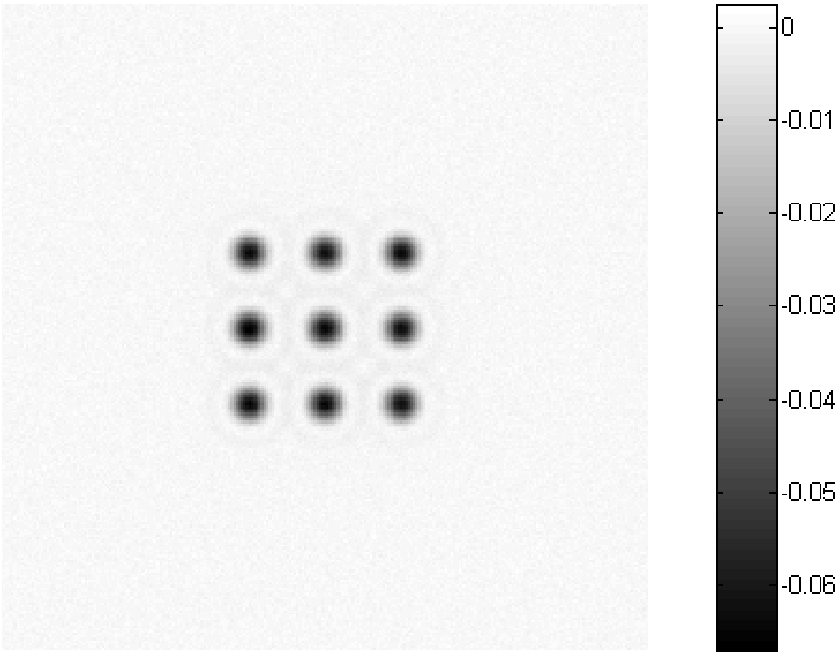

Fig. 7.6. The simulated processed image I_p^2

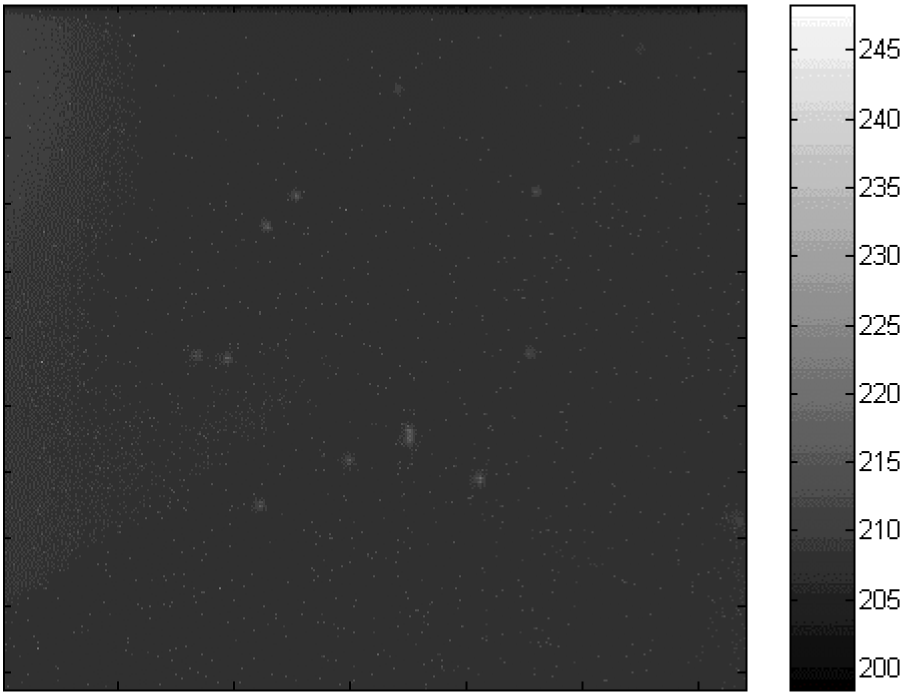

Fig. 7.7 The averaged LCD modulated image $\langle IS+n\rangle$

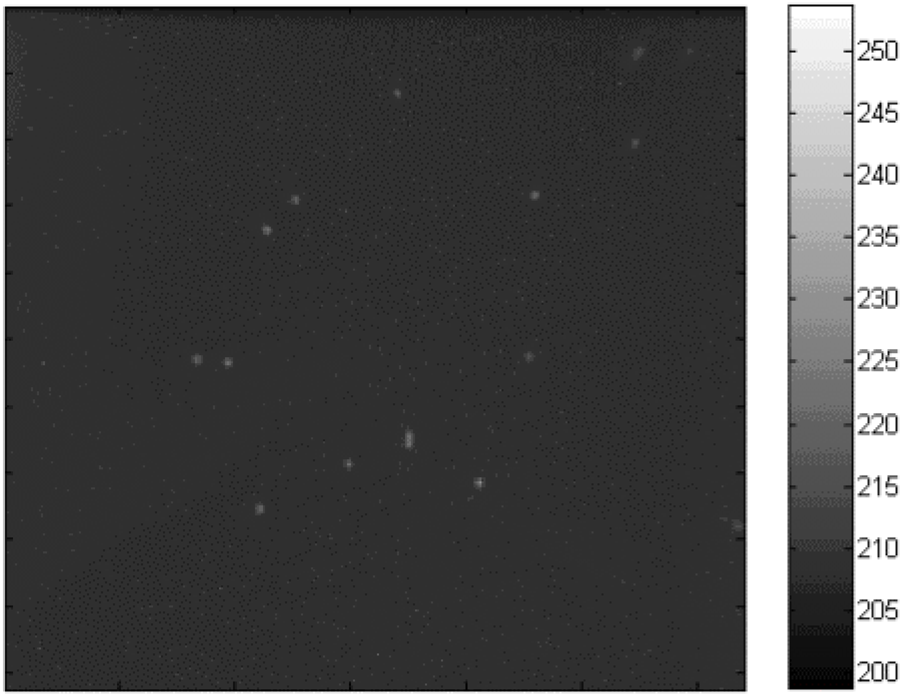

Fig. 7.8 The averaged unmodulated image $\langle I+n\rangle$

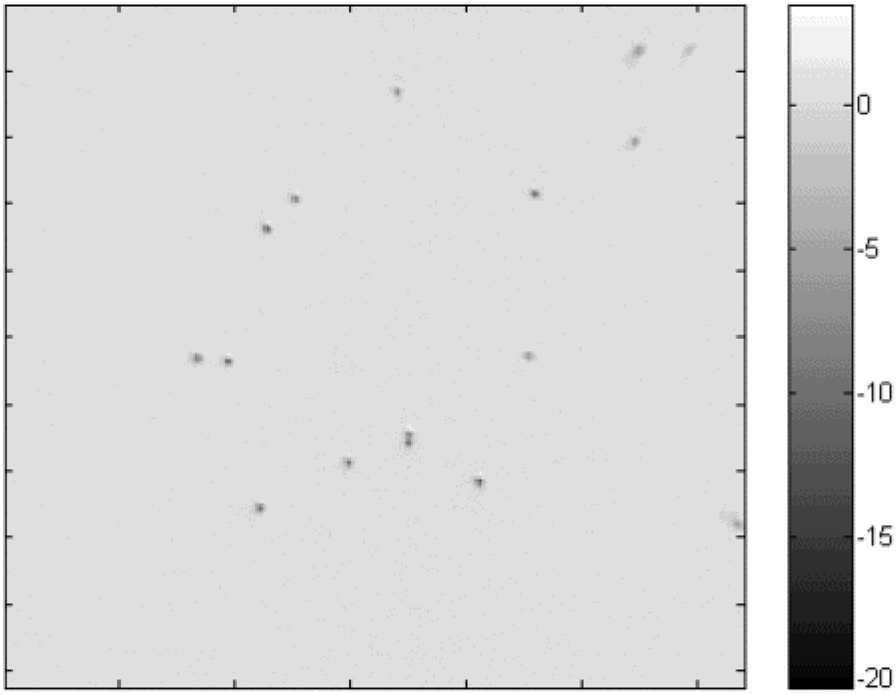

Fig. 7.9 The processed image I_p^2

3. Recording a sequence of fluorescence images each modulated by an *uncorrelated* speckle pattern *S*'. The processed image is then given by

$$\begin{aligned} I_p^3 &= \langle IS + n \rangle - \langle IS' + n \rangle \\ &= \langle IS \rangle + \langle n \rangle - \langle IS' \rangle + \langle n \rangle \\ &= \langle IS \rangle - \langle I \rangle \langle S' \rangle \\ &= I_p^0 \end{aligned} \tag{7.4}$$

Note that the ensemble average of the product of two uncorrelated random variables is equal to the multiplication of their ensemble averages:

$$\langle IS' \rangle = \langle I \rangle \langle S' \rangle \tag{7.5}$$

and clearly,

$$\langle S' \rangle = \langle S \rangle \tag{7.6}$$

The uncorrelated speckle pattern can be obtained by shifting the LCD laterally by a small distance Δx or Δy that should exceed one speckle diameter, namely

$$S'(x, y) = S(x - \Delta x, y) \tag{7.7}$$

Fig. 7.10 shows the simulated averaged image $\langle IS'+n \rangle$ obtained by shifting the LCD horizontally by 20 pixels (equivalent to the speckle size). Fig. 7.11 shows the processed image obtained using formula (7.4), and Fig. 7.12 the processed image with its negative components suppressed. It is interesting to see that the image has a satisfactory visual quality with most of the noise removed. Compared with approaches 1 and 2, we conclude that approach 3 is a promising way forward, as it can process data all-optically in two measurements taken with the LCD on and with no need for knowledge of $\langle S \rangle$ or $\langle S' \rangle$.

A downside of this approach is that the image intensity uniformity is a bit worse than the two-detector system, and the noise level is relatively high. This is because the correlated speckle $\langle S \rangle$ in formula (2.18) is replaced with the uncorrelated speckle $\langle S' \rangle$. According to the previous system performance evaluation, the image intensity non-uniformity is dependent on the number of averaging. The simulation results for this dependence is illustrated in Fig. 7.13 where the first column shows the ideal images from a conventional microscope, the second column shows the ideal images from a fluorescence scanning confocal microscope, the third to six columns show the images obtained using formula 7.4, but averaged over 500, 1000, 1500 and 2000 independent frames with additive white noise. It can be seen that the intensity non-uniformity and the residual noise are reduced with the increase in the number of averaging. From the discussion in Chapter 5, the intensity uniformity can be improved through speckle processing. A comparison between different speckle processing methods is shown in Fig. 7.14. Unfortunately the unwanted intensity non-uniformity is about twice that of the two-detector arrangement. The processing of binary speckle and thresholding are not significantly effective, and the best candidate is the A-Law processing which gives an improvement of about 15%. A quantitative analysis of signal-to-noise ratio for the non-scanning image in Fig. 7.13 was conducted using the same procedure as described in section 3.5.3. The results (with the threshold value equal to 0.1) are shown in Fig. 7.15. The in-focus image SNR of the SLM based system is between 5-9, much lower than that of the two-detector system from Fig. 3.12.

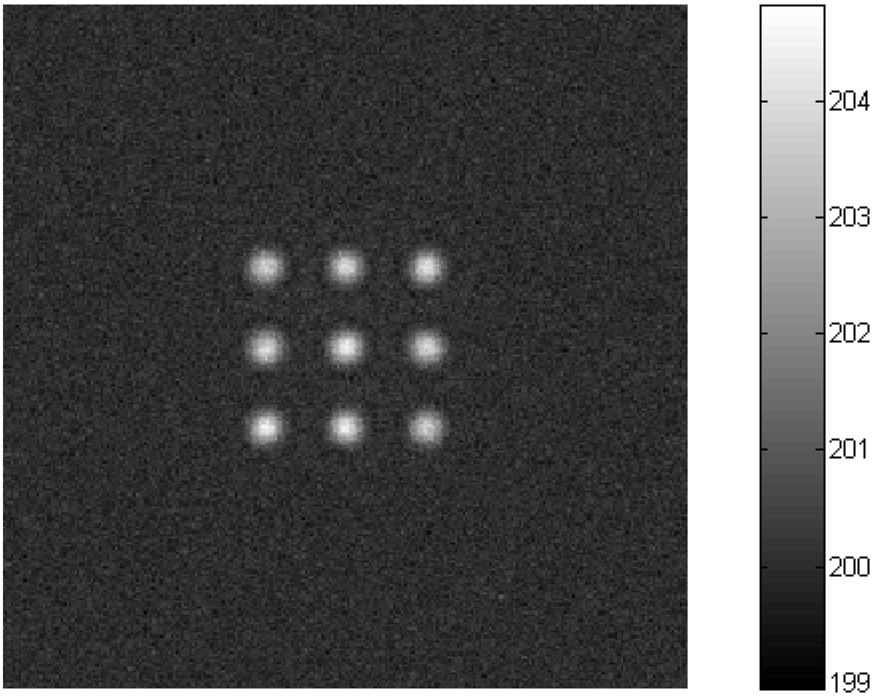

Fig. 7.10. The averaged image modulated by uncorrelated speckle pattern $\langle IS'+n \rangle$

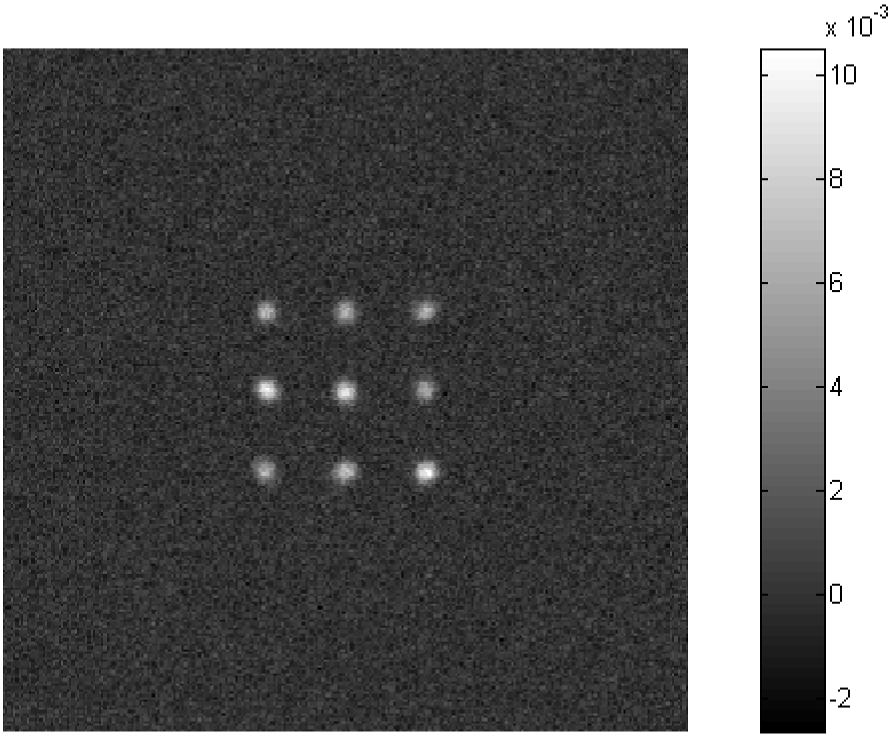

Fig.7.11. The processed image $I_p^3 = \langle IS + n \rangle - \langle IS' + n \rangle$

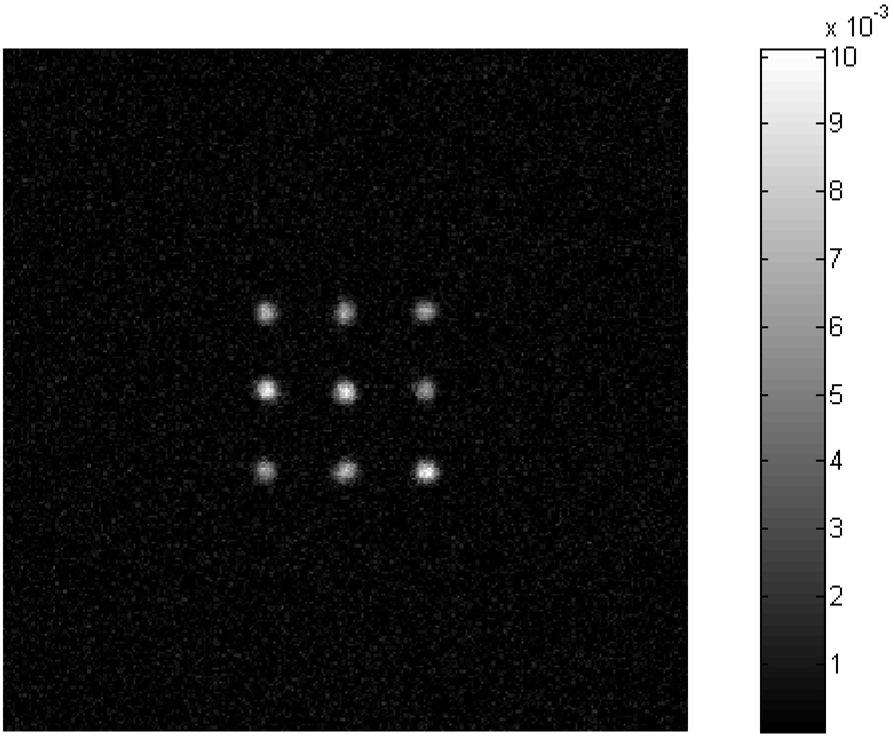

Fig. 7.12. The processed image with its negative components suppressed

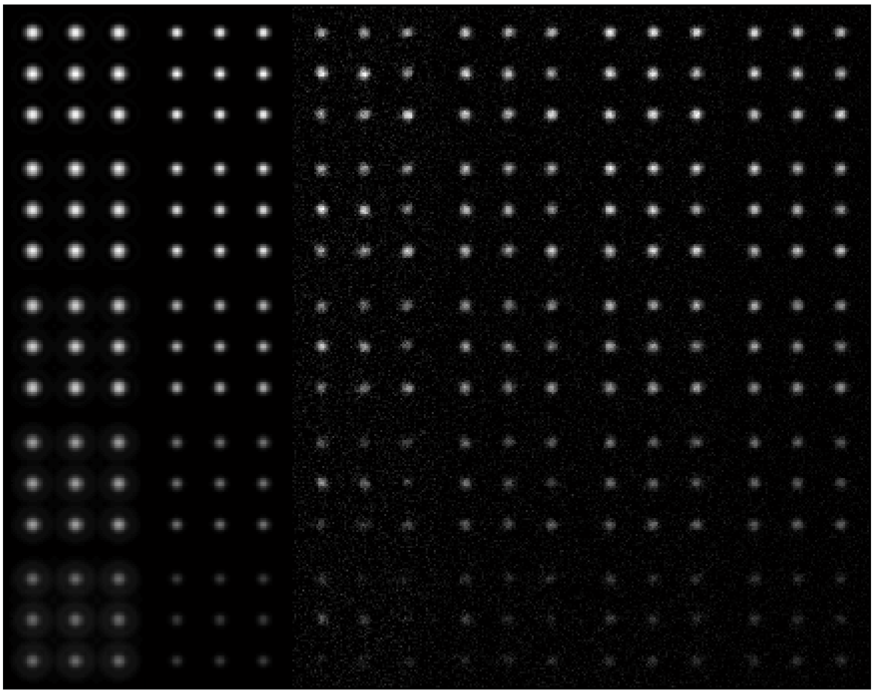

(a) Greyscale images

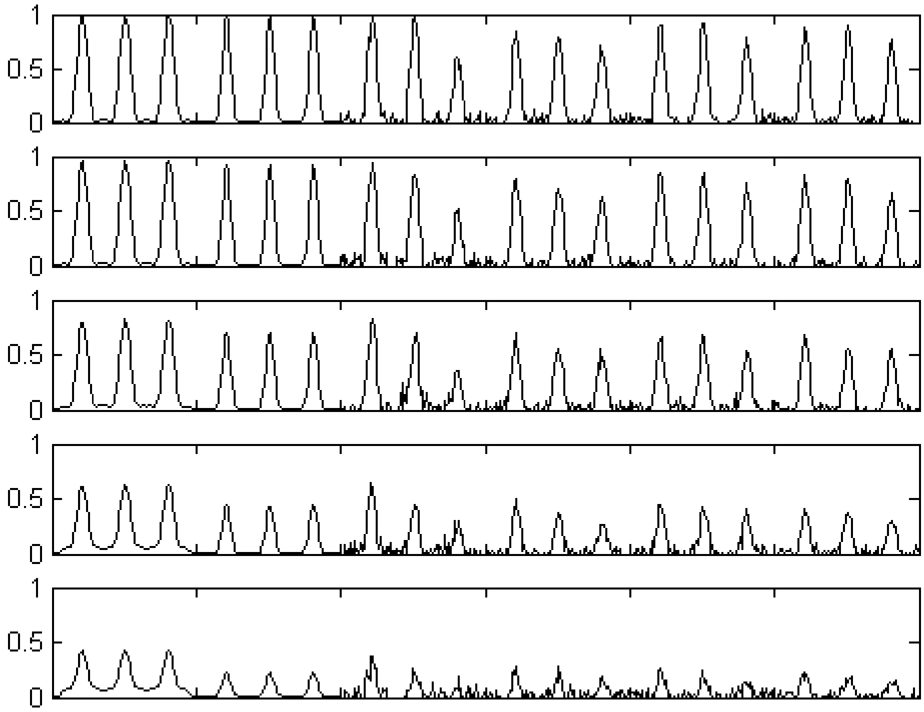

(b) Intensity distribution sliced along the central line of each panel
Fig. 7.13. Simulation results using uncorrelated speckle processing

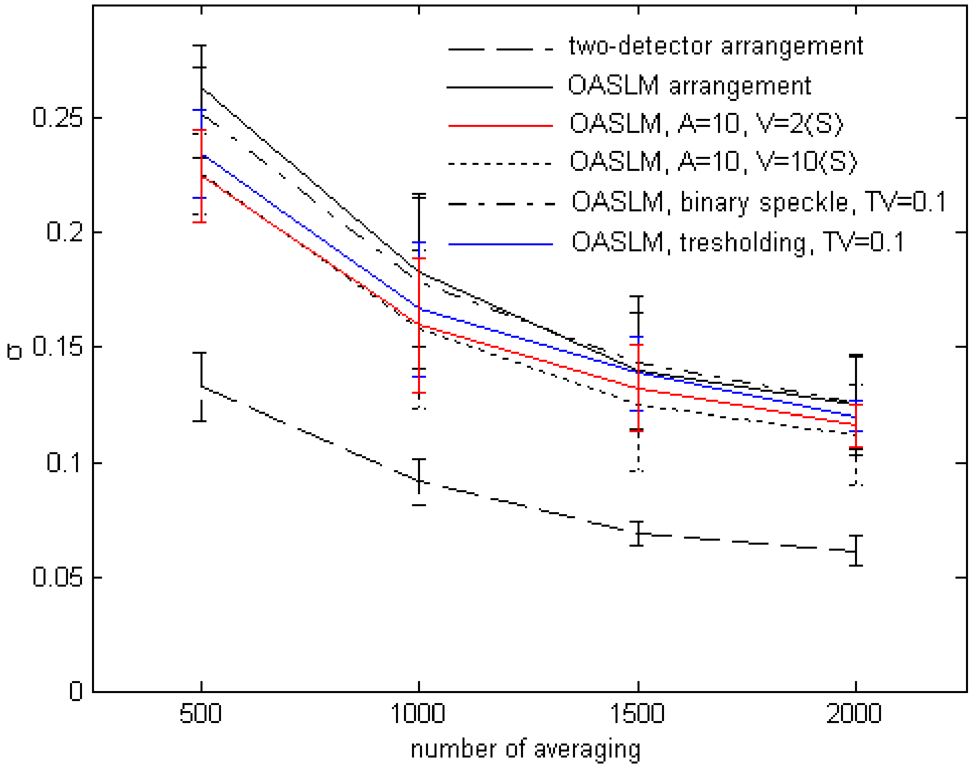

Fig. 7.14. Intensity nonuniformity σ against the number of averaging

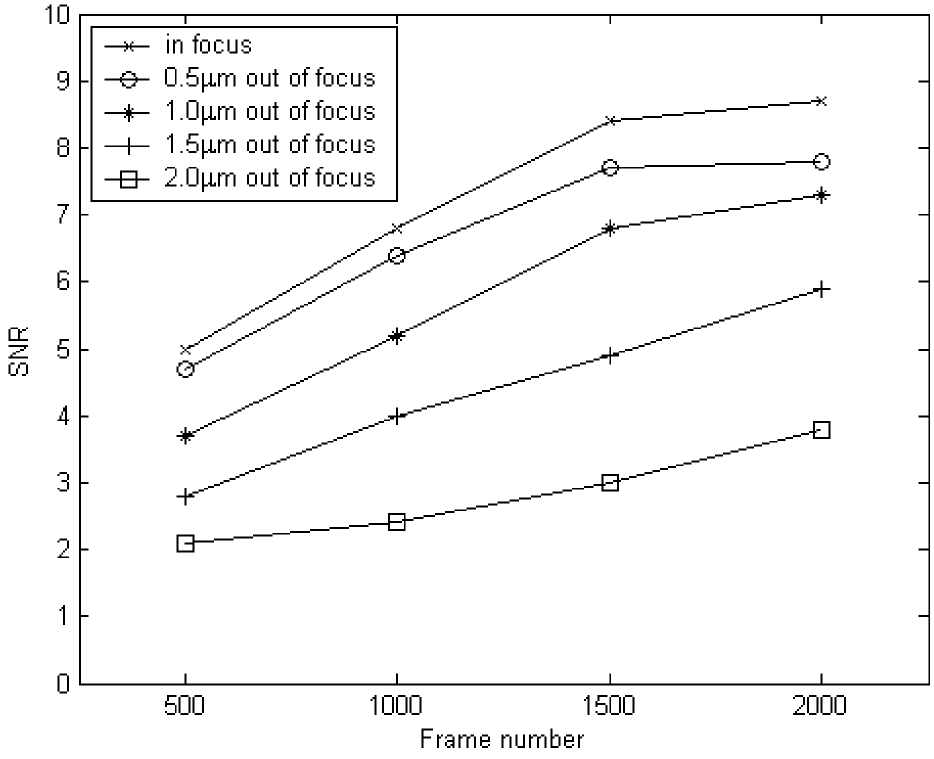

Fig. 7.15. The image signal-to-noise ratio in a SLM-based non-scanning system

7.5 Experimental results with digital frame averaging

Encouraged by the results of the computer simulation presented in Section 7.4, experiments were performed with 4μm fluorescent beads on the bench system shown in Fig. 7.1. The experimental procedure includes two sessions for the specimen at each focal position:

- Record 500 frames of a field of 4μm fluorescent beads with each frame modulated by LCD with a correlated speckle pattern
- Move the LCD horizontally by about 100 μm, record 500 more frames with each frame modulated with an uncorrelated speckle pattern

Measurements were taken for the object at 4 different focal positions. The exposure time for each frame was set to 2 seconds. The recorded frames, stored on a computer, were then processed using Eq. (7.4). An individual random laser speckle pattern reproduced on the LCD is shown in Fig. 7.16. Its intensity distribution with a negative-exponential characteristic is shown in Fig. 7.17. Figs 7.18 – 7.20 show the averaged image modulated by correlated pattern $\langle IS + n \rangle$, the averaged image modulated by uncorrelated pattern $\langle IS' + n \rangle$ and the processed image I_p^3 respectively when the object is in focus. Fig. 7.21 shows the processed image with the negative components suppressed for the object at different focal positions. The experimental results show evident agreement with theory and simulation except for the dark grid pattern imposed due to the opaque mask between the LCD pixels. Another artefact is that the beads in Fig. 7.20 look shadowy due to the fact that there is a small displacement between the two averaged images. A zoom-in view of the bead indicated with arrow in Fig. 7.20 is given in Fig. 7.22. The bead looks deformed as shown in Fig. 7.23 after the negative components are removed. This problem will be discussed later in section 7.6.

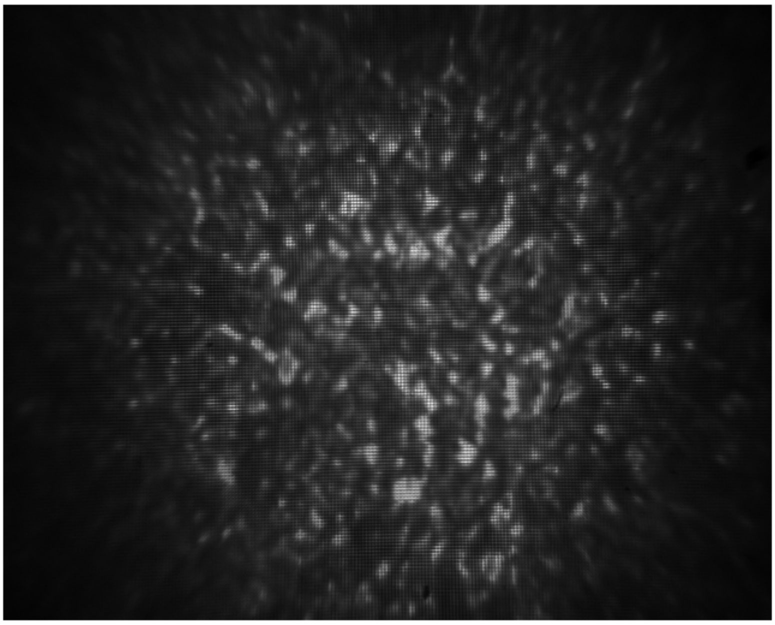

Fig. 7.16. The laser speckle pattern reproduced on the LCD

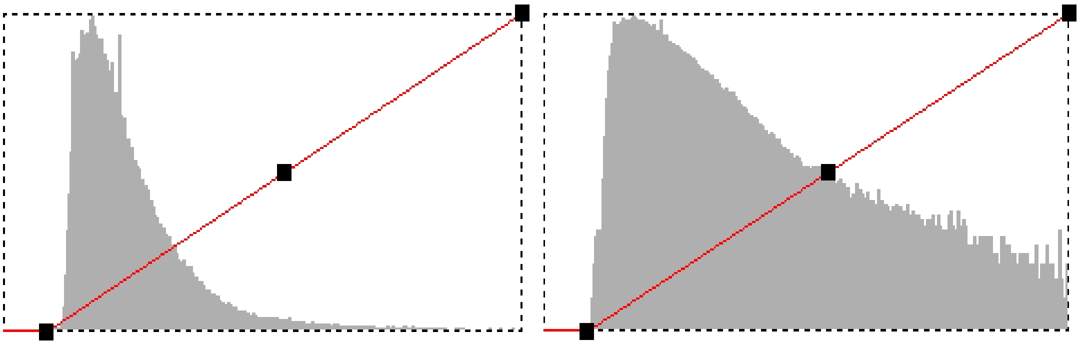

(a) Linear histogram (b) Logarithmic histogram

Fig. 7.17. Histograms of the speckle pattern in Fig. 7

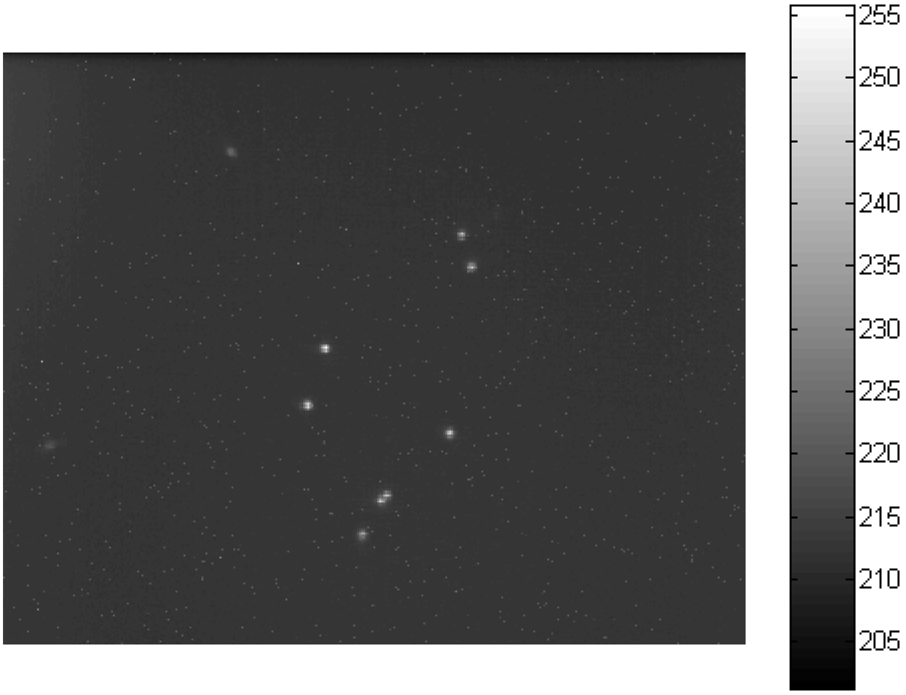

Fig. 7.18. The averaged image modulated by correlated pattern $\langle IS + n \rangle$

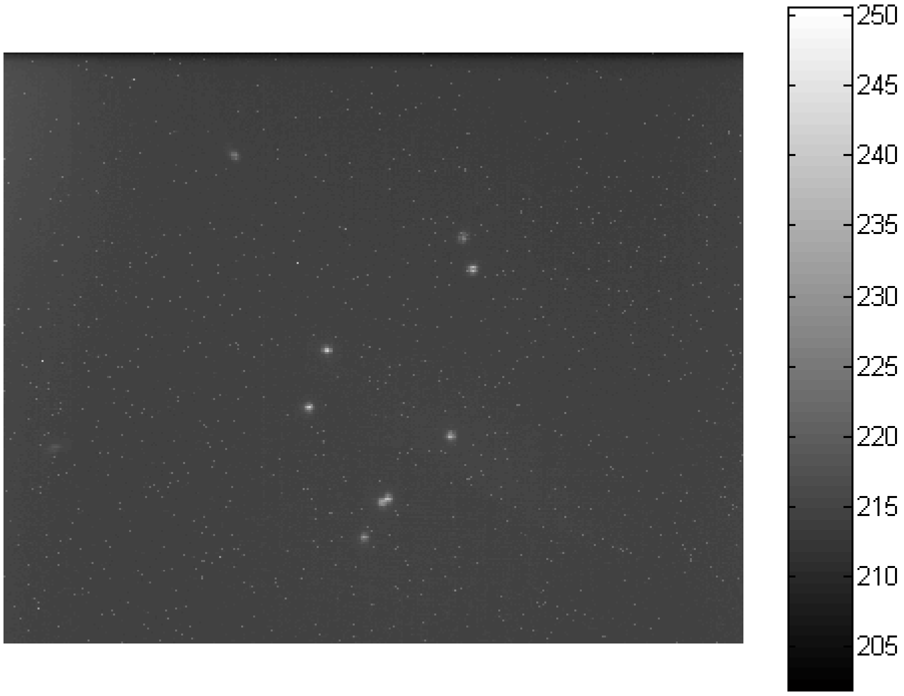

Fig. 7.19. The averaged image modulated by uncorrelated pattern $\langle IS'+n \rangle$

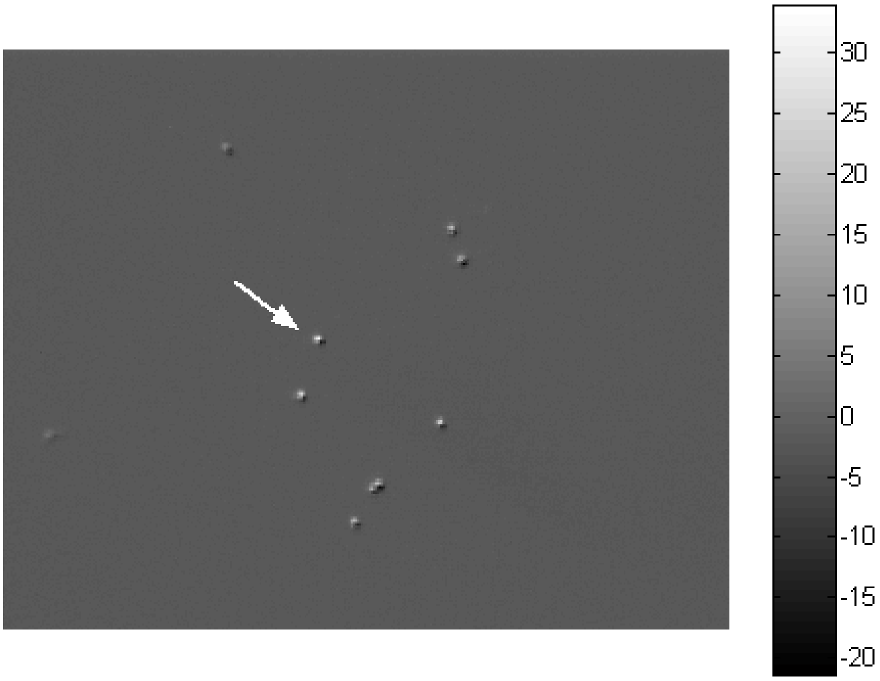

Fig. 7.20. The processed image I_p^3

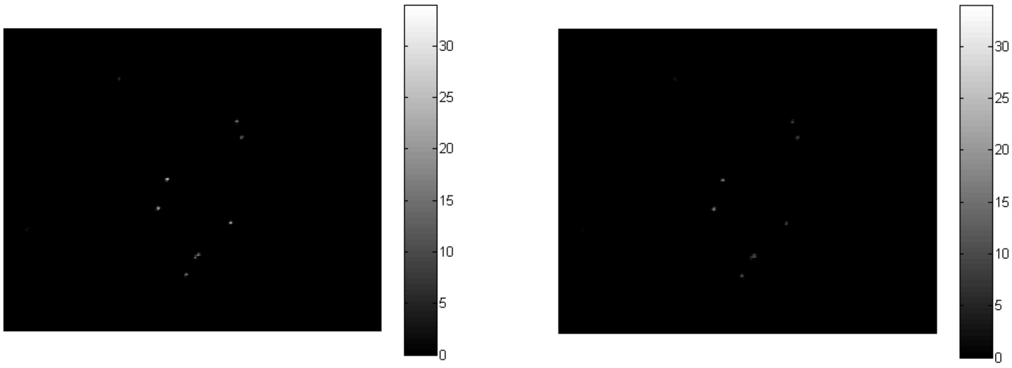

(a) In focus

(b) 20μm out of focus

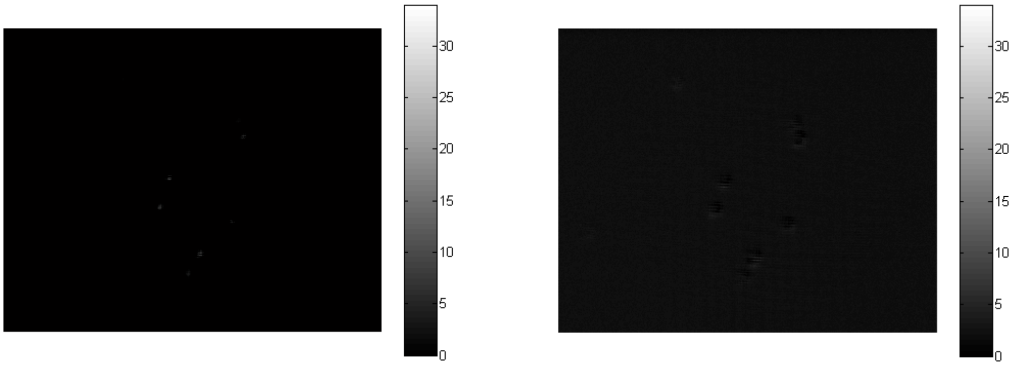

(c) 40μm out of focus

(d) 60μm out of focus

Fig. 7.21. Processed images (640 × 512 × 12) with the negative components suppressed for the object at different focal positions

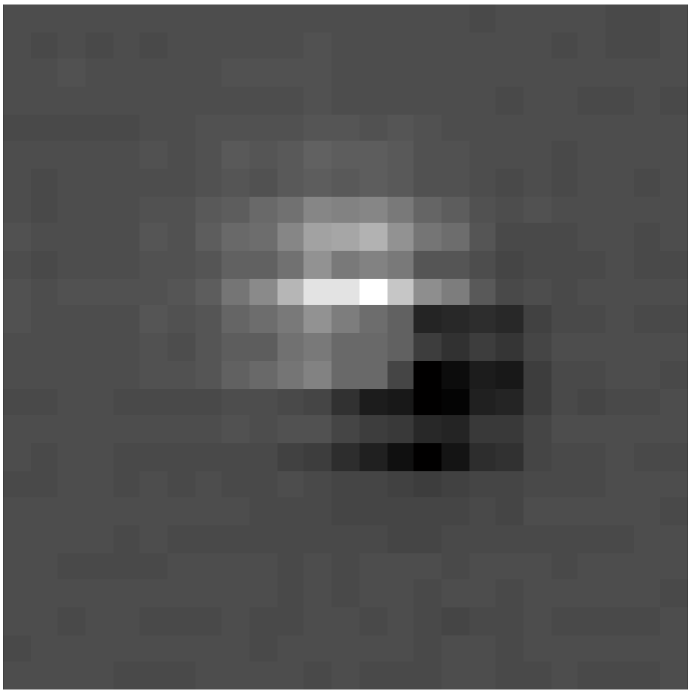

Fig. 7.22. A zoom-in view of the bead indicated with arrow in Fig. 7.20

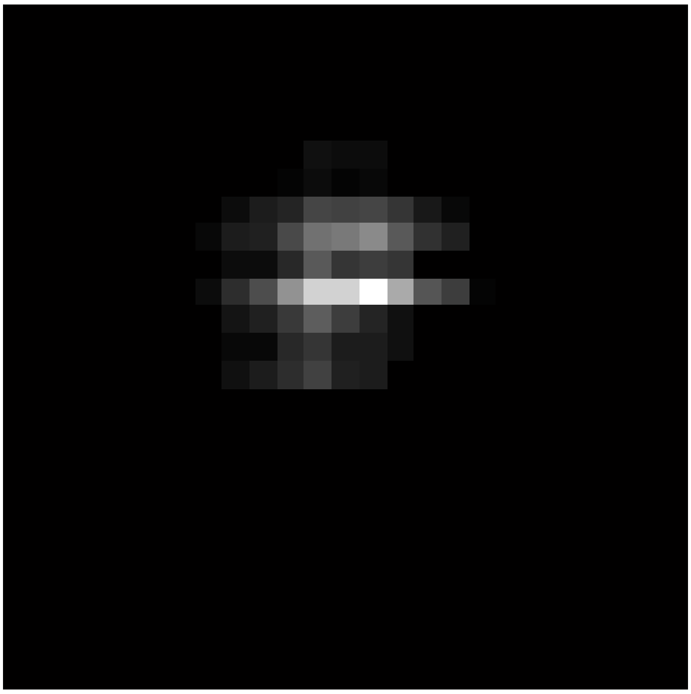

Fig. 7.23. A zoom-in view of the same bead as in Fig. 7.22 after the negative components suppressed

7.6 Image manipulation

As has been pointed out earlier, an artefact in the experimental result is that there is a small displacement of bead location between the two averaged images, and the amount of the displacement is different for the sample at different focal positions. This problem may be caused by the misregistration of the fluorescence frame with the corresponding pixel locations on the LCD panel during the measurement with correlated speckle and by the shifting of the LCD between the two measurements, as this scenario can be easily simulated by computer.

However this problem can be overcome by aligning the two averaged images prior to the subtraction operation. A method for image alignment by cross-correlation is introduced [69]. With this method the mismatch between two similar images can be determined by measuring the peak offset from the origin of their cross-correlation. But it is found that the method works only when no white noises exist in either image, otherwise they cannot be subtracted away. Therefore, the processed image should be expressed as

$$I_p = \langle IS \rangle - \langle IS' \rangle_T \tag{7.8}$$

where $\langle IS' \rangle_T$ denotes the $\langle IS' \rangle$ with a translational movement and it is assumed that the averaged white noise $\langle n \rangle$ has been removed from both images.

To obtain the averaged white noise $\langle n \rangle$, 500 CCD frames were recorded with the laser switched off. The histograms of an individual CCD frame and the averaged frame are shown in Figs. 7.24 and 7.25 respectively. The standard deviation of the averaged white noise has been reduced from 3.3 to 1, which implies that frame averaging, or ensemble averaging, helps to reduce the white noise content. Figs. 7.26 and 7.27 show the images $\langle IS \rangle$ and $\langle IS' \rangle$ respectively where the noise $\langle n \rangle$ has been subtracted. Figs. 7.28 and 7.29 show the subregions of Figs. 7.26 and 7.27 indicated with arrows, from which we see that the bead is laterally displaced by a few pixels.

The cross-correlation c between images f and g can be written as

$$c = f \otimes g \tag{7.9}$$

According to the correlation theorem, Eq. (7.9) in the Fourier space becomes

$$F\{c\} = F^*\{f\}F\{g\} \tag{7.10}$$

where $F^*\{f\}$ is the complex conjugate of $F\{f\}$. So we can easily obtain the cross-correlation by taking the inverse Fourier transform of Eq. (7.10):

$$c = F^{-1}\{F^*\{f\}F\{g\}\} \tag{7.11}$$

The calculated cross-correlation between the two subregions is shown in Fig. 7.30. The maximum of the cross-correlation is found at x=16, y=15, with an x-offset of 3 pixels and a y-offset of 2 pixels from the origin (x=13, y=13). This means that $\langle IS' \rangle_T$ can be obtained by shifting image $\langle IS' \rangle$ 3 pixels upwards and 2 pixels to the left. But, due to the pixelated structure of the LCD, the image intensities of the bead in the subregions are not smoothly distributed, nor is their cross-correlation. Therefore the assessed peak offset can be inaccurate. To avoid this problem, the calculated cross-correlation needs to be smoothed prior to peak offset assessment. The smoothed cross-correlation with a Gaussian kernel [70] is shown in Fig. 7.31. Locations of the maxima of cross-correlation, smoothed cross-correlation and the assessed movement for image $\langle IS' \rangle$ for the object at different focal positions are listed in Table 7.3.

The processed image for the object in focus obtained using Eq. (7.8) is shown in Fig. 7.32, which does not look shadowy compared with Fig. 7.22. The images for the specimen at different focal positions manipulated in the same way with negative components suppressed are shown in Fig. 7.33. A zoom-in view of the bead indicated with arrow in Fig. 7.20 is given in Fig. 7.34. The bead reproduced by removing the negative components is shown in Fig. 7.35 where no shape deformation can be observed except the dark grid pattern imposed due to the pixelated structure of the LCD. A zoom-in view of beads at different focal positions, corresponding to Fig. 7.33, is shown in Fig. 7.36 where a depth discrimination property is clearly displayed.

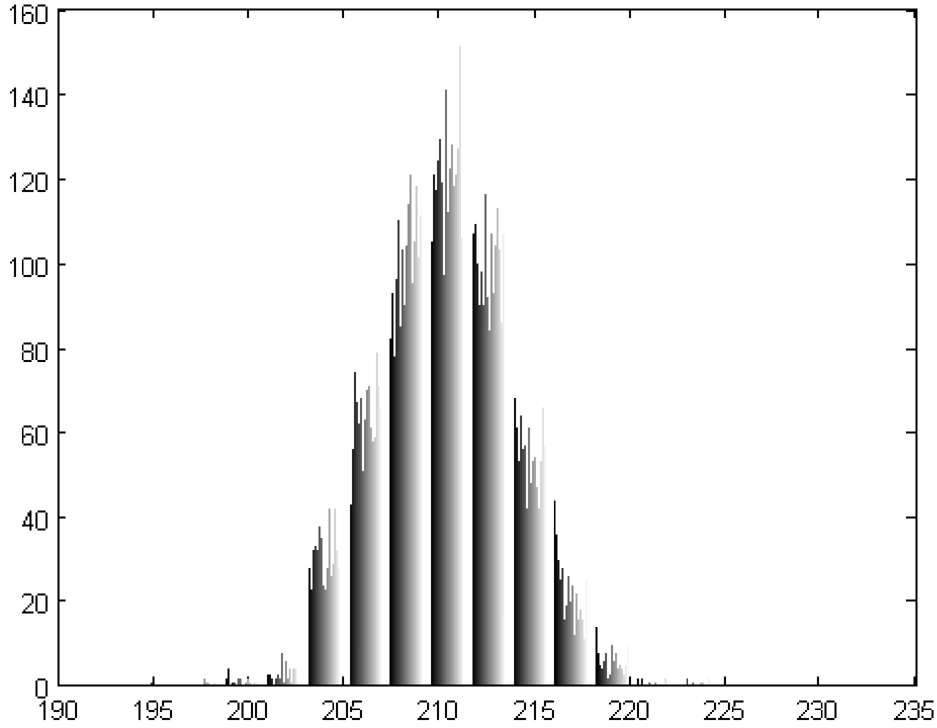

Fig. 7.24. The histogram of an individual CCD frame
with a mean of 210 and SD of 3.3

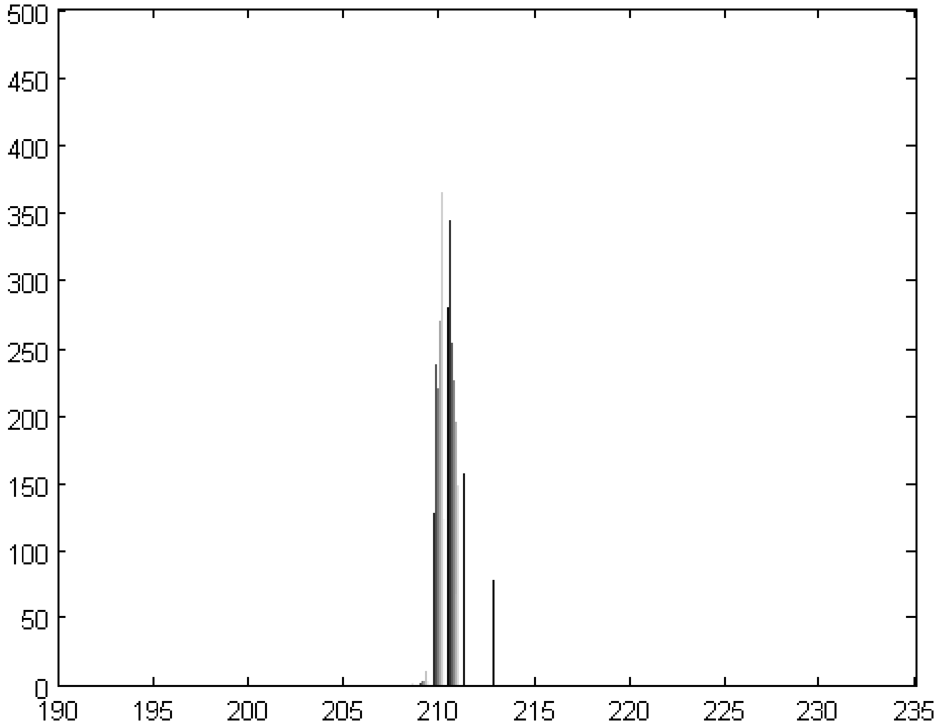

Fig. 7.25. The histogram of the averaged frame
with a mean of 210 and SD of 1

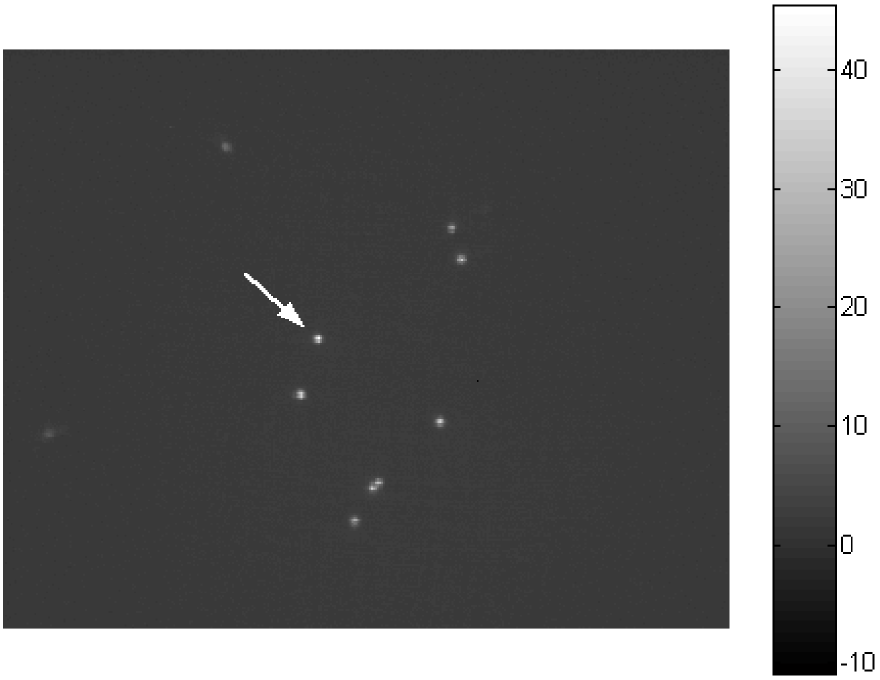

Fig. 7.26. The image $\langle IS \rangle$ with $\langle n \rangle$ removed

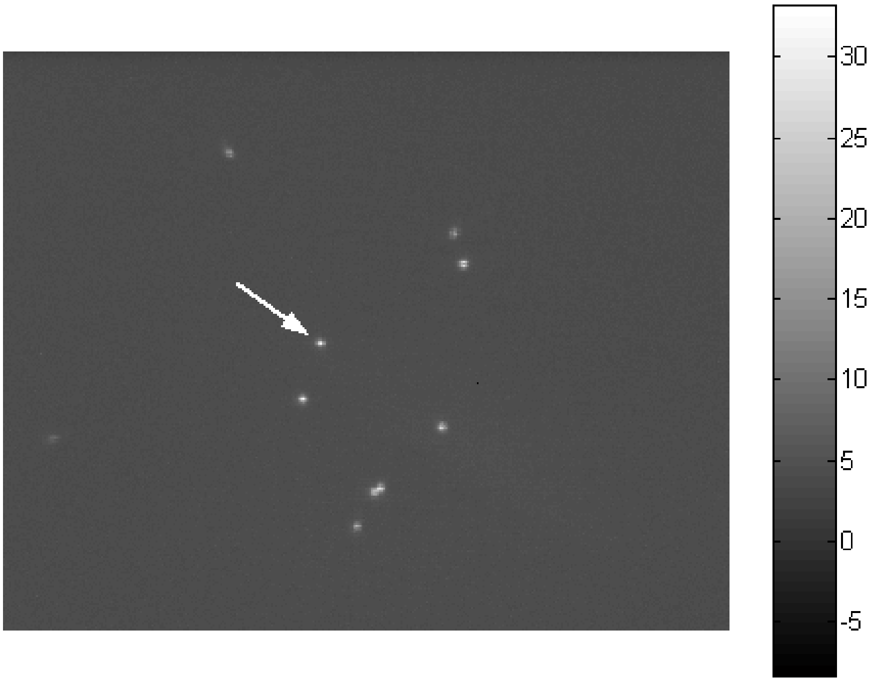

Fig. 7.27. The image $\langle IS' \rangle$ with $\langle n \rangle$ removed

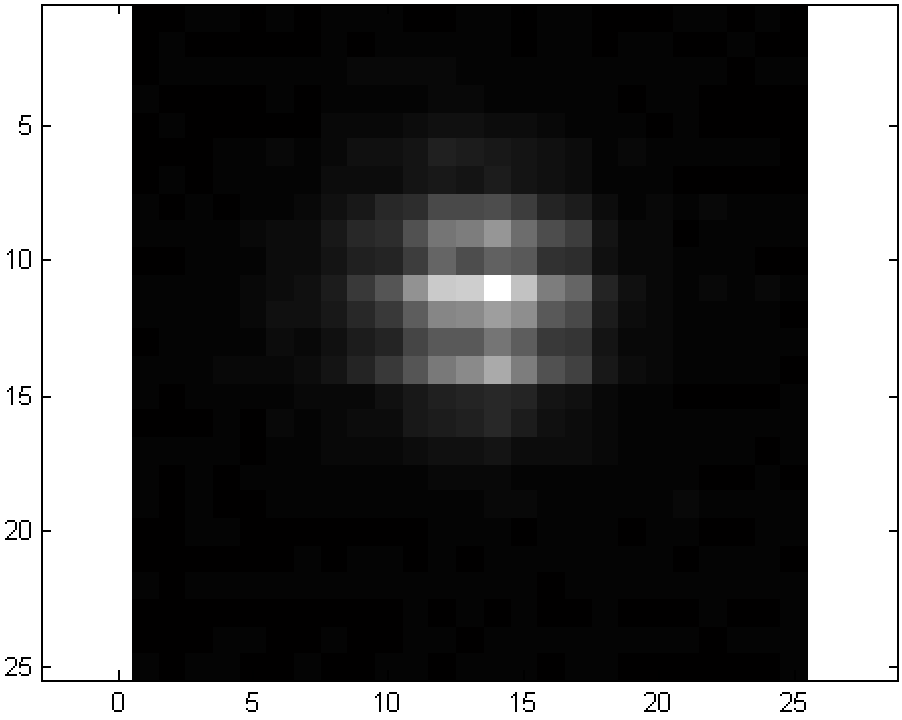

Fig. 7.28. The subregion of Fig. 7.26

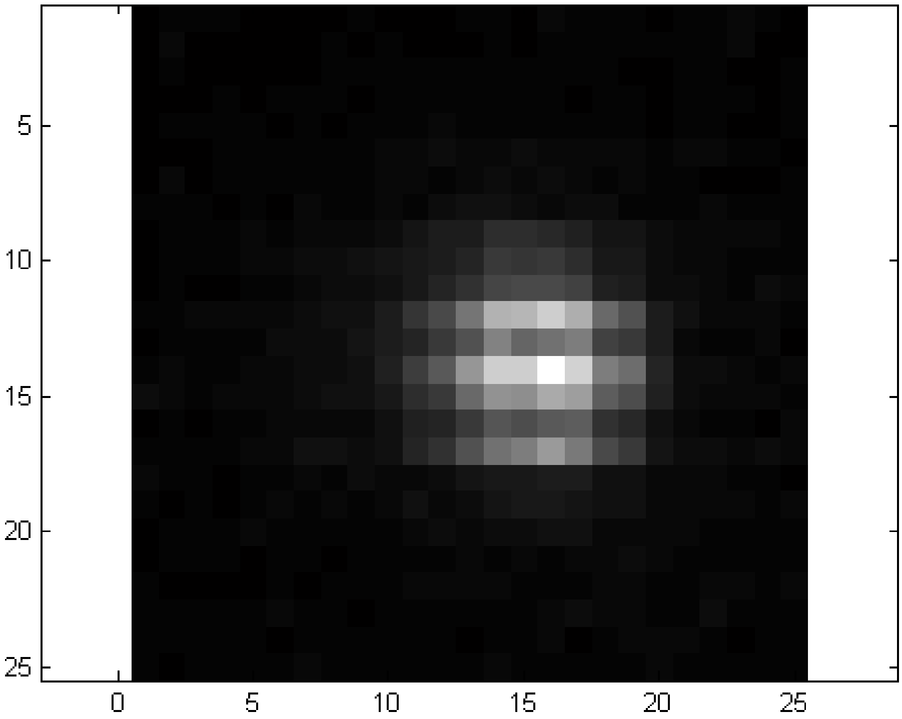

Fig. 7.29. The subregion of Fig. 7.27

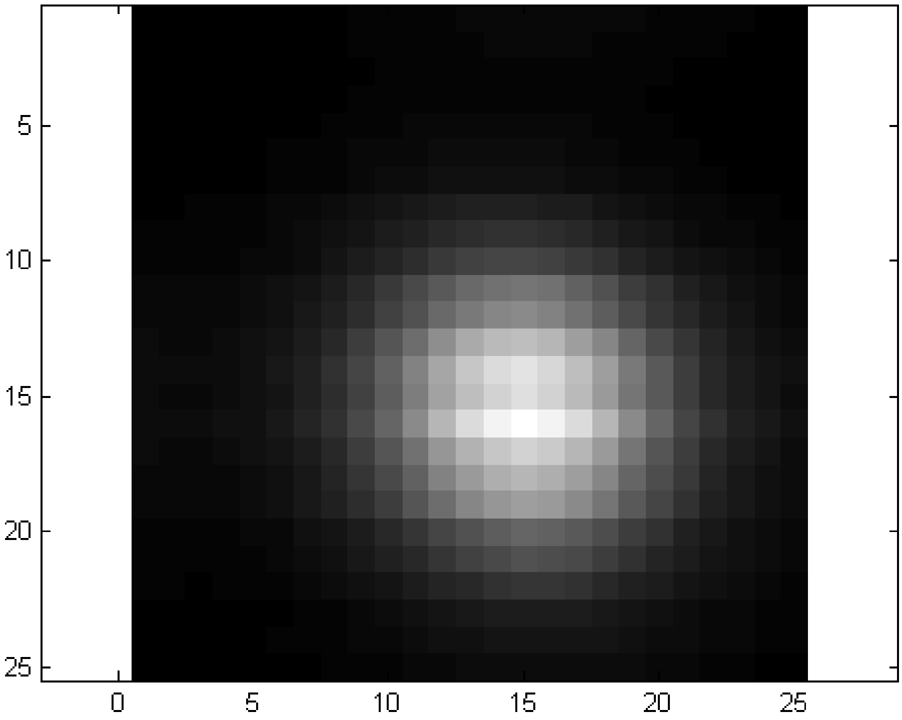

Fig. 7.30. The cross-correlation between the two subregions

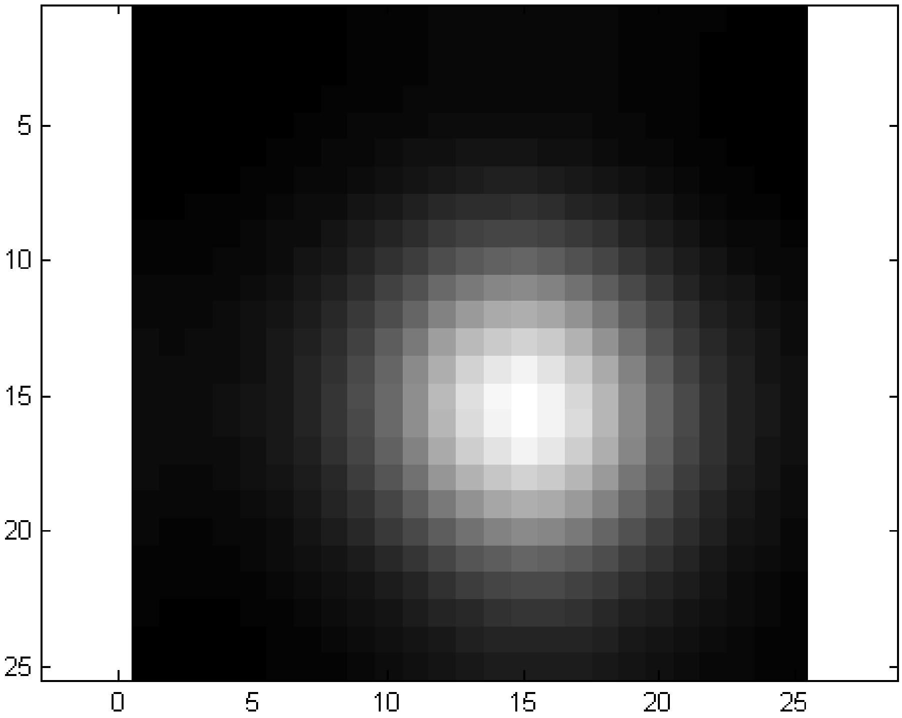

Fig. 7.31. Smoothed cross-correlation

Focal position of the sample (μm)	Centre of cross-correlation	Location of maximum of cross-correlation	Location of maximum of smoothed cross-correlation	Assessed movement
0	x=13 y=13	x=16 y=15	x=15 y=15	2 pixels upwards 2 pixels to the left
20	x=13 y=13	x=13 y=14	x=14 y=14	1 pixel upwards 1 pixel to the left
40	x=13 y=13	x=13 y=13	x=13 y=13	No movement needed
60	x=18 y=18	x=14 y=19	x=14 y=19	4 pixels downwards 1 pixel to the left

Table 7.3 Assessment for image alignment

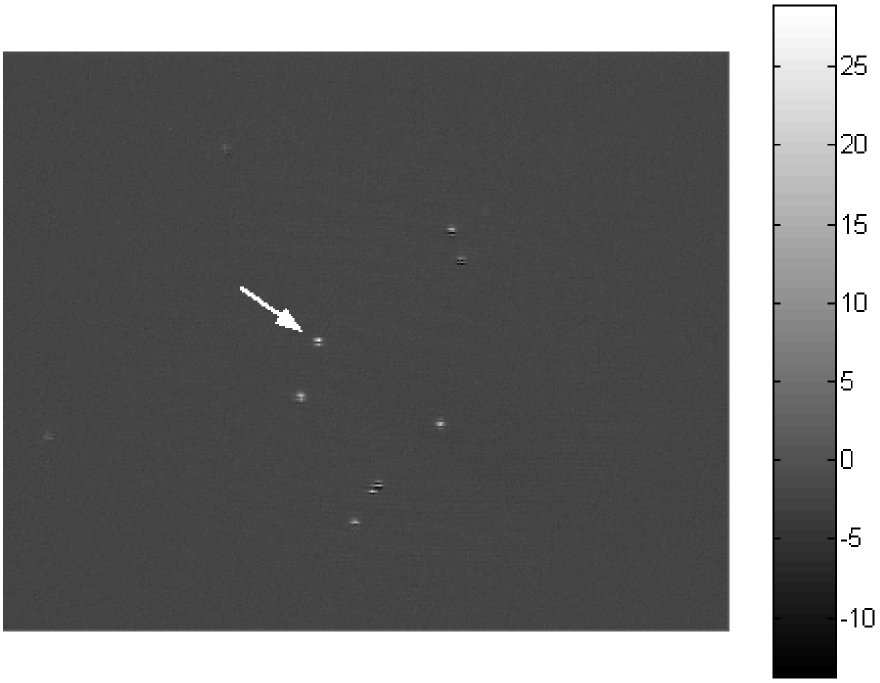

Fig. 7.32. The processed image I_p for the in-focus case with the image $\langle IS' \rangle$ shifted to the left by 2 pixels and then 2 pixels upwards

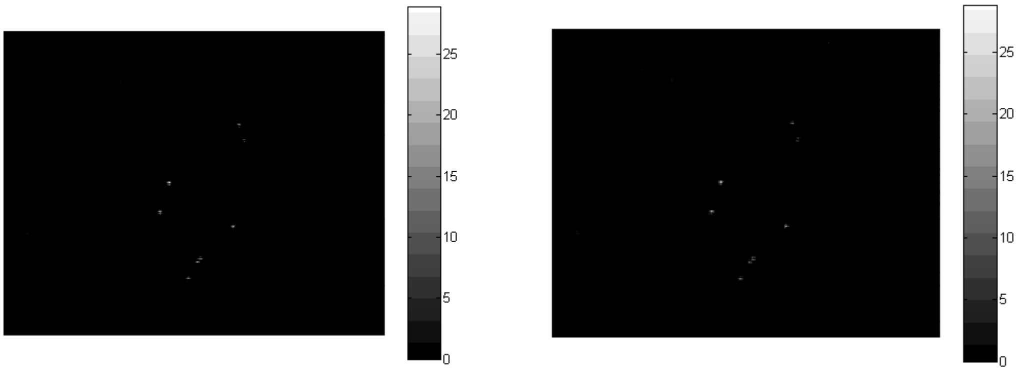

(a) in focus

(b) 20μm out of focus

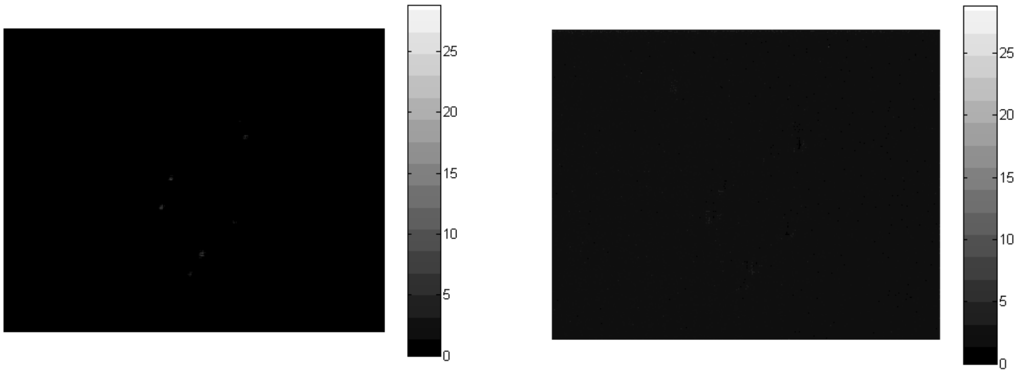

(c) 40μm out of focus

(d) 60μm out of focus

Fig. 7.33. The processed image I_p with the negative components suppressed

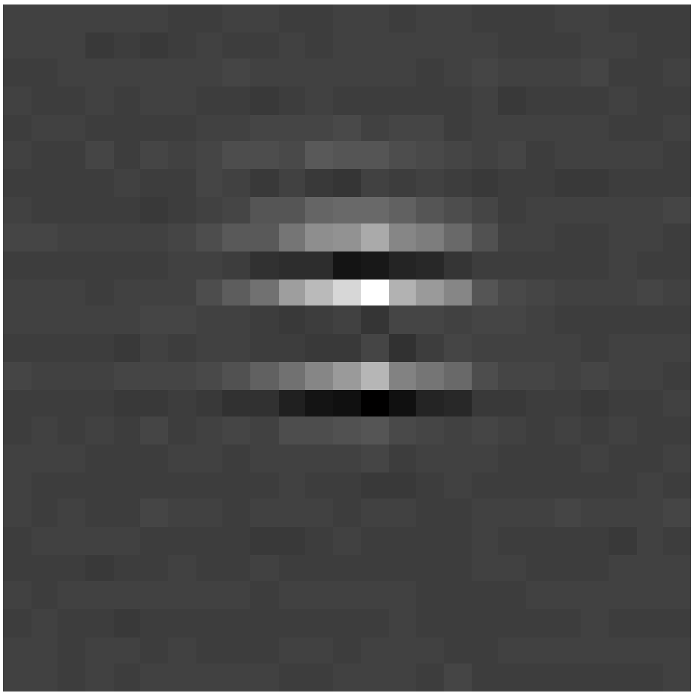

Fig. 7.34. A zoom-in view of the bead indicated with arrow in Fig. 7.32

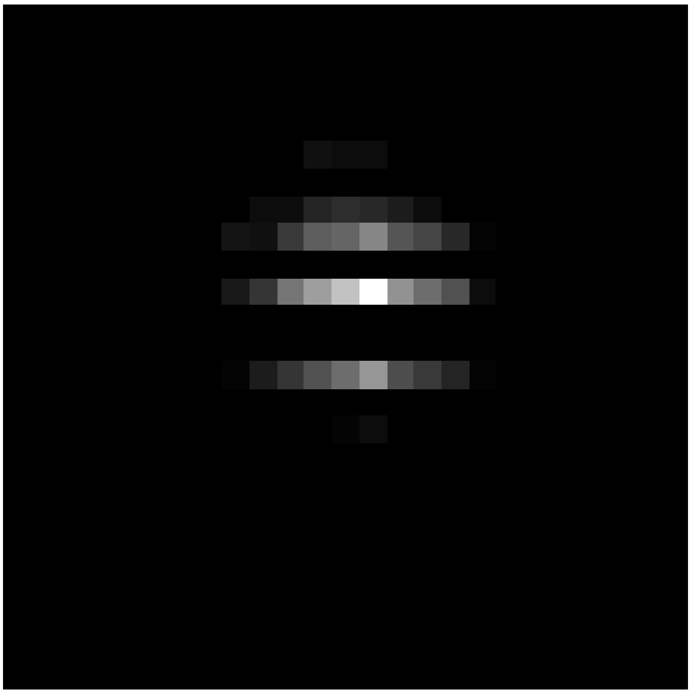

Fig. 7.35. A zoom-in view of the same bead as in Fig. 7.34 after the negative components suppressed

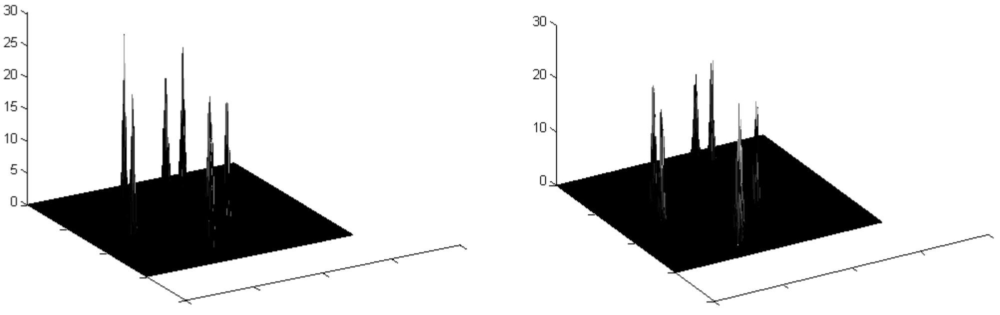

(a) In focus (b) 20 μm out of focus

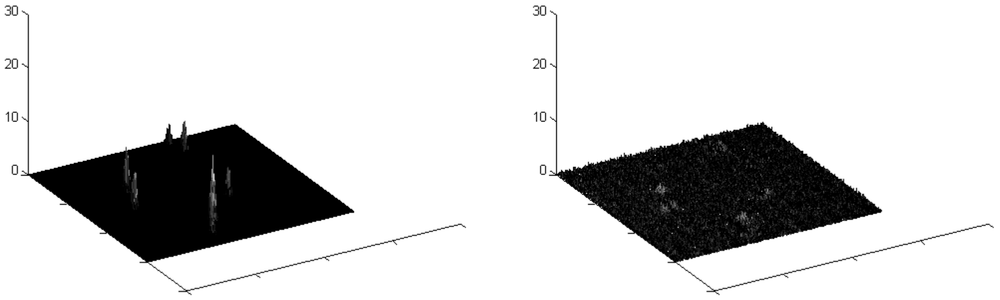

(c) 40 μm out of focus (d) 60 μm out of focus

Fig. 7.36. A zoom-in view of beads at different focal positions

7.7 Experimental results with averaging by CCD charge accumulation

An experiment based on frame averaging by CCD charge accumulation or the two-shot scheme was also conducted. Considering the low frame rate of the LCD, we set the stepper motor speed to 150 steps/sec. The exposure time of the cooled CCD camera was set to 10 seconds, during which time the diffuser rotates by 1.5°. The speed of the speckle patterns moving vertically on the LCD panel was calculated to be 2.6 mm/sec. The LCD was shifted *vertically* by 100 microns between the two CCD readouts, because the speckle patterns change by far slower in the horizontal direction than in the vertical direction, and a horizontal shift will not make significant difference between the two measurements. The averaged frames and the processed image are shown in Figs. 7.37. The images of the beads at focal positions of 0μm, 20μm, 40μm and 60μm with and without image manipulation are shown in Figs 7.38. A frame with the laser switched off is also recorded to obtain an image of white noise for image manipulation. The processed images with the negative components suppressed are shown in Fig. 7.39. A corresponding zoom-in view of beads at different focal positions is shown in Fig.7.40 where a depth discrimination property is clearly displayed. Compared with the experimental results with digital frame averaging shown in Fig. 7.36, the averaging scheme by CCD charge accumulation gives a very similar result but requires capturing only two frames so that the data collection time can be reduced dramatically.

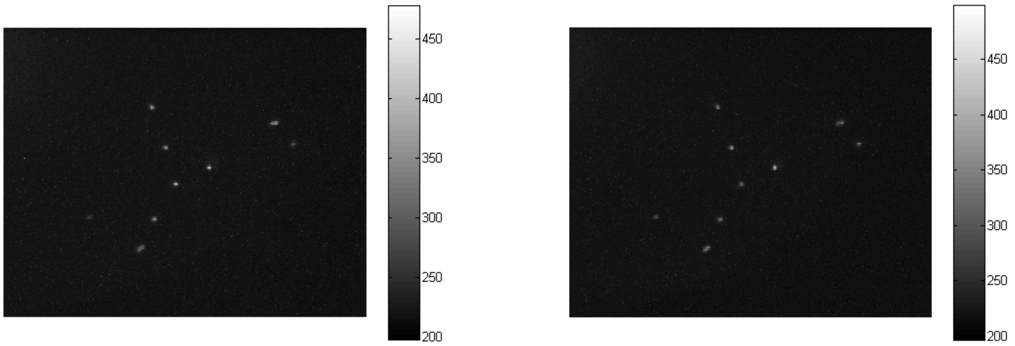

(a) In focus (e) In focus

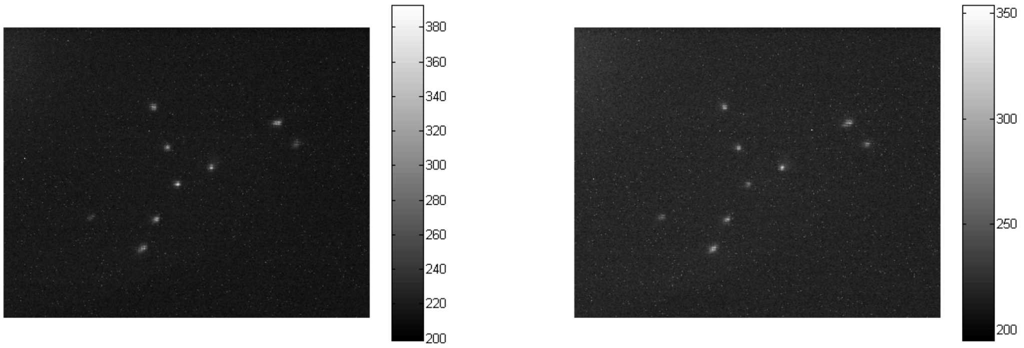

(b) 20 μm out of focus (f) 20 μm out of focus

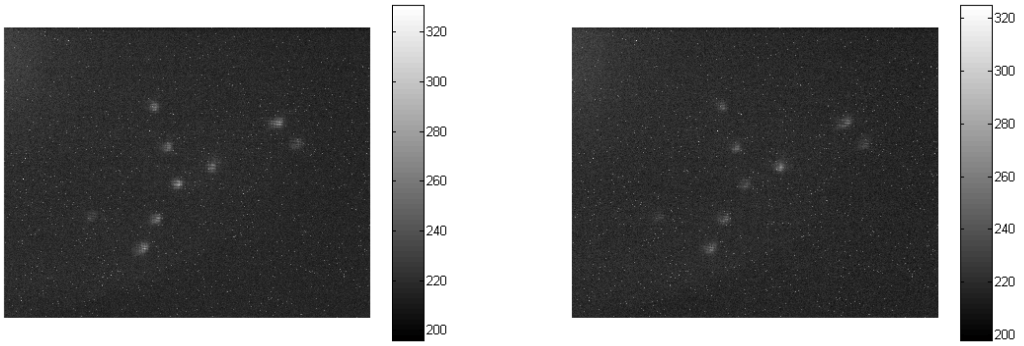

(c) 40 μm out of focus (g) 40 μm out of focus

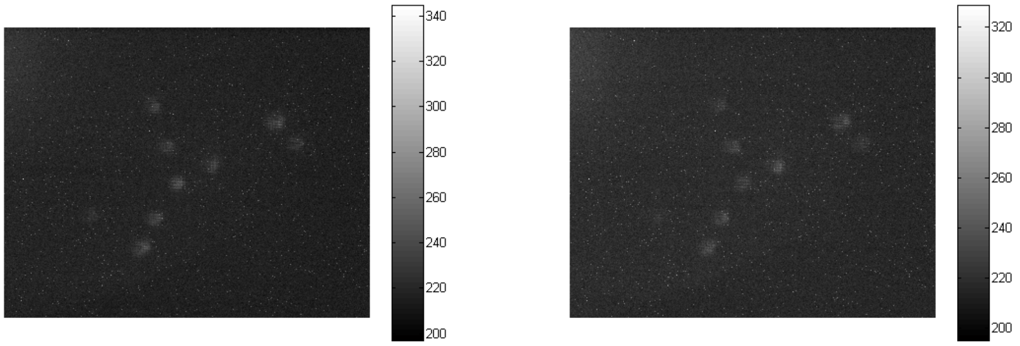

(d) 60 μm out of focus (h) 60 μm out of focus

Fig. 7.37. The images averaged by CCD charge accumulation

(a)-(d): $\langle IS + n\rangle$, (e)-(h): $\langle IS'+n\rangle$

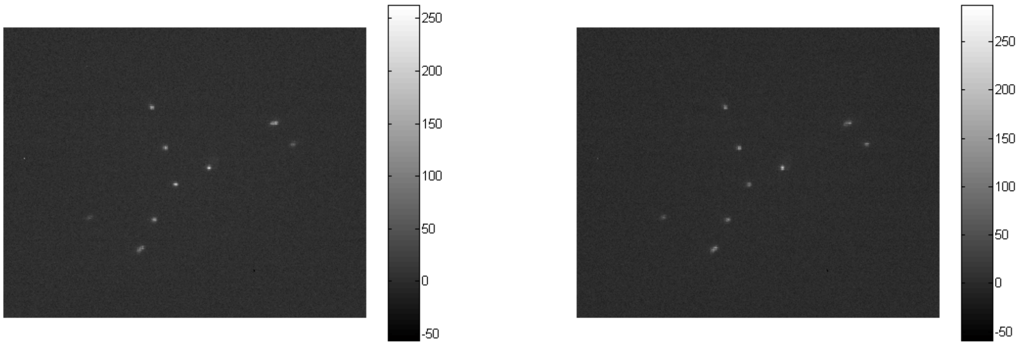

(a) In focus

(e) In focus, 1 pixel down

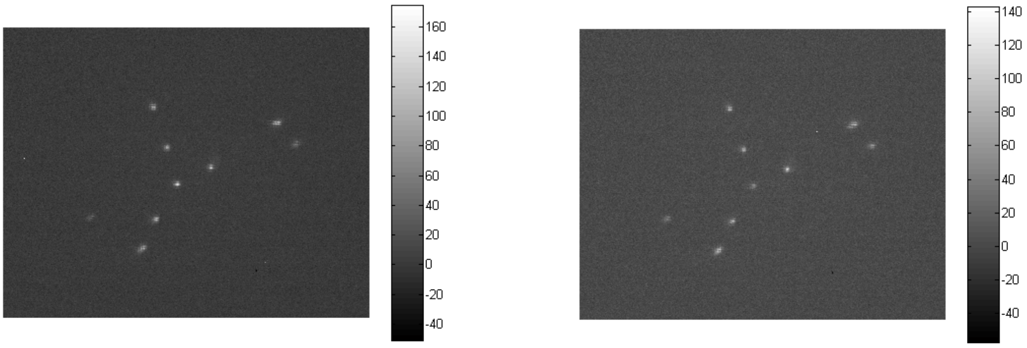

(b) 20 μm out of focus

(f) 20 μm out of focus, 1 pixel up

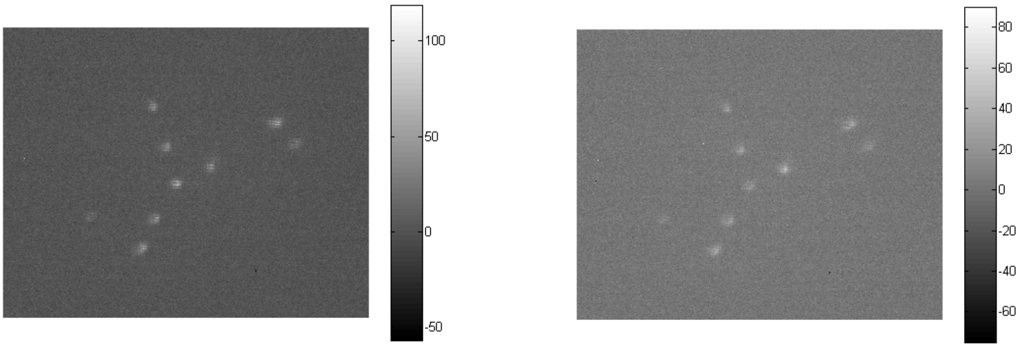

(c) 40 μm out of focus

(g) 40 μm out of focus, 1 pixel up

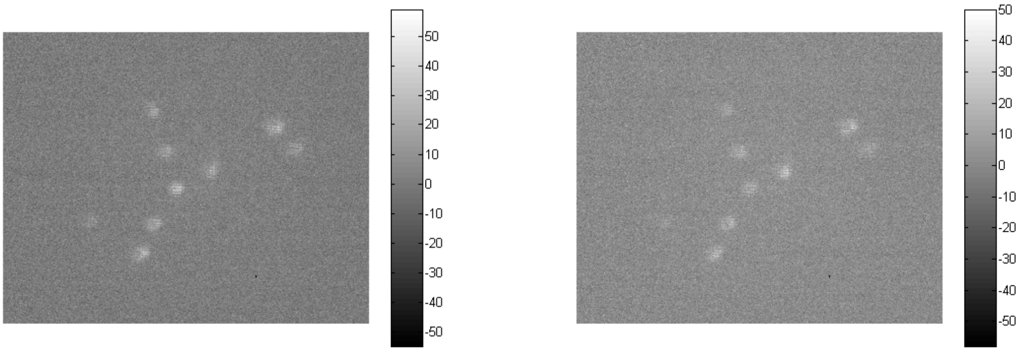

(d) 60 μm out of focus

(h) 20 μm out of focus, 1 pixel up

Fig. 7.38. The processed images
(a)-(d): without image manipulation, (e)-(h): with image manipulation

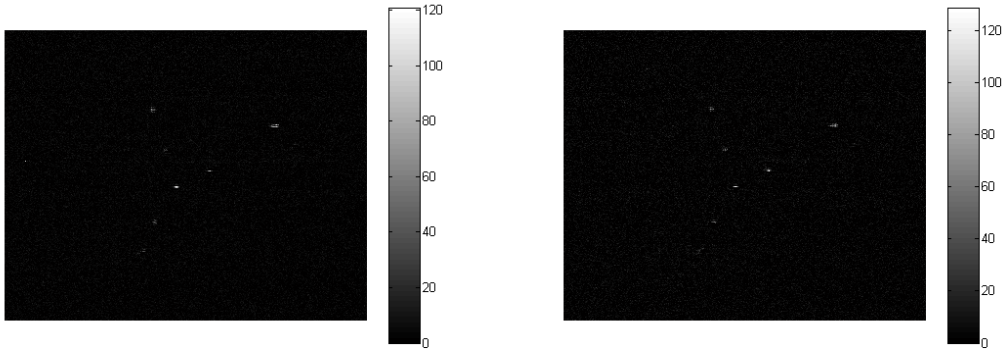

(a) In focus (e) In focus, 1 pixel down

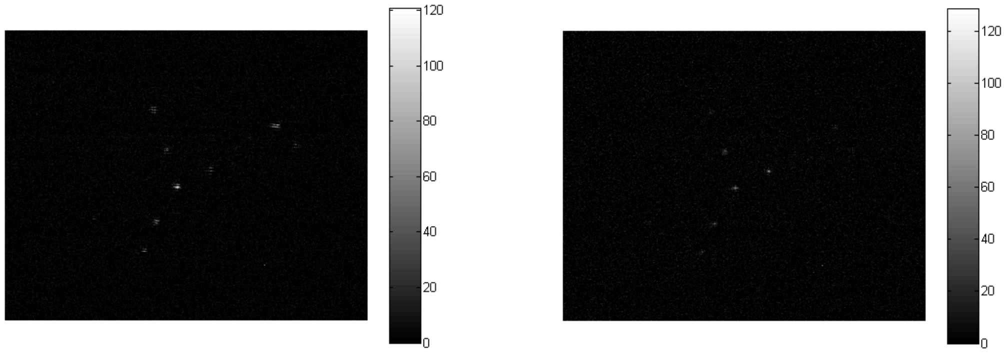

(b) 20 μm out of focus (f) 20 μm out of focus, 1 pixel up

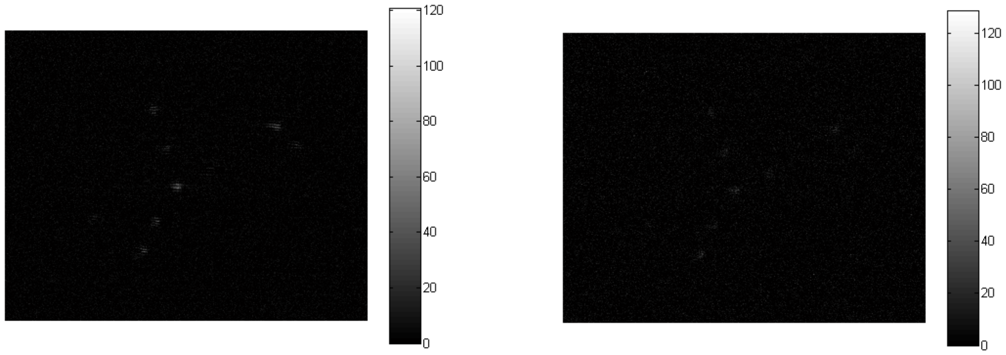

(c) 40 μm out of focus (g) 40 μm out of focus, 1 pixel up

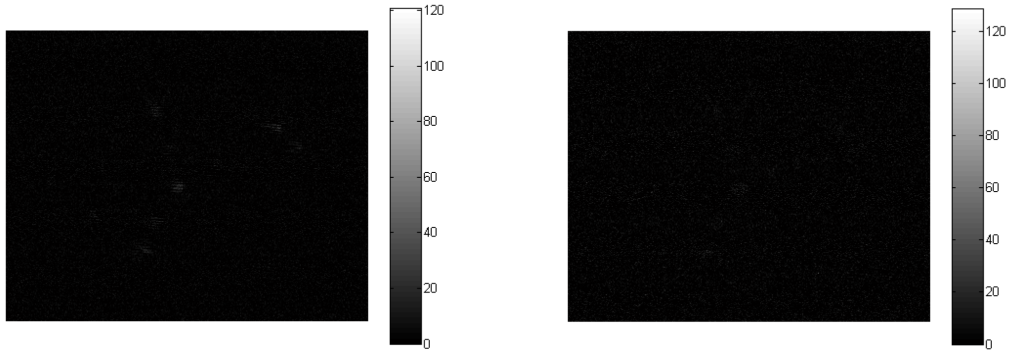

(d) 60 μm out of focus (h) 60 μm out of focus, 1 pixel up

Fig. 7.39. The processed image with the negative components suppressed (a)-(d): without image manipulation, (e)-(h): with image manipulation

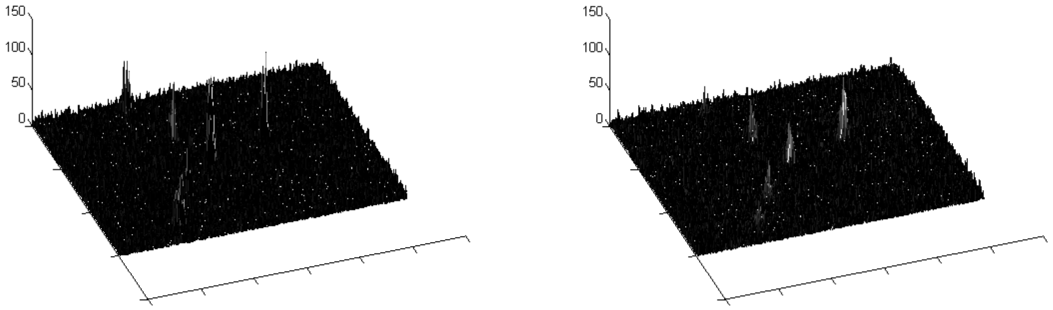

(a) in focus (b) 20 μm out of focus

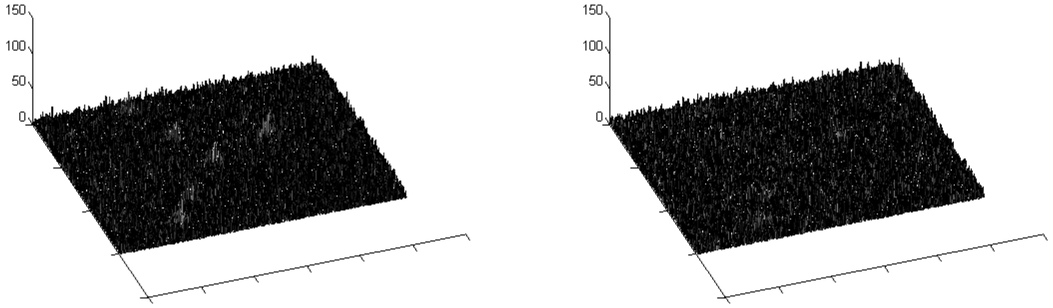

(c) 40 μm out of focus (d) 60 μm out of focus

Fig. 7.40. A zoom-in view of beads at different focal positions

8. Conclusion and further work

> “*The three things that are most essential to achievement are common sense, hard work and stick-to-it-iv-ness.....*”
>
> — Thomas Edison, 1847 – 1931

Fluorescence microscopy is the commonest approach for studying molecular organisations and tissue structures. For anyone new to this area, however, it can be difficult to decide which techniques or equipment to try: wide-field microscopy, scanning confocal, or spinning disk confocal? When selecting which system to use for imaging a sample, one should consider a few things: What spatial resolution is required? Is the process to be observed fast or slow? Is the sample thick or thin? You also need to consider some further questions: Is the sample subject to photobleaching? What is the appropriate illumination intensity to avoid sample damage? In many cases, no single microscope system will be best, and compromises will have to be made. A strong demand of biologists for imaging their different samples resulted in developments of new imaging techniques such as structured-light illumination, 4Pi confocal microscopy, two-photon excitation microscopy, to name just a few. Speckle-illuminated non-scanning fluorescence confocal microscopy, is a novel method for obtaining images with the enhanced resolution and optical sectioning properties of a confocal microscope but avoids the complexity of a scanning system and potentially may avoid the long frame times associated with the scanning process. This method has been investigated by experiment and computer simulations, and the implementation of this method based on two different optical arrangements is presented in this thesis. This chapter will summarize the conclusions from the results that has been achieved and provide some recommendations for future work.

8.1 Conclusion

A non-scanning fluorescence confocal microscopy using speckle illumination is described. It uses a random time-varying speckle pattern to illuminate the specimen, recording a large number of wide-field fluorescence frames I and a sequence of corresponding illumination speckle patterns S with a CCD camera. The recorded frames are then processed by the averaging formula $I_p = \langle I \cdot S \rangle - \langle I \rangle \cdot \langle S \rangle$. The processed image I_p would be equivalent to a confocal image if an infinitive ensemble of frames were used.

The method can be implemented in two optical arrangements. The first one is known as two-detector arrangement where each fluorescence frame is recorded with one CCD camera and the corresponding illumination speckle pattern with the other one at the same time. The recorded frames are stored on a computer for off-line digital processing. As current CCD technology allows a continuous frame rate of hundreds of frames per second (e.g., the Hamamatsu C7770 with a frame rate of 291 per second) and the non-scanning data processing needs to average over hundreds of frames, such a system gives an overall frame rate of the order of a second which is comparable with scanning systems. The second arrangement allows real-time optical data processing instead of digital off-line processing based on the spatial light modulator (SLM) technology. If the SLM is fast enough, frame averaging can be implemented by integrating the signal on the CCD chip in analogue form during a single exposure. In this implementation, only two CCD frames are required, with both of them modulated by dynamic speckle patterns; one by correlated speckle and the other by uncorrelated speckle. The difference of the two frames gives a confocal image. Developments in novel SLM structures, such as digital micromirror device (DMD) [71, 72] and multiple quantum well (MQW) SLMs [73], have led to devices with array sizes exceeding 256×256 and frame rates of 10 ~ 100 KHz. Fast scanless confocal imaging on the sub-second scale should be possible.

The effects of some important factors such as shot noise, Gaussian white noise and quantisation error from a CCD detector on the non-scanning system were investigated by simulation. The image signal-to-noise ratio for a multipoint object was calculated using Murray's procedure. It is shown that the in-focus image SNR of the two-detector arrangement is between 30–70 for the frame number between 500–2000, while the SLM based digital-averaging arrangement gives a SNR between 5-9. For quantitative performance evaluation, several criteria were established in terms of intensity non-uniformity, intensity non-linearity, depth discrimination property and lateral resolution. The simulated behaviour of system was investigated against these criteria. It is shown that the non-scanning system offers the same imaging response as a scanning confocal system in the sense of depth discrimination property and improved lateral resolution, except for a 10% image intensity variation with the two-detector system and 20% with the SLM based system.

To reduce the number of frames required, some methods such as A-Law compression and binary speckle were introduced to improve the efficiency of the averaging process. The simulation results show that these methods can effectively reduce the frame number by 50% for the two-detector system and 15% for the SLM based system without any adverse effects on the performance assessed against the same criteria.

Confocal imaging of 4μm fluorescent microspheres without a raster scan has been realised on a self-built optical bench system. Since there is only one digital

CCD camera available, the two-detector experiment is implemented by using a stepper motor and recording the fluorescent frames and the speckle frames separately. The experimental results agree with simulation very well. It is shown that the non-scanning system offers satisfactory image quality and good background rejection. The SLM based experimental system uses a CCD camera in combination with a transmissive LCD to operate as a OASLM. Frame averaging is performed in two ways: digital frame averaging and analogue averaging by CCD charge accumulation. Because of the low frame rate of the LCD used, analogue averaging is accomplished by using slow time-varying speckle patterns and prolonged CCD exposure time. The results obtained with the two averaging methods are very similar and both show clear confocal properties. Since the SLM based system performs data processing all-optically, the data collection time can be significantly reduced.

No matter which system is used, an important point that needs attention is that the fluorescent frame and the corresponding speckle pattern must be correctly registered with the CCD pixels, otherwise there would be a mismatch between the two frames and the resulting image would show a shadow effect. However it has been shown that this mismatch can be corrected automatically by calculating the cross-correlation of the two frames.

In a few words, speckle-illuminated fluorescence microscopy offers several advantages compared to the established scanning and non-scanning methods:

1. The same axial and lateral spatial resolution as the CSM
2. No need for a scanning apparatus
3. No need for a pinhole
4. Since the method is truly wide-field, it is less susceptible to photobleaching because the light is not focused and the excitation density is much smaller [74]

5. The two-detector arrangement equipped with ordinary video CCD cameras has an extremely simple structure. It can be used in place of conventional CSMs when imaging speed is not essential

The principal disadvantages of this method compared to others is that

1. The illumination efficiency is low, about 15%, due to the use of the diffuser
2. There is a 10 – 20% unwanted variation in intensity levels
3. Not suitable for two-photon excitation

8.2 Further work

There is clearly a great deal of work yet to be done in order to develop a sophisticated instrument on the basis of progress made to date. The issues to be addressed include:

Current experiments are restricted to low-aperture case. It would be useful and interesting to model high-aperture non-scanning confocal imaging using vector theory which is outlined in section 2.12. Experiments could be made with high NA objectives and standard submicron fluorescent beads.

It would be worthwhile to investigate other methods, such as sigmoid or tanh function, for speckle processing.

As mentioned in section 6.2.5, there are two types of speckle motion from a rotating diffuser: translation and boiling. The current simulation is restricted to the boiling type. However the true case in a SLM based system is the translation type. It would be useful if such a speckle motion could be modelled.

Whether a fast spatial light modulator is available will be crucial to the survival of our research on fast confocal imaging with the SLM based system. Recent literature survey shows that digital micromirror device (DMD) might be feasible for our application. The DMD technology was perfected and commercialised over the last decade. One of the advantages of DMD is that it can modulate light independently of wavelength due to its simple reflective operation. The DMD has a light modulator efficiency in the range of 65%. Binary frame rates up to 9,700 frames /second can be achieved for full array (1024x768) operation. LCDs are also widely used SLMs and may be either transmissive or reflective, but do not have the speed, precision or broadband capability that the DMD boasts. Commercial MQW SLMs working at visible bands are still not available. A possible implementation of two-shot scanless confocal microscopy using speckle illumination and the DMD for optical data processing is illustrated in Fig. 8.1. One can expect a new optical imaging technique to emerge!

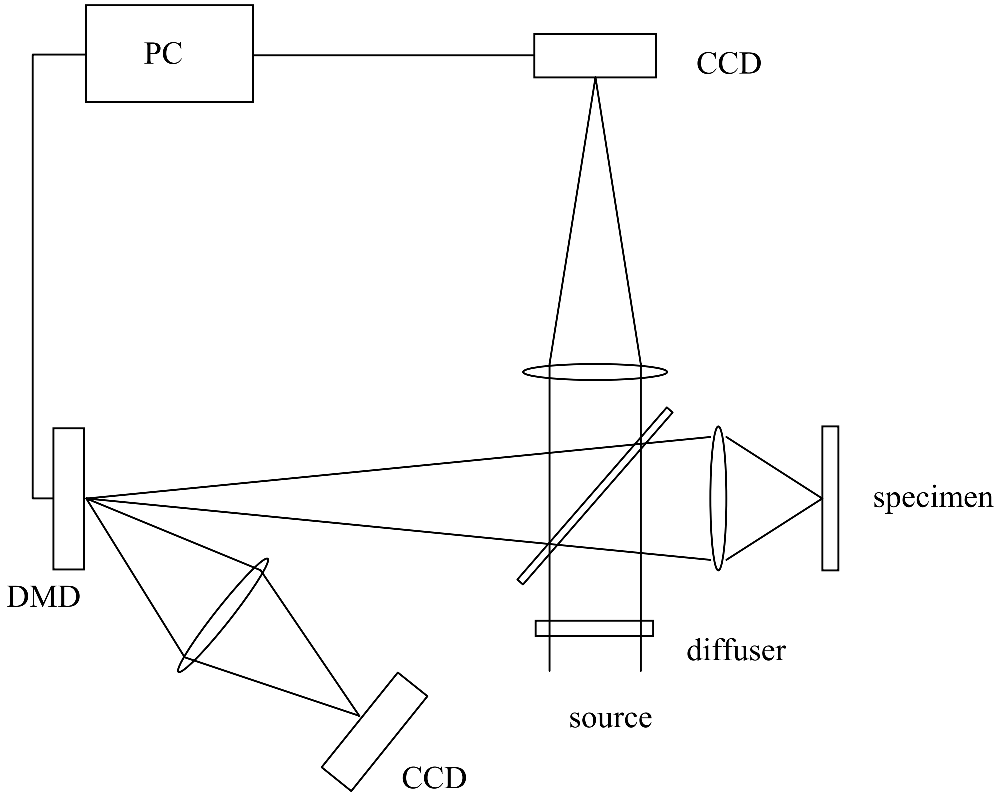

Fig. 8.1. Schematic representation of a speckle-illuminated non-scanning fluorescence microscope using the DMD for optical data processing

Bibliography

1. M. Minsky, *Memoir on Inventing the Confocal Scanning Microscope.* Scanning, 1988. **10**(4): p. 128-138.
2. W.B. Amos, J.G. White, and M. Fordham, *Use of Confocal Imaging in the Study of Biological Structures.* Applied Optics, 1987. **26**(16): p. 3239-3243.
3. S.W. Paddock, ed. *Confocal Microscopy Methods and Protocols*. Methods in Molecular Biology, ed. J.M. Walker. Vol. 122. 1999, Humana Press: Totowa, New Jersey.
4. W.B. Amos and J.G. White, *How the Confocal Laser Scanning Microscope entered Biological Research.* Biology of the Cell, 2003. **95**(6): p. 335-342.
5. D.A. Agard, Y. Hiraoka, P. Shaw, and J.W. Sedat, *Fluorescence Microscopy in 3 Dimensions.* Methods in Cell Biology, 1989. **30**: p. 353-377.
6. S.J. Wright and G. Schatten, *Confocal Fluorescence Microscopy and 3-Dimensional Reconstruction.* Journal of Electron Microscopy Technique, 1991. **18**(1): p. 2-10.
7. M.J. Cole, J. Siegel, S.E.D. Webb, R. Jones, K. Dowling, M.J. Dayel, D. Parsons-Karavassilis, P.M.W. French, M.J. Lever, L.O.D. Sucharov, M.A.A. Neil, R. Juskaitis, and T. Wilson, *Time-domain whole-field fluorescence lifetime imaging with optical sectioning.* Journal of Microscopy-Oxford, 2001. **203**: p. 246-257.
8. D.J. Stephens and V.J. Allan, *Light microscopy techniques for live cell Imaging.* Science, 2003. **300**(5616): p. 82-86.
9. M.R. Young, S.H. Jiang, R.E. Davies, J.G. Walker, E.R. Pike, and M. Bertero, *Experimental confirmation of superresolution in coherent confocal*

scanning microscopy using optical masks. Journal of Microscopy-Oxford, 1992. **165**: p. 131-138.

10. Roy Pike, *Superresolution in fluorescence confocal microscopy and in DVD optical storage*, in *Confocal and Two-photon Microscopy*, A. Diaspro, Editor. 2002, John Wiley and Sons: New York.
11. E.R. Pike and S.H. Jiang, *Ultrahigh-resolution optical imaging of colloidal particles.* Journal of Physics-Condensed Matter, 2002. **14**(33): p. 7749-7756.
12. Roy Pike, Deeph Chana, Pelagia Neocleous, and Shihong Jiang, *Superresolution in scanning optical systems*, in *Optical Imaging and Microscopy*, Peter Torok and F.-J. Kao, Editors. 2003, Springer: Berlin.
13. H. Tadakuma, J. Yamaguchi, Y. Ishihama, and T. Funatsu, *Imaging of single fluorescent molecules using video-rate confocal microscopy.* Biochemical and Biophysical Research Communications, 2001. **287**(2): p. 323-327.
14. X. Michalet, A.N. Kapanidis, T. Laurence, F. Pinaud, S. Doose, M. Pflughoefft, and S. Weiss, *The power and prospects of fluorescence microscopies and spectroscopies.* Annual Review of Biophysics and Biomolecular Structure, 2003. **32**: p. 161-182.
15. J. Zimmermann, A. van Dorp, and A. Renn, *Fluorescence microscopy of single molecules.* Journal of Chemical Education, 2004. **81**(4): p. 553-557.
16. P.J. Shaw, *Introduction to confocal Microscopy*, in *Light Microscopy in Biology*, A.J. Lacey, Editor. 1999, Oxford University Press: New York. p. 45-71.
17. C.J.R. Sheppard, X. Gan, M. Gu, and M. Roy, *Signal-to-noise in confocal microscopes*, in *Handbook of biological confocal microscopy*, J.B. Pawley, Editor. 1995, Plenum Press: New York. p. 363-371.

18. J.R. Swedlow, K. Hu, P.D. Andrews, D.S. Roos, and J.M. Murray, *Measuring tubulin content in Toxoplasma gondii: A comparison of laser-scanning confocal and wide-field fluorescence microscopy.* Proceedings of the National Academy of Sciences of the United States of America, 2002. **99**(4): p. 2014-2019.

19. LSM 510 and LSM 510 META Laser Scanning Microscopes, Operating Manual, Release 3.2, Carl Zeiss, 2002

20. M. Petran, M. Hadravsk, M.D. Egger, and R. Galambos, *Tandem-scanning reflected-light microscope.* Journal of the Optical Society of America, 1968. **58**(5): p. 661.

21. H. Ishida, C. Genka, Y. Hirota, H. Nakazawa, and W.H. Barry, *Formation of planar and spiral Ca2+ waves in isolated cardiac myocytes.* Biophysical Journal, 1999. **77**(4): p. 2114-2122.

22. A. Ichihara, T. Tanaami, H. Ishida, and M. Shimizu, *Confocal fluorescent microscopy using a Nipkow scanner*, in *Fluorescent and Luminescent Probes*, W.T. Mason, Editor. 1999, Academic Press: London.

23. Visitech International. Available at: <http://www.visitech.co.uk> [5 Jan 2005]

24. M.G.L. Gustafsson, D.A. Agard, and J.W. Sedat, *(IM)-M-5: 3D widefield light microscopy with better than 100 nm axial resolution.* Journal of Microscopy-Oxford, 1999. **195**: p. 10-16.

25. M.G.L. Gustafsson, *Surpassing the lateral resolution limit by a factor of two using structured illumination microscopy.* Journal of Microscopy-Oxford, 2000. **198**: p. 82-87.

26. J.T. Frohn, H.F. Knapp, and A. Stemmer, *True optical resolution beyond the Rayleigh limit achieved by standing wave illumination.* Proceedings of the National Academy of Sciences of the United States of America, 2000. **97**(13): p. 7232-7236.

27. J.T. Frohn, H.F. Knapp, and A. Stemmer, *Three-dimensional resolution enhancement in fluorescence microscopy by harmonic excitation.* Optics Letters, 2001. **26**(11): p. 828-830.

28. R. Fedosseev, Y. Belyaev, J. Frohn, and A. Stemmer, *Structured light illumination for extended resolution in fluorescence microscopy.* Optics and Lasers in Engineering, 2005. **43**(3-5): p. 403-414.

29. B. Bailey, D.L. Farkas, D.L. Taylor, and F. Lanni, *Enhancement of Axial Resolution in Fluorescence Microscopy by Standing-Wave Excitation.* Nature, 1993. **366**(6450): p. 44-48.

30. F. Lanni and B. Bailey, *Standing -wave excitation for fluorescence microscopy.* Trends in Cell Biology, 1994. **4**: p. 262-265.

31. B. Bailey, V. Krishnamurthi, D.L. Farkas, D.L. Taylor, and F. Lanni, *Three-dimensional imaging of biological specimens with standing wave fluorescence microscopy.* Proceedings of SPIE, 1994. **2184**: p. 208-213.

32. V. Krishnamurthi, B. Bailey, and F. Lanni, *Image processing in 3-D standing-wave fluorescence microscopy.* Proceedings of SPIE, 1994. **2655**: p. 18-25.

33. M.A.A. Neil, R. Juskaitis, and T. Wilson, *Method of obtaining optical sectioning by using structured light in a conventional microscope.* Optics Letters, 1997. **22**(24): p. 1905-1907.

34. M.A.A. Neil, R. Juskaitis, and T. Wilson, *Real time 3D fluorescence microscopy by two beam interference illumination.* Optics Communications, 1998. **153**(1-3): p. 1-4.

35. M.A.A. Neil, A. Squire, R. Juskaitis, P.I.H. Bastiaens, and T. Wilson, *Wide-field optically sectioning fluorescence microscopy with laser illumination.* Journal of Microscopy-Oxford, 2000. **197**: p. 1-4.

36. S.E.D. Webb, Y. Gu, S. Leveque-Fort, J. Siegel, M.J. Cole, K. Dowling, R. Jones, P.M.W. French, M.A.A. Neil, R. Juskaitis, L.O.D. Sucharov, T. Wilson, and M.J. Lever, *A wide-field time-domain fluorescence lifetime imaging microscope with optical sectioning.* Review of Scientific Instruments, 2002. **73**(4): p. 1898-1907.

37. M.G. Somekh, C.W. See, and J. Goh, *Wide field amplitude and phase confocal microscope with speckle illumination.* Optics Communications, 2000. **174**(1-4): p. 75-80.

38. J.G. Walker, *Non-scanning confocal fluorescence microscopy using speckle illumination.* Optics Communications, 2001. **189**(4-6): p. 221-226.

39. S.H. Jiang and J.G. Walker, *Experimental confirmation of non-scanning fluorescence confocal microscopy using speckle illumination.* Optics Communications, 2004. **238**(1-3): p. 1-12.

40. S. Jiang and J.G. Walker, *Non-scanning fluorescence confocal microscopy using speckle illumination and optical data processing.* Optics Communications, 2005. **256**(1-3): p. 35-45.

41. E. Wang, C.M. Babbey, and K.W. Dunn, *Performance comparison between the high-speed Yokogawa spinning disc confocal system and single-point*

scanning confocal systems. Journal of Microscopy-Oxford, 2005. **218**: p. 148-159.

42. M.G. Gustafsson, *Extended resolution fluorescence microscopy.* Current Opinion in Structrural Biology, 1999. **9**(5): p. 627-634.
43. L.H. Schaefer, D. Schuster, and J. Schaffer, *Structured illumination microscopy: artefact analysis and reduction utilizing a parameter optimization approach.* Journal of Microscopy-Oxford, 2004. **216**: p. 165-174.
44. C.J.R. Sheppard and D.M.Shotton, *Confocal Laser Scanning Microscopy*. Microscopy Handbooks. Vol. 38. 1997, Oxford, UK: BIOS Scientific Publishers.
45. T.Wilson and C.Sheppard, *Theory and Practice of Scanning Optical Microscopy*. 1984, London: Academic Press.
46. T.Wilson, *Confocal Microscopy*. 1990, San Diego, Calif.: Academic.
47. C.J.R. Sheppard and C.J. Cogswell, *3-Dimensional Image-Formation in Confocal Microscopy.* Journal of Microscopy-Oxford, 1990. **159**: p. 179-194.
48. B. Richards and E. Wolf, *Electromagnetic Diffraction in Optical Systems .2. Structure of the Image Field in an Aplanatic System.* Proceedings of the Royal Society of London Series a- Mathematical and Physical Sciences, 1959. **253**(1274): p. 358-379.
49. M. Bertero, P. Boccacci, G.J. Brakenhoff, F. Malfanti, and H.T.M. Vandervoort, *3-Dimensional Image-Restoration and Superresolution in Fluorescence Confocal Microscopy.* Journal of Microscopy-Oxford, 1990. **157**: p. 3-20.

50. B. Ulli, *Optical data processing in high-numerical-aperture imaging, PhD thesis*, in *Department of Physics*. 2000, King's College: London.

51. I. Akduman, U. Brand, J. Grochmalicki, G. Hester, R. Pike, and M. Bertero, *Superresolving masks for incoherent high-numerical-aperture scanning microscopy in three dimensions.* Journal of the Optical Society of America a-Optics Image Science and Vision, 1998. **15**(9): p. 2275-2287.

52. J. Grochmalicki and R. Pike, *Superresolution for digital versatile discs (DVD's).* Applied Optics, 2000. **39**(34): p. 6341-6349.

53. J.W.Goodman, *Statistical Optics*. 1985: John Wiley & Sons.

54. R.N. Bracewell, *The Fourier Transform and its Applications*. 2 ed. 1986, New York: McGraw-Hill Book Company.

55. M. Gu, *Advanced Optical Imaging Theory*. 1999, Berlin: Springer.

56. O. Nakamura and S. Kawata, *3-Dimensional Transfer-Function Analysis of the Tomographic Capability of a Confocal Fluorescence Microscope.* Journal of the Optical Society of America a-Optics Image Science and Vision, 1990. **7**(3): p. 522-526.

57. J.M. Murray, *Evaluating the performance of fluorescence microscopes.* Journal of Microscopy-Oxford, 1998. **191**: p. 128-134.

58. J.Dunlop and D.G.Smith, *Telecommunications Engineering*. 1994: Chapman & Hall.

59. A.D. Ducharme, G.D. Boreman, and D.R. Snyder, *Effects of Intensity Thresholding on the Power Spectrum of Laser Speckle.* Applied Optics, 1994. **33**(13): p. 2715-2720.

60. G. Moddel, K.M. Johnson, W. Li, R.A. Rice, L.A. Paganostauffer, and M.A. Handschy, *High-Speed Binary Optically Addressed Spatial Light-Modulator.* Applied Physics Letters, 1989. **55**(6): p. 537-539.

61. D. Cunningham, J. Sharpe, and K.M. Johnson, *Application of an Optically Addressed Spatial Light-Modulator to Real-Time Speckle Photography.* Optics Communications, 1993. **101**(5-6): p. 311-316.

62. Operator's Manual, Sapphire 488-20 & 460-10 Laser Optically Pumped Semiconductor Laser, Coherent, 2002, http://www.coherent.com

63. ORCA-1394 Digital CCD Camera (C4742-95-12NRG) User's Manual, Hamamatsu Photonics, April 2001

64. J.H. Churnside, *Speckle from a Rotating Diffuse Object.* Journal of the Optical Society of America, 1982. **72**(11): p. 1464-1469.

65. J. B.Pawley, *Handbook of biological confocal microscopy*. 1989: Plenum Press.

66. J.S. Ahearn and et al. *Multiple quantum well (MQW) spatial light modulators (SLMs) for optical data processing and beam steering*. in *Spatial Light Modulators: Technology and Applications*. 2001. San Diego: SPIE The International Society for Optical Engineering.

67. Lenslet Ltd. Available at:<http://www.lenslet.com> [15 May 2005]

68. SVGA2 Miniature LCD User Guide, CRL Opto Limited, 2002, http://www.crlopto.com

69. J. Frank and B.F. McEwen, *Alignment by cross-correlation*, in *Electron Tomography: Three-dimensional Imaging with the Transmission electron Microscope*, F. J., Editor. 1992, Plenum: New York. p. 205-213.

70. Matthew Brett, An introduction to smoothing [online]. Cambridge: MRC Cognition and Brain Sciences Unit, 1999. Available at: <http://www.mrc-cbu.cam.ac.uk/Imaging/Common/smoothing.shtml> [24 February 2005]

71. Q.S. Hanley, P.J. Verveer, M.J. Gemkow, D. Arndt-Jovin, and T.M. Jovin, *An optical sectioning programmable array microscope implemented with a digital micromirror device.* Journal of Microscopy-Oxford, 1999. **196**: p. 317-331.

72. T. Fukano and A. Miyawaki, *Whole-field fluorescence microscope with digital micromirror device: imaging of biological samples.* Applied Optics, 2003. **42**(19): p. 4119-4124.

73. W.S. Rabinovich, M. Bashkansky, S.R. Bowman, R. Mahon, and P.R. Battle, *Speckle photography using optically addressed multiple quantum well spatial light modulators.* Optics Express, 1998. **2**(11): p. 449-453.

74. Wolfgang Becker and Axel Bergmann, Lifetime imaging techniques for optical microscopy [online]. Berlin: Becker & Hickl GmbH, 2003. Available at:<http://www.becker-hickl.de/literature.htm> [1 August 2005]